

國立交通大學

光電工程研究所

博士論文

多極磁性元件之設計與製作

在高精密定位系統之應用

**Design and Fabrication of Multi-Pole Magnetic Components
for High Precision Position System Application**



研究生：邱國基

指導教授：謝漢萍 博士 & 黃得瑞 博士

中華民國九十五年三月

多極磁性元件之設計與製作 在高精密定位系統之應用

**Design and Fabrication of Multi-Pole Magnetic Components
for High Precision Position System Application**

研究生：邱國基

Student : Kuo-Chi Chiu

指導教授：謝漢萍博士

Advisors : Dr. Han-Ping D. Shieh

：黃得瑞博士

：Dr. Der-Ray Huang



國立交通大學電機資訊學院

光電工程研究所

博士論文

A Dissertation
Submitted in Partial Fulfillment of the Requirements
for the Degree of Doctor of Philosophy in
The Institute of Electro-Optical Engineering
College of Electrical Engineering and Computer Science
National Chiao Tung University
Hsinchu, Taiwan

中華民國九十五年三月

摘 要

時序進入微米及次微米的時代，並已投入對奈米尺寸的技術開發，各種量測儀器的精密度不斷地被要求提升以符合所需。由於編碼器是精密量測系統中不可或缺的關鍵元件，因此開發一個小尺寸具有高解析度的編碼器，來增進量測系統的功能為一重要的基本研究。一般而言，編碼器可分為兩類，一為光學式，利用光反射或是透射的特性，造成光線明暗的效果，來作為偵測的訊號；另一為磁性式，藉由磁性南極與北極的差異，來作為檢測的訊號。

磁性編碼器是由一個磁性感測器，以及一個多極磁性元件具有微小磁極距所組成，解析度的高低由磁極距的大小所決定。使用傳統的方法，要製作出磁極距小於 1mm 是非常困難的，精密的機械加工技術以及昂貴且複雜的充磁系統是必備的條件。為了克服製作微小磁極距小於 1mm，來提升磁性編碼器的解析能力，本論文所提出的創新方法，是利用印刷電路板的製程技術，來製作出一特殊的線路圖形於基板上，具有均勻的磁極結構，依據安培定律，在供給線路電流之後，便會感應產生出交錯且規則的磁場分佈，從而獲得一多極磁性元件具有微小磁極距。

為了量測此微小磁極距的磁場分佈，我們設計製作出一個精密的磁場量測系統，使用高解析度的霍爾探棒，其感測面積只有 $165 \times 165 \mu\text{m}^2$ ，因此可以量測出微小磁極距小於 1mm。不同多極磁性元件具有微小磁極距 $300 \mu\text{m}$ 、 $350 \mu\text{m}$ 和 $400 \mu\text{m}$ ，已成功製作出來，同時也量測出其表面上方 $200 \mu\text{m}$ 與 $300 \mu\text{m}$ 處的磁場分佈變化，清楚的磁性邊界顯示出此微小磁極距的大小，分別為 $300 \mu\text{m}$ 、 $350 \mu\text{m}$ 和 $400 \mu\text{m}$ 。因此，磁性編碼器的解析能力可以大幅地提升 3.33 倍 ($1\text{mm}/300 \mu\text{m}$)。此外，利用有限函數疊加計算微小磁極距內之磁場公式也已經推導出來，理論計算的數值與實驗量測的結果有很好的的一致性。

另外，藉由使用雙層的線路結構，可以將其微弱的磁場強度有效地提升 1.37 倍。再者，在磁場最佳化的研究中，使用不同的線路寬度 $190 \mu\text{m}$ 與 $235 \mu\text{m}$ ，其所對應出來的最佳磁極距大小為 $465 \mu\text{m}$ 與 $495 \mu\text{m}$ ，相較於其他尺寸的磁極距，具有較大的磁場強度與變化，上述這些特性是非常有助於後續訊號的檢測與處理。印刷電路板的製程技術已經驗證可以有效地縮減磁極距小於 1mm，不需要精密的機械加工技術，以及昂貴複雜的充磁系統，而且大量生產很容易，不同磁極數目與磁極距尺寸也可以輕易的完成於基板上。

Design and Fabrication of Multi-Pole Magnetic Components for High Precision Position System Application

**Student : Kuo-Chi Chiu Advisors : Dr. Han-Ping D. Shieh
: Dr. Der-Ray Huang**

**Institute of Electro-Optical Engineering
National Chiao Tung University**

Abstract

Micro-, submicro- and nano-related industries have been growing rapidly in recent years. The technologies of precise measurements thus become increasingly more demanding. Since encoders are the key component in precise control systems, developing a high-resolution and small-sized encoder is essential to enable the systems more competitive in performance and price.

Encoders can be classified into optical and magnetic types. The optical type uses the light reflection or transmission as the detection signals. The magnetic type utilizes magnetic south and north poles as the sensing sources. A magnetic encoder comprises a magnetic sensor and a multi-pole magnetic component with a fine magnetic pole pitch. A smaller magnetic pole pitch yields a higher resolution in applications. Using traditional methods, a multi-pole magnetic component magnetized with a fine magnetic pole pitch of less than 1mm is very difficult to achieve. Moreover, it requires a precise mechanical processing and a complicated magnetization system.

In order to overcome the limitation of 1mm in fabricating the magnetic pole pitch, an innovative method by using the printed circuit board (PCB) technology was employed. A special wire circuit pattern was designed and fabricated on the PCB with a periodic structure. According to *Ampere's Law*, an alternate and regular magnetic field distribution is induced after applying a current to the wire circuit.

Thus, a multi-pole magnetic component with a fine magnetic pole pitch is obtained.

Additionally, a precise magnetic field measuring system was designed and set up to measure the field distribution in the fine magnetic pole pitch. A high-sensitivity Hall-effect probe with a fine sensing area of $165 \times 165 \mu\text{m}^2$ was used and therefore it is capable of determining the field distribution with a fine magnetic pole pitch of less than 1mm. Various multi-pole magnetic components with different magnetic pole pitches of $300 \mu\text{m}$, $350 \mu\text{m}$ and $400 \mu\text{m}$ were accomplished. The field distributions were measured at the detection spacing of $200 \mu\text{m}$ and $300 \mu\text{m}$ above the surface of the wire circuit. The explicit boundaries between magnetic poles are found, indicating the fine magnetic pole pitches are $300 \mu\text{m}$, $350 \mu\text{m}$ and $400 \mu\text{m}$, respectively. Correspondingly, the resolution of magnetic encoders can be markedly improved by a factor of 3.33 ($1\text{mm}/300 \mu\text{m}$). Moreover, the field formulae for computing the field distribution in the fine magnetic pole pitch have been also derived. These field solutions are expressed in terms of finite sums of elementary functions and easily implemented in any programming environments. As a comparison, the calculated values of magnetic flux density in the z direction agree with the measurement data.

A dual-layered wire circuit structure was used to improve the field strength. After measurements, a gain factor of 1.37 was obtained in the field enhancement. Furthermore, various wire widths of $190 \mu\text{m}$ and $235 \mu\text{m}$ were used to investigate the field optimization and the corresponding optimal magnetic pole pitches are $465 \mu\text{m}$ and $495 \mu\text{m}$. Such an optimal design has larger strength and steeper variation in the field distribution. Both of them are useful to the signal detection and processing. PCB manufacturing technology has been demonstrated to effectively fabricate a multi-pole magnetic component with a fine magnetic pole pitch to be less than 1mm. This innovative method provides a simple process without using the complicated technologies such as machining technique, magnetizing head and magnetization machine. Additionally, it is also a cost-effective method to enable mass production easily. Different pole numbers and pitch sizes can be also easily fabricated on the PCB through this flexible approach.

Acknowledgements

I am deeply indebted to my thesis advisors, Professor Han-Ping D. Shieh and Professor Der-Ray Huang, for conducting me to pursue my advanced degree in the area of applied magnetism at National Chiao Tung University. This thesis provides a very unique opportunity for scientific research as well as engineering development in the technology of high-precision control system. Working for Professor Shieh and Professor Huang has been rewarding in many aspects.

I am very grateful to the thesis committee members for their constructive and invaluable suggestions on this research. The financial and various technical supports from ITRI are also greatly appreciated. I especially acknowledge Mr. Chin-Sen Chen for his continuous efforts to make this research work possible. I also wish to thank my colleagues in ITRI for their constant encouragement, advice and help on some research subjects.

Finally, I would like to express my sincere appreciation to my parents and family for their patience and encouragement during the years of my study. The sharing of joy and frustration with my wife on my thesis work is an essential element in the completion of this thesis.

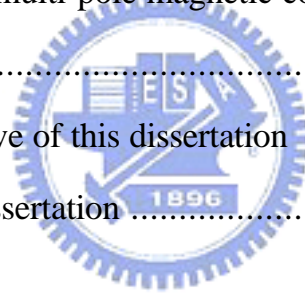
To
my Parents and my Wife



Contents

Chapter 1

Introduction	1
1.1 Overview of encoders	1
1.2 Optical encoder	2
1.3 Magnetic encoder	3
1.4 A review of magnetic encoders related technologies	4
1.4.1 Linear types of multi-pole magnetic components	5
1.4.2 Rotary types of multi-pole magnetic components	8
1.4.3 Summary	13
1.5 Motivation and objective of this dissertation	14
1.6 Organization of this dissertation	15



Chapter 2

Design and fabrication	17
2.1 Introduction	17
2.2 Design	21
2.3 Fabrication	23
2.3.1 Drawing	23
2.3.2 Wire circuit manufacturing process	25
2.4 Summary	28

Chapter 3

Theoretical analysis	29
3.1 Long and straight wire	29
3.2 Straight wire with a finite length L	30
3.2.1 Point P located outside the straight wire	30
3.2.2 Point P located along the bisection line of the straight wire	32
3.2.3 Point P located at the upper position of the straight wire	33
3.2.4 Point P located at the lower position of the straight wire	34
3.3 Two-dimensional analysis	34
3.4 Three-dimensional analysis	36
3.5 Field analysis	37
3.5.1 At Area 1	39
3.5.2 At Area 2	39
3.5.3 At the top side of Area 3	40
3.5.4 At the bottom side of Area 3	41
3.5.5 At the top side of Area 4	42
3.5.6 At the bottom side of Area 4	43
3.5.7 At Area 5	44
3.5.8 At the left side of Area 6	45
3.5.9 At the right side of Area 6	45
3.6 Summary	48

Chapter 4

Field measurements	50
4.1 Dimensional measurements	50
4.2 Magnetic field measuring system	53
4.3 Measurement results	55
4.4 Summary	60

Chapter 5

Field enhancement and optimization	61
5.1 Field enhancement	61
5.1.1 Design and experiments	61
5.1.2 Results and discussions	63
5.1.3 Summary	66
5.2 Field optimization	67
5.2.1 Design and experiments	67
5.2.2 Results and discussions	69
5.2.3 Summary	71

Chapter 6

Field variation analysis	72
6.1 Variation among different multi-pole magnetic components	72
6.2 Variation along different measuring routes	73
6.3 Summary	77

Chapter 7

Conclusions 78

References 82

Appendix 86



List of Figures

Fig. 1-1.	Configurations of (a) a linear, (b) 2D and (c) rotary optical encoders.	2
Fig. 1-2.	(a) An optical encoder used in the inkjet printer. (b) Enlarged photo of the optical grating element.	3
Fig. 1-3.	Configurations of (a) a linear, (b) 2D and (c) rotary magnetic encoders.	4
Fig. 1-4.	(a) A magnetic encoder employed in the lens module. (b) Enlarged photo of the multi-pole magnetic component.	4
Fig. 1-5.	Linear types of a magnetizing head and (b) a multi-pole magnetic component on a magnetic sheet.	6
Fig. 1-6.	Magnetic moments exist inside the magnetic material (a) before magnetization and (b) after magnetization.	6
Fig. 1-7.	A LPM mover used in the magnetic encoder with a tooth structure as a multi-pole magnetic component.	7
Fig. 1-8.	Output voltage varied with the bias gap b_b and tooth pitch p .	8
Fig. 1-9.	Rotary types of multi-pole magnetic components (a) in the axial and (b) in the radial directions for various applications.	8
Fig. 1-10.	(a) Schematic view of the magnetizing fixture in the axial direction. (b) Configuration of the winding pattern in the magnetizing fixture. (c) Photos of the fixture base and magnetizing fixture.	9
Fig. 1-11.	(a) Configuration and (b) photo of a unique magnetizing head.	10
Fig. 1-12.	(a) Schematic view and (b) photo of a multi-pole magnetic drum (magnetic component) with a fine magnetizing pitch λ mounted on the base.	11
Fig. 1-13.	(a) Photo and (b) schematic view of a precise multi-pole magnetization system including a magnetizing head and a magnetization machine.	12
Fig. 2-1.	Magnetic flux density distribution in a long and straight wire.	18
Fig. 2-2.	(a) Linear wire circuit pattern with a periodic structure. (b) The magnetic flux density distribution induced from the linear wire circuit pattern.	19

Fig. 2-3.	(a) Annular wire circuit pattern with a multi-pole configuration in the radial direction. (b) The magnetic flux density distribution induced from the annular wire circuit pattern.	19
Fig. 2-4.	Special wire circuit pattern designed for fabricating a multi-pole magnetic component with a fine magnetic pole pitch.	21
Fig. 2-5.	(a) Schematic view of the cross section on the special wire circuit pattern along the bisection line. (b) The magnetic flux density distribution generated from the special wire circuit pattern.	22
Fig. 2-6.	Schematic view of the cross section on a dual-layered wire circuit structure along the bisection line.	22
Fig. 2-7.	Geometrical structures of (a) single-layered and (b) dual-layered wire circuits.	23
Fig. 2-8.	Various drawings of nine-pole magnetic components with different fine magnetic pole pitches of (a) 250 μm by using a wire width of 100 μm and a gap of 150 μm , (b) 300 μm by using a wire width of 100 μm and a gap of 200 μm , (c) 250 μm by using a wire width of 125 μm and a gap of 125 μm , and (d) 300 μm by using a wire width of 125 μm and a gap of 175 μm .	24
Fig. 2-9	(a) Nine-pole and (b) nineteen-pole wire circuit masks.	25
Fig. 2-10.	Flow charts of wire circuit manufacturing process. (a) The surface of the copper film is cleaned up to be free from dusts. (b) A photoresist layer is applied to the surface of the copper film. (c) A pre-prepared mask is placed on the top of the photoresist layer. (d) The UV light is employed to proceed the light exposure process. (e) The non-exposed area is removed through a developing process. (f) The copper film at the exposed area is removed by chemical reaction using an etching solvent. (g) The residual photoresist on the surface of the wire circuit is stripped. (h) The wire circuit is accomplished on the substrate.	26
Fig. 2-11.	A nine-pole magnetic component fabricated on the PCB with a fine magnetic pole pitch of 350 μm by using a wire width of 175 μm and a gap of 175 μm .	27
Fig. 2-12.	A 29-pole magnetic component fabricated on the PCB with a fine magnetic pole pitch of 500 μm by using a wire width of 225 μm and a gap of 275 μm .	28

Fig. 3-1.	Long and straight wire carrying a steady current I , the element dl contributes a $d\vec{B}$ at the point P .	30
Fig. 3-2.	A straight wire with a finite length L carrying a steady current I , the element dz' contributes a $d\vec{B}$ at the point P located outside the straight wire.	31
Fig. 3-3.	A straight wire with a finite length L carrying a steady current I , the element dz' contributes a $d\vec{B}$ at the point P located along the bisection line of the straight wire.	32
Fig. 3-4.	A straight wire with a finite length L carrying a steady current I , the element dz' contributes a $d\vec{B}$ at the point P located at the upper position of the straight wire.	33
Fig. 3-5.	A straight wire with a finite length L carrying a steady current I , the element dz' contributes a $d\vec{B}$ at the point P located at the lower position of the straight wire.	34
Fig. 3-6.	Mesh of a straight wire with a finite length L carrying a steady current I and the wire width $T1 \approx r$. The distance r_{n1} decreases slightly with a small $t1$.	35
Fig. 3-7.	(a) Mesh and (b) corresponding positions of all elements of a straight wire with a wire width $T1 \approx r$ and a wire thickness $T2 \approx r$ carrying a steady current I . The distances of r_{n1} and z_{n2} decrease slightly with a small $t1$ and $t2$, respectively.	36
Fig. 3-8.	(a) Geometrical structure, current loop and induced field direction of the wire circuit. (b) Corresponding positions of each segment and six areas indicated with different colors for study separately.	38
Fig. 3-9.	Top view of the central pole on the PCB sample and the corresponding cross section of the wire circuit.	47
Fig. 3-10.	Calculated field distributions of the central pole along the bisection line for the magnetic pole pitch of $300\mu\text{m}$ at the detection spacing of $200\mu\text{m}$ and $300\mu\text{m}$.	48
Fig. 3-11.	Calculated field distributions of the central pole along the bisection line for the magnetic pole pitch of $400\mu\text{m}$ at the detection spacing of $200\mu\text{m}$ and $300\mu\text{m}$.	48

Fig. 4-1.	Precise dimension measuring system.	51
Fig. 4-2.	(a) Image of wire circuit captured and displayed on the monitor through CCD module. (b) Enlarged image of copper wires on the PCB sample.	52
Fig. 4-3.	(a) Sample of part copper wires fixed by using the acrylic resin. (b) Enlarged images of the thickness of part copper wires fabricated on the PCB sample.	53
Fig. 4-4.	Precise magnetic field measuring system.	54
Fig. 4-5.	Top view of the three central poles on nine-pole magnetic components and the corresponding cross section.	55
Fig. 4-6.	Field distributions at the detection spacing of $200\mu\text{m}$ and $300\mu\text{m}$ for the magnetic pole pitch of $300\mu\text{m}$ ($T1/G=5/7$).	56
Fig. 4-7.	Field distributions at the detection spacing of $200\mu\text{m}$ and $300\mu\text{m}$ for the magnetic pole pitch of $350\mu\text{m}$ ($T1/G=6/8$).	56
Fig. 4-8.	Field distributions at the detection spacing of $200\mu\text{m}$ and $300\mu\text{m}$ for the magnetic pole pitch of $400\mu\text{m}$ ($T1/G=7/9$).	57
Fig. 4-9.	Field distributions with various ratios of $T1/G$ at the detection spacing of $200\mu\text{m}$.	58
Fig. 4-10.	Field distributions with various ratios of $T1/G$ at the detection spacing of $300\mu\text{m}$.	58
Fig. 4-11.	Field distributions of the central pole along the bisection line with various ratios of $T1/G$ at the detection spacing of $200\mu\text{m}$.	59
Fig. 4-12.	Field distributions of the central pole along the bisection line with various ratios of $T1/G$ at the detection spacing of $300\mu\text{m}$.	60
Fig. 5-1.	Cross section, induced magnetic field and equivalent circuit of DL wire circuit structure.	62
Fig. 5-2.	Field distributions for the magnetic pole pitch of $500\mu\text{m}$ at the detection spacing of $200\mu\text{m}$ and $300\mu\text{m}$ with SL wire circuit structure.	64
Fig. 5-3.	Field distributions for the magnetic pole pitch of $500\mu\text{m}$ at the detection spacing of $200\mu\text{m}$ and $300\mu\text{m}$ with DL wire circuit structure.	64
Fig. 5-4.	Field distributions for the magnetic pole pitch of $500\mu\text{m}$ at SL and DL wire circuit structures.	65

Fig. 5-5.	Calculated values and measurement data of the central pole for the magnetic pole pitch of $500\mu\text{m}$ on SL wire circuit structure.	66
Fig. 5-6.	Calculated values and measurement data of the central pole for the magnetic pole pitch of $500\mu\text{m}$ on DL wire circuit structure.	66
Fig. 5-7.	(a) Geometrical structure of a straight wire with a finite length. (b) The field distribution calculated along the bisection line at at the detection spacing of $200\mu\text{m}$.	68
Fig. 5-8.	Pole structure and optimal condition in the field distribution.	68
Fig. 5-9.	Field distributions of the central pole at different magnetic pole pitches of $365\mu\text{m}$, $465\mu\text{m}$ and $565\mu\text{m}$ by using the wire width $T1$ of $190\mu\text{m}$.	70
Fig. 5-10.	Field distributions of the central pole at different magnetic pole pitches of $395\mu\text{m}$, $495\mu\text{m}$ and $595\mu\text{m}$ by using the wire width $T1$ of $235\mu\text{m}$.	70
Fig. 6-1.	Field distributions along the bisection line among different 9-pole, 19-pole, and 29-pole magnetic components with a fine magnetic pole pitch of $500\mu\text{m}$.	73
Fig. 6-2.	Different measuring routes with various wire segments b .	73
Fig. 6-3.	Field distributions along different measuring routes in the 9-pole magnetic component with a fine magnetic pole pitch of $400\mu\text{m}$.	74
Fig. 6-4.	Field distributions along different measuring routes in the 19-pole magnetic component with a fine magnetic pole pitch of $400\mu\text{m}$.	75
Fig. 6-5.	Field distributions of the central pole along different measuring routes in the z direction for the 9-pole magnetic component.	76
Fig. 6-6.	Field distributions of the central pole along different measuring routes in the z direction for the 19-pole magnetic component.	76

List of Tables

Table 2-1	Comparison among different methods	20
Table 4-1	Various wire widths $T1$, gaps G , pitch sizes, and ratios of $T1/G$	55
Table 5-1	Parameters on DL wire circuit structure	63
Table 5-2	Parameters of wire width $T1$, distance r_{max} , gap G and optimal magnetic pole pitch $T1+G$	69
Table 6-1	ious values of magnetic flux density at various wire segments b for 9-pole and 19-pole magnetic components	75

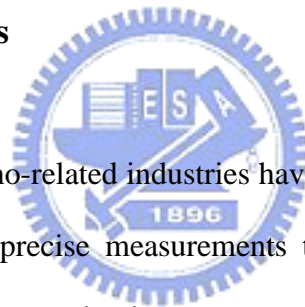


Chapter 1

Introduction

The principles and configurations of different optical and magnetic encoders are presented. A review of magnetic encoders related technologies are also reported and some critical issues with respect to the improvement of performance are considered as well. Finally, the motivation, objective and organization of this dissertation are discussed.

1.1 Overview of encoders



Micro-, submicro- and nano-related industries have been growing rapidly in recent years. The technologies of precise measurements thus become increasingly more demanding. Since encoders are the key component in precise control systems, developing a high-resolution and small-sized encoder is essential to enable the systems more competitive in performance and price. Encoders can be classified into optical and magnetic types. Both of them are widely used to detect the position, angle or speed in precise control systems. They are playing an important role in Information Application (IA) products, in automatic manufacturing for various industries, etc. Consequently, encoders can be frequently found in different places such as lathes for the precise machining, printers for the precise printing and optical disc drives for the precise reading, etc.

The performance of magnetic encoders is now comparable to that of optical types. They are rigid with a simple structure to offer a reliable operation in adverse

environments with large vibration, high temperature, dense moisture or dust. Since encoders are only an auxiliary element in a system, they do not much attract the mainstream academic and industrial attentions. Only a few scholars and researchers had been interested in and devoted to the research of this important key component [1-19]. Both of optical and magnetic encoders will be introduced in the following sections.

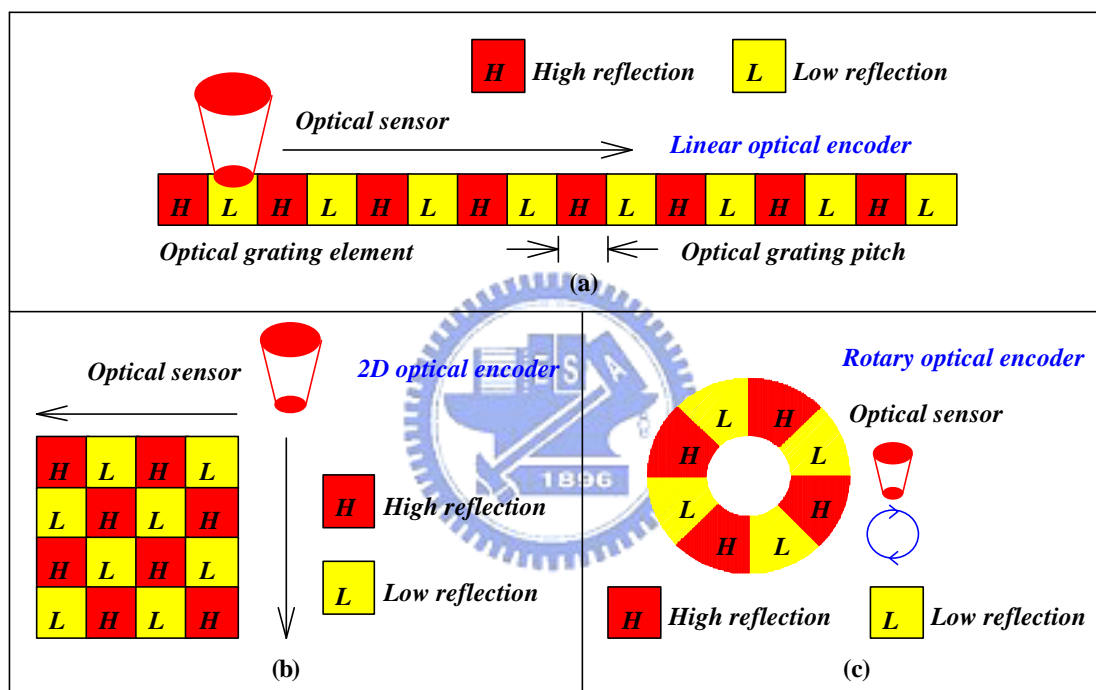


Fig. 1-1. Configurations of (a) a linear, (b) 2D and (c) rotary optical encoders.

1.2 Optical encoder

An optical encoder comprises an optical sensor and an optical grating element with a fine grating pitch. A smaller pitch size yields a higher resolution in applications. Figure 1-1 shows the configurations of various linear, 2D and rotary optical encoders, respectively. The high (H) and low (L) reflection signals can be detected by using the optical sensor when the light reflects from or transmits through

the optical grating element. Consequently, the precise position, angle or speed can be obtained by counting the number of high and low reflection signals.

An example of an optical encoder used in the inkjet printer for controlling the precise position in printing is illustrated in Fig. 1-2. The similar high and low reflection signals are detected when the light passes through the optical grating element. After counting the number of high and low reflection signals, the precise position can be found. Accordingly, the documents can be printed out accurately.

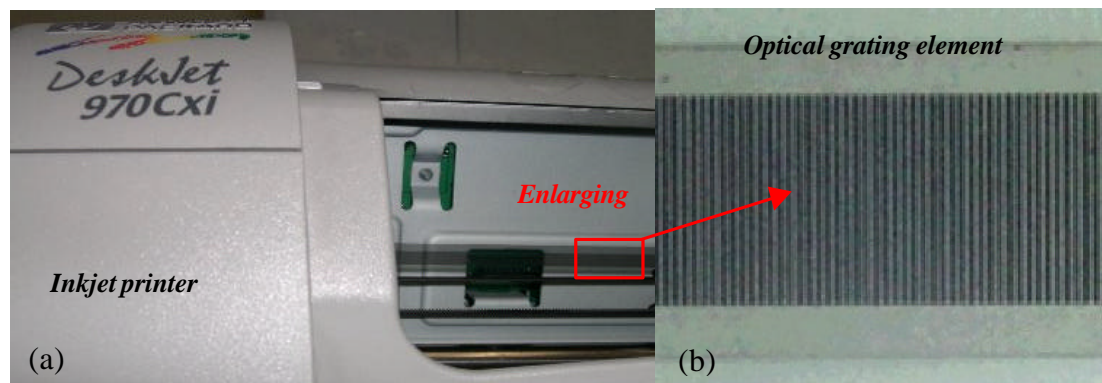


Fig. 1-2. (a) An optical encoder used in the inkjet printer. (b) Enlarged photo of the optical grating element.

1.3 Magnetic encoder

A magnetic encoder consists of a magnetic sensor and a multi-pole magnetic component with a fine magnetic pole pitch. Figure 1-3 indicates the configurations of various linear, 2D and rotary magnetic encoders, respectively. The resolution of magnetic encoders can be markedly improved by narrowing the magnetic pole pitch. Different field distributions of magnetic south (S) and north (N) poles are distinguished from the magnetic sensor. Correspondingly, the precise position, angle or speed can be acquired after counting the number of magnetic poles.

An example of a magnetic encoder employed in the lens module for controlling

the precise focusing when taking photographs is shown in Fig. 1-4. The precise position in focusing can be decided after accumulating the number of magnetic poles.

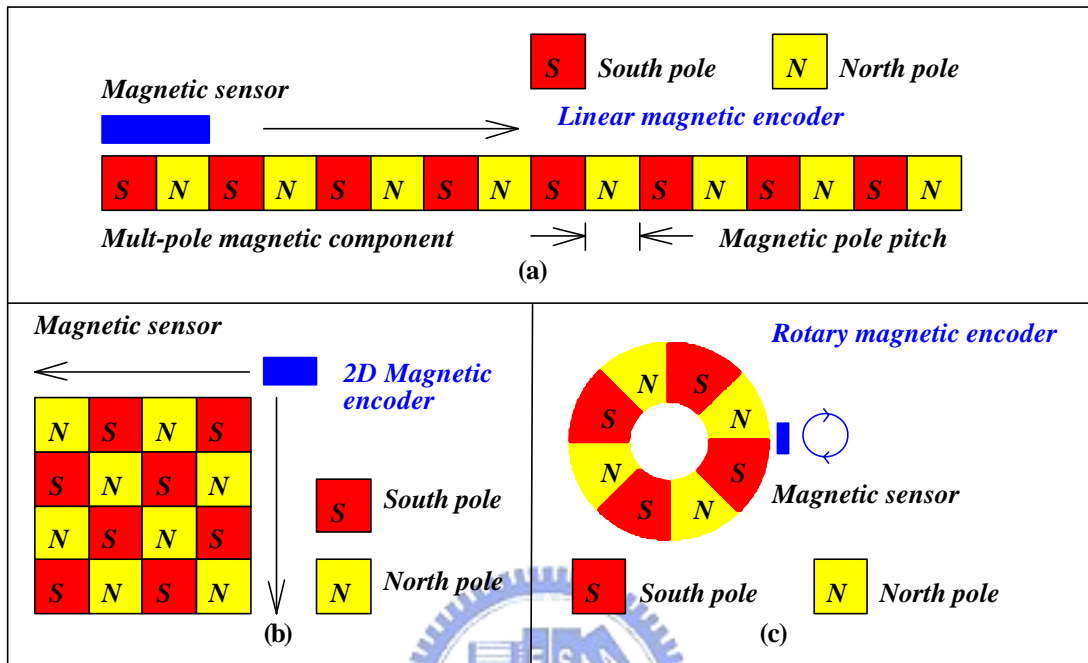


Fig. 1-3. Configurations of (a) a linear, (b) 2D and (c) rotary magnetic encoders.

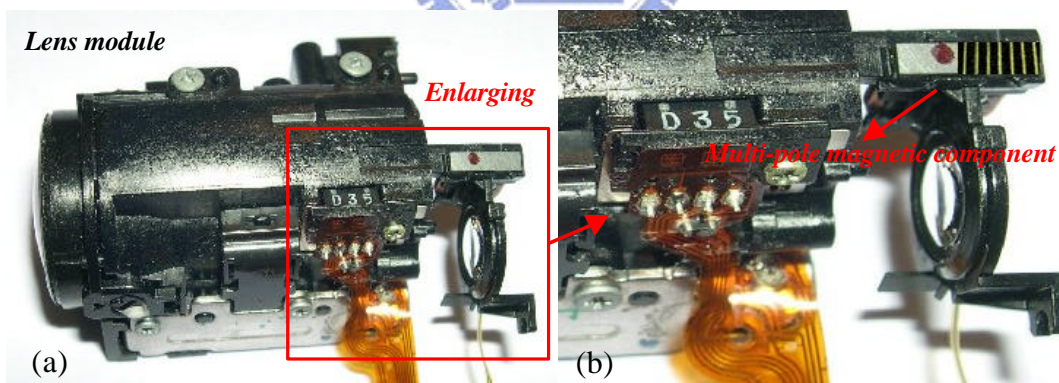


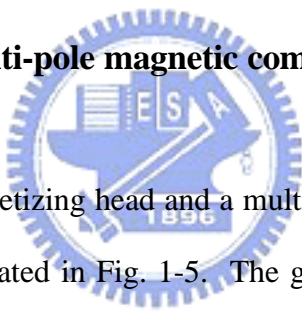
Fig. 1-4. (a) A magnetic encoder employed in the lens module. (b) Enlarged photo of the multi-pole magnetic component.

1.4 A review of magnetic encoders related technologies

Several methods have been used to fabricate a multi-pole magnetic component with a fine magnetic pole pitch for use in magnetic encoders. However, a costly and

complicated magnetization system including a precise magnetizing head (or fixture) and a magnetization machine is required [1-14]. During the magnetization process, an unmagnetized magnetic component is placed on the top of a magnetizing head. The magnetizing coils are wound and fixed on the magnetizing head with a multi-pole configuration. The terminals of magnetizing coils are connected to a magnetization machine, which can provide a large magnetizing current. A large magnetic field is induced instantaneously to magnetize the magnetic component into a multi-pole structure after applying a large current to the magnetizing coils. Thus, a multi-pole magnetic component can be obtained. Different methods for fabricating various types of multi-pole magnetic components are discussed as follows.

1.4.1 Linear types of multi-pole magnetic components



The linear types of a magnetizing head and a multi-pole magnetic component on a magnetic sheet [20] are illustrated in Fig. 1-5. The grooves in the magnetizing head are designed for winding the magnetizing coils to form an alternate magnetic field distribution. The spacing between any two adjacent grooves is defined as the gap. The sum of groove width and gap is defined as the magnetic pole pitch, which is limited by machining techniques. The minimum magnetic pole pitch can be achieved only around 1mm through this approach. Additionally, the waveform of the magnetizing current should be modified to fit the material characteristic of the magnetic component to attain the optimal condition for magnetization.

Before magnetization, the magnetic moments inside the magnetic material are in a random state. The net magnetic moment is zero and therefore no magnetic field exists in the magnetic component. However, the magnetic moments will move to the same direction after magnetization. Consequently, the net magnetic moment is not

zero and the magnetic field is thus generated in the magnetic component, as shown in Fig. 1-6.

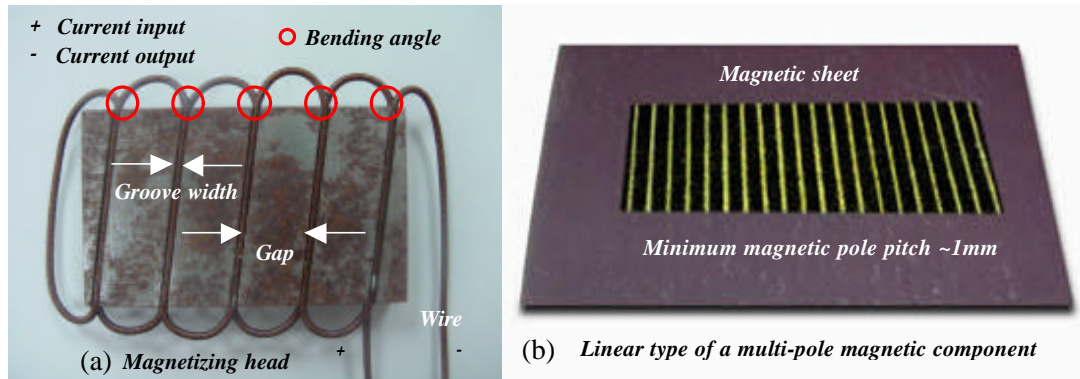


Fig. 1-5. Linear types of a magnetizing head and (b) a multi-pole magnetic component on a magnetic sheet.

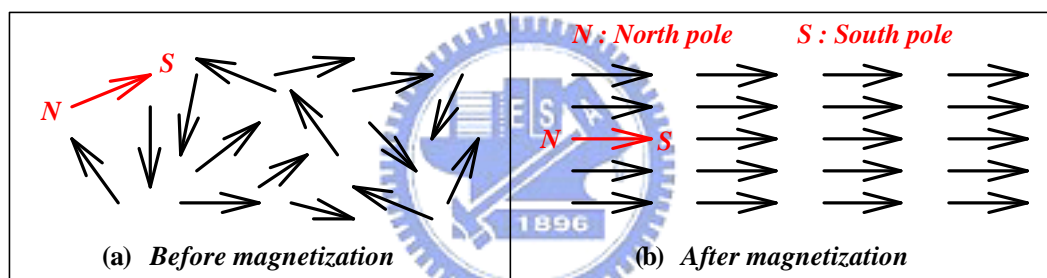


Fig. 1-6. Magnetic moments exist inside the magnetic material (a) before magnetization and (b) after magnetization.

During the magnetization process, the magnetic sheet is placed on the top of the magnetizing head. According to *Ampere's law*, an alternate magnetic field distribution is induced instantaneously after applying a current to the current input on the head. Accordingly, a linear type of multi-pole magnetic component is obtained [21]. The magnetizing head is made of a permalloy, which has a very high permeability that can concentrate the magnetic flux to enhance the magnetic field for magnetization. However, the insulating layer of magnetizing coils is easy to damage at the large bending angle in grooves and this often leads to a short circuit. Moreover, the large magnetization energy needs to disperse in a few seconds and

therefore the magnetizing coils are broken frequently during the magnetization process. This approach is thus very dangerous.

A method proposed by Y. Kikuchi et al. who used a linear pulse motor (LPM) mover in a magnetic encoder [22]. The LPM mover is made of carbon steel with a tooth structure as a multi-pole magnetic component. A bias magnet is hired to generate different magnetic resistance and a MR element is employed to detect the resistance in the tooth structure, as shown in Fig. 1-7. After counting the number of output pulses from MR element, the exact displacement is obtained.

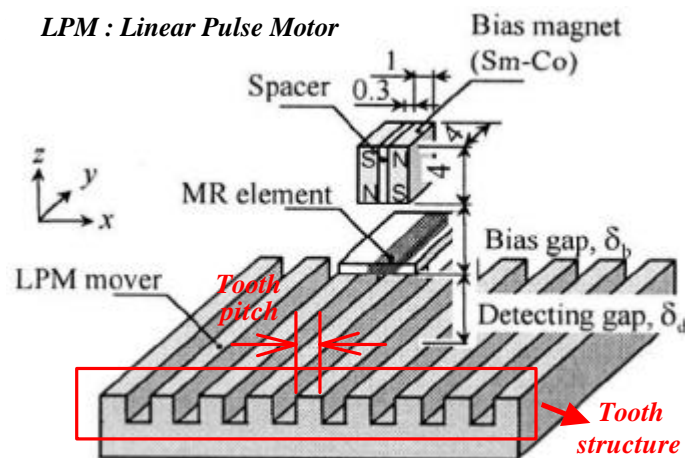


Fig. 1-7. A LPM mover used in the magnetic encoder with a tooth structure as a multi-pole magnetic component.

Although the tooth pitch in the LPM mover (multi-pole magnetic component) can be narrowed to around 0.8mm without using the costly and complicated magnetization system, the uniformity of LPM mover structure is not easy to control and fabricate by using conventional machining tools. Moreover, the bias gap δ_b and detecting gap δ_d should be also carefully adjusted to obtain the maximum variation in the magnetic resistance for measurements. Additionally, a well design and alignment among the bias magnet, MR element and LPM mover are required as well. Furthermore, the output voltage from MR element is varied with the bias gap

δ_b and tooth pitch significantly, as illustrated in Fig. 1-8. All above-mentioned problems are difficult to handle in applications through this approach.

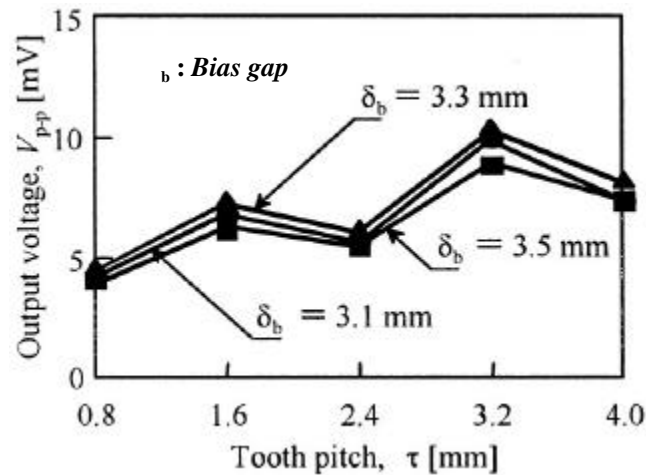


Fig. 1-8. Output voltage varied with the bias gap δ_b and tooth pitch τ .

1.4.2 Rotary types of multi-pole magnetic components

Except linear types, the rotary types of multi-pole magnetic components are also widely used in precise control systems, as shown in Fig. 1-9 [20]. The components are magnetized in the axial and radial directions for various applications. Figure 1-10 demonstrates a rotary type of magnetizing fixture (or head) is employed to magnetize the magnetic component into an eight-pole structure in the axial direction.

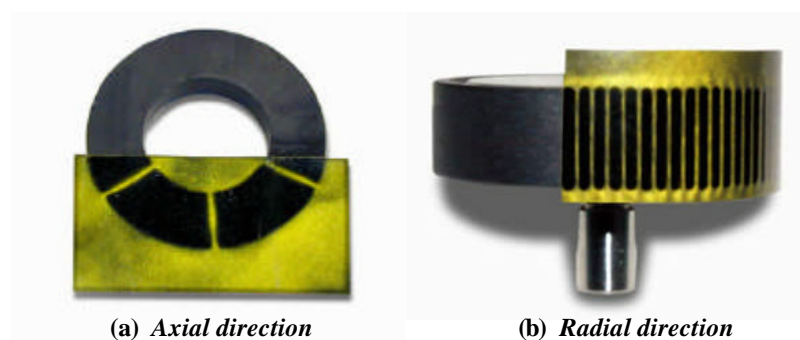


Fig. 1-9. Rotary types of multi-pole magnetic components (a) in the axial and (b) in the radial directions for various applications.

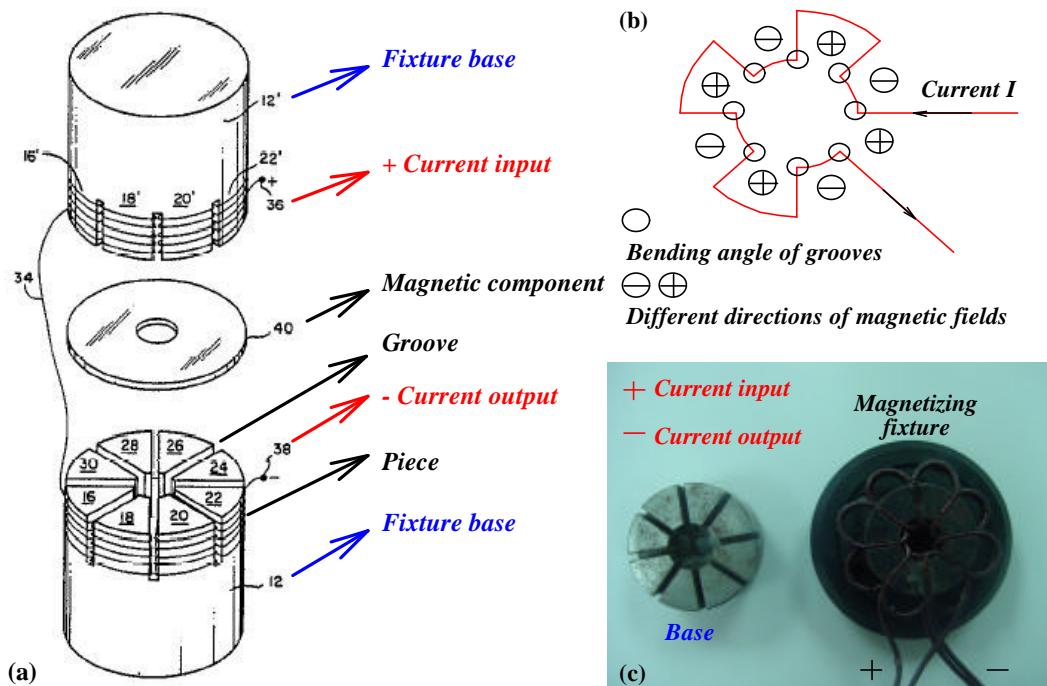


Fig. 1-10. (a) Schematic view of the magnetizing fixture in the axial direction. (b) Configuration of the winding pattern in the magnetizing fixture. (c) Photos of the fixture base and magnetizing fixture.

Both of fixture bases (12 and 12') are also made of a permalloy, which has a very high permeability that can concentrate the magnetic flux to enhance the magnetic field for magnetization [23-24]. The surfaces of fixtures are divided into eight equal pieces (16~30 and 16'~30') through the line-cutting process. The magnetizing coils (15' and 34) are wound into the grooves. An alternate multi-pole magnetic field distribution is formed from using an appropriate layout of magnetizing coils, as illustrated in Fig. 1-10 (b). Both terminals of current input (36) and output (38) are connected to a magnetization machine. A large magnetic field is induced instantaneously after the magnetization machine releases a large magnetizing current. The magnetic component (40) is then magnetized into an eight-pole structure.

Unfortunately, the same problem also occurs in this rotary type of magnetizing fixture, as discussed in the linear type. The insulating layer of magnetizing coils can not withstand the stress and finally results in break. Consequently, a short circuit

happens between the bases of magnetizing fixtures. Since both bases are made of a permalloy, the magnetizing coils and fixtures are often exploded during the magnetization process. The risk of explosion can not be avoided because the large magnetic field is required for reversing the magnetic moments inside the magnetic material. The sum of groove width and piece size is defined as the magnetic pole pitch, which is also limited by machining techniques. Accordingly, it is not easy to have a fine magnetic pole pitch of less than 1mm through this approach.

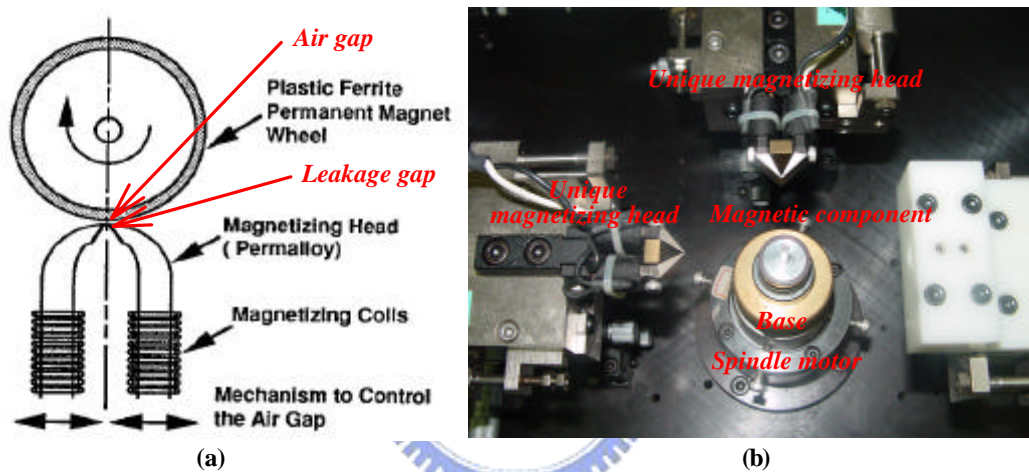


Fig. 1-11. (a) Configuration and (b) photo of a unique magnetizing head.

In order to overcome the limitation of 1mm in fabricating the fine magnetic pole pitch, a single-pulse magnetization method, which resembles the magnetic recording technology, was introduced [25]. Figure 1-11 (a) shows the magnetizing coils are wound and fixed on a unique magnetizing head. A leakage gap exists in the head to leak out the magnetic flux to record magnetic pole pairs (i.e. N and S pole) onto the surface of the plastic ferrite permanent magnet wheel (magnetic component). The magnetic pole pitch of less than 1mm can be achieved by using this method. Before magnetization, the magnetic component is mounted on a base that is usually supported and rotated through a high-precision spindle motor, as shown in Fig. 1-11

(b). The precise position control of the spindle motor is highly required; otherwise, an asymmetric magnetic field distribution will appear on the multi-pole magnetic component after magnetization. The asymmetric magnetic field distribution is not useful to the subsequent processing of signals.

After magnetization, a multi-pole magnetic drum (magnetic component) with a fine magnetizing pitch λ is obtained, as shown in Fig. 1-12. A precise MR element is employed to determine the field distribution generated from the multi-pole magnetic drum.

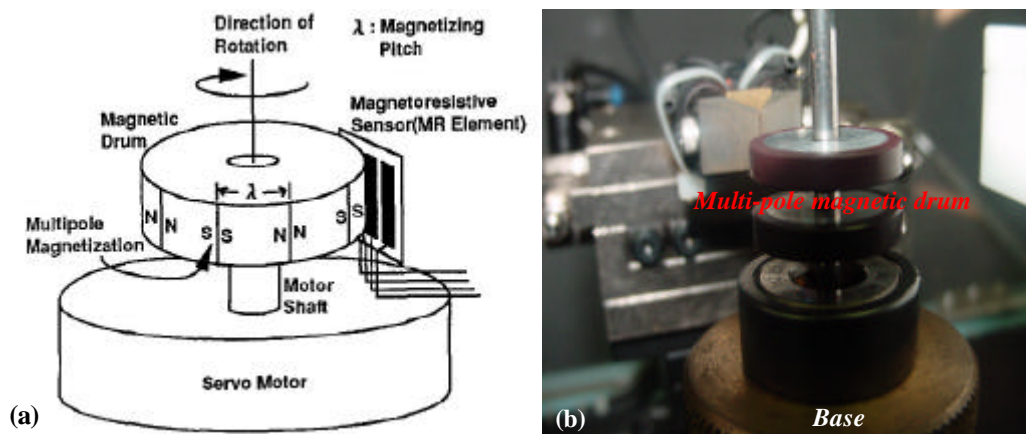


Fig. 1-12. (a) Schematic view and (b) photo of a multi-pole magnetic drum (magnetic component) with a fine magnetizing pitch λ mounted on the base.

A precise multi-pole magnetization system comprises a magnetizing head and a magnetization machine, as shown in Fig. 1-13 (a). The red mark in Fig. 1-13 (b) represents the unit of the magnetizing head, as discussed in Figs. 1-11(a) and 1-12(a). The blue area indicates the unit of the magnetization machine, as illustrated in Fig. 1-13 (b). The field distributions of multi-pole magnetic components are detected by using a Gauss meter with a precise Hall-effect probe. The precise position of the spindle motor is controlled through the μP controller. The magnetic pole pairs are recorded intermittently onto the surface of the magnetic component through the pulse

width modulation (PWM) generation circuit and drive circuit. All tasks are carefully handled by the personal computer.

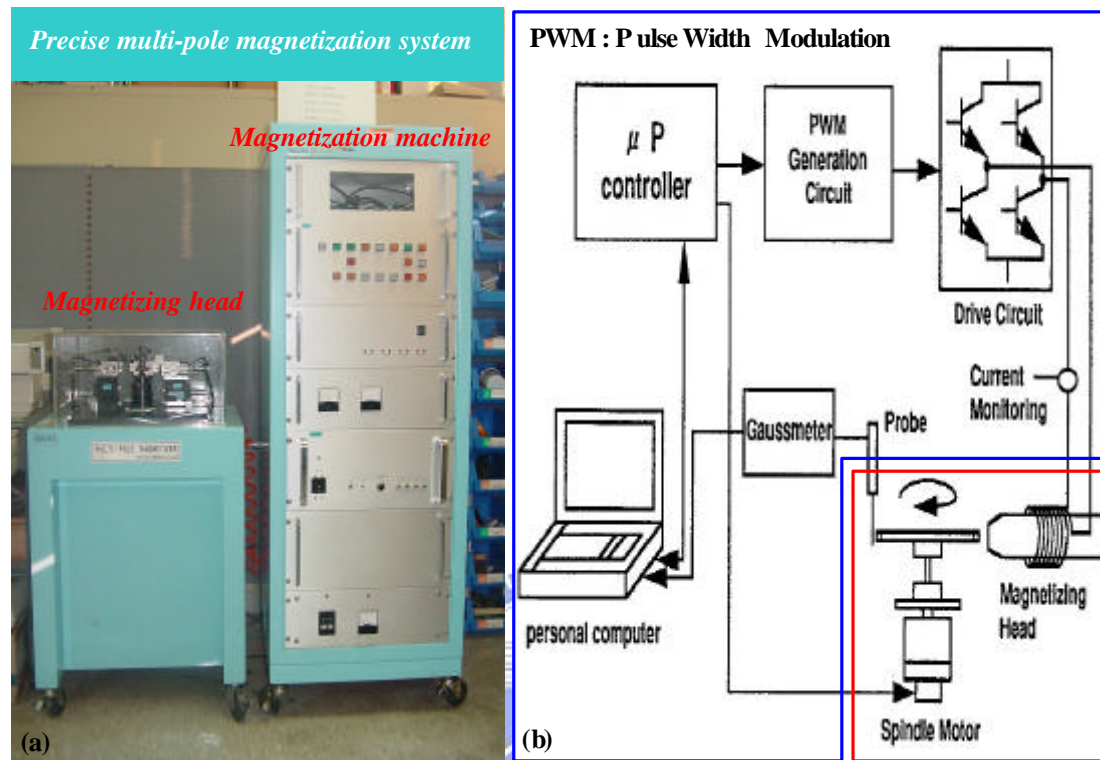


Fig. 1-13. (a) Photo and (b) schematic view of a precise multi-pole magnetization system including a magnetizing head and a magnetization machine.

During the magnetization process, the magnetic component will often collide with the head if its radial run-out is too large and thus results in damages on both of them. Consequently, the dimension of the magnetic component must be fabricated uniformly with a small radial run-out. Moreover, the leakage gap in the head and the air gap between the head and magnetic component must be properly adjusted to obtain the desired magnetic pole pitch. As the magnetic pole pitch gets smaller, both of leakage and air gaps need to be narrowed as well. These are key factors to affect the size of the magnetic pole pitch in magnetization.

Furthermore, the waveform of the magnetizing current from the magnetization system is required to modify to fit the magnetic material property of the magnetic

component. In addition to the tiny radial run-out and material homogeneity, the magnetic component must be mounted on a spindle motor under a precise position control. All requirements for magnetization can be achieved only through the precise multi-pole magnetization system.

Despite the fact that the single-pulse magnetization method can narrow the magnetic pole pitch to be less than 1mm, the fabrication process is very difficult and complicated. Additionally, the precise machining technique, magnetizing head and magnetization machine are also necessary. Consequently, the single-pulse magnetization method is costly in fabricating a multi-pole magnetic component with a fine magnetic pole pitch.

1.4.3 Summary



Several methods have been discussed to fabricate a multi-pole magnetic component with a fine magnetic pole pitch. For practical applications, some critical issues are required for narrowing the magnetic pole pitch as mentioned as the following :

- Precise machining

To fabricate the magnetic component with a small radial run-out for magnetization.

- Magnetizing head (fixture)

To magnetize the magnetic component into a multi-pole structure with a fine magnetic pole pitch.

■ Magnetization machine

To supply and modify the magnetizing current to fit the material characteristic of the magnetic component.

1.5 Motivation and objective of this dissertation

A wide magnetic pole pitch is insufficient for high-resolution control applications. Traditionally, a magnetizing head, which is used to magnetize the magnetic component into a multi-pole structure, is fabricated through the line-cutting process. Since the process is highly depended upon the precision of machining tools, it is difficult to have a fine magnetic pole pitch of less than 1mm. The single-pulse magnetization method, which resembles the magnetic recording technology, is also mentioned to fabricate a multi-pole magnetic component. Finally, the limitation of 1mm in the magnetic pole pitch is overcome by using this costly and complicated method.

In view of foregoing problems in narrowing the magnetic pole pitch, the precise magnetizing head and magnetization machine are required. Additionally, the precise machining techniques are essential to produce the magnetic component with a small radial-runout for magnetization. *In order to overcome the different technical barriers, creating an innovative method with a simple process to fabricate a multi-pole magnetic component with a fine magnetic pole pitch of less than 1mm is the motivation of this dissertation.*

PCB manufacturing technology has been applied to many products and gained a great success at various industrial applications. More and more electric devices can be placed on a substrate and the corresponding wire circuit density is thus higher and higher than before. According to electromagnetism, applying a current to a long and

straight wire will induce an annular magnetic field around the wire. The magnetic flux density is proportional to the current input, but inversely proportional to the distance [26]. Consequently, an alternate and regular magnetic field distribution can be obtained from designing a special wire circuit pattern with an appropriate layout. Thus, a multi-pole magnetic component can be accomplished by forming the special wire circuit pattern on the PCB. *The objective of this dissertation is to fabricate a multi-pole magnetic component with a fine magnetic pole pitch by using the PCB manufacturing technology.*

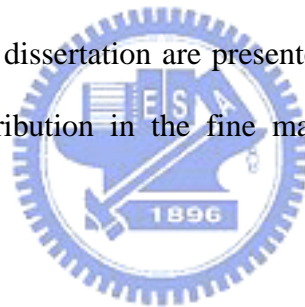
At present, the minimum wire width and the gap between any two adjacent wires on the circuit can be achieved are about 3mils ($\sim 75\mu\text{m}$, $1\text{mil} = 25.4\mu\text{m}$) through the PCB manufacturing technology. Correspondingly, it is highly possible to have a fine magnetic pole pitch of less than 1mm. *The first goal of this thesis is to design and fabricate a special wire circuit pattern having a multi-pole structure with a fine magnetic pole pitch of less than 1mm on the PCB.*

Since the induced magnetic fields among the wire circuits are very small, the field distributions in the fine magnetic pole pitch are not easy to detect. Accordingly, *the second goal of this thesis is to develop a high-precision magnetic field measuring system to determine the field distributions in the fine magnetic pole pitch.* It combines a precise Gauss meter, a Hall-effect probe, a probe holder, a PCB sample holder, an X-Y micro-stage, and an X-Y-Z micro-stage. All of them are mounted on an optical table to prevent vibrations.

1.6 Organization of this dissertation

This dissertation is organized as the following : An introduction is reported in Chapter 1. Design and fabrication of a multi-pole magnetic component with a fine

magnetic pole pitch by using the PCB manufacturing technology are discussed in Chapter 2. Both of linear and rotary types of wire circuit patterns are presented to form different multi-pole magnetic components on the PCB. In Chapter 3, the field formulae for computing the magnetic flux density distribution in the fine magnetic pole pitch are derived through the theoretical analysis. In Chapter 4, a precise magnetic field measuring system is designed and set up to determine the field distributions induced from the wire circuits. In Chapter 5, the field enhancement using a dual-layered wire circuit structure is studied to improve the field strength for measurements. The field optimization in the fine magnetic pole pitch is also investigated. Moreover, the field variations along different measuring routes are analyzed in Chapter 6. Finally, the conclusions with a summary of main results and areas for future works in this dissertation are presented in Chapter 7. All programs for computing the field distribution in the fine magnetic pole pitch are given in Appendix.



Chapter 2

Design and fabrication

An innovative method by using the printed circuit board (PCB) manufacturing technology is employed to fabricate a multi-pole magnetic component with a fine magnetic pole pitch of less than 1mm. Neither the precise machining technique or the magnetizing head and magnetization machine is required. This innovative method is not only a simple but also a cost-effective method to enable mass production easily. Additionally, different pole numbers and pitch sizes can be also easily achieved by modifying an appropriate wire circuit pattern on the PCB.



2.1 Introduction

Several technologies have been described to fabricate a multi-pole magnetic component with a fine magnetic pole pitch in Chapter 1. However, the costly and complicated machining technique, magnetizing head and magnetization machine are required. Unfortunately, these techniques are difficult to be held simultaneously. PCB manufacturing technology has been widely used and gained a great success in many products for various industrial applications. More and more electric devices can be placed on a substrate. Consequently, the wire circuit density is thus higher and higher than before. Since the wire circuit fabricated on the PCB is made of copper, it can be treated as composed of many straight wires that are located at different positions on the substrate.

According to electromagnetism [27], an annular magnetic field is induced around

a long and straight wire after applying a steady current, as shown in Fig. 2-1. The magnetic flux density \vec{B} inside the wire is given by

$$\oint \vec{B} \cdot d\vec{l} = \mu_0 I \quad \rightarrow \quad B \cdot 2\pi r = \mu_0 I \frac{\pi r^2}{\pi d^2} \quad \rightarrow \quad \vec{B} = \mu_0 I \frac{r}{2\pi d^2} \hat{f}, \quad (2-1)$$

where r is the distance, d is the radius of the wire, I is the current input, \hat{f} is the unit vector in cylindrical coordinates and μ_0 is the permeability of free space. Outside the wire, the magnetic flux density \vec{B} is proportional to the current input I but inversely proportional to the distance r , and it is

$$\oint \vec{B} \cdot d\vec{l} = \mu_0 I \quad \rightarrow \quad B \cdot 2\pi r = \mu_0 I \quad \rightarrow \quad \vec{B} = \frac{\mu_0 I}{2\pi r} \hat{f}. \quad (2-2)$$

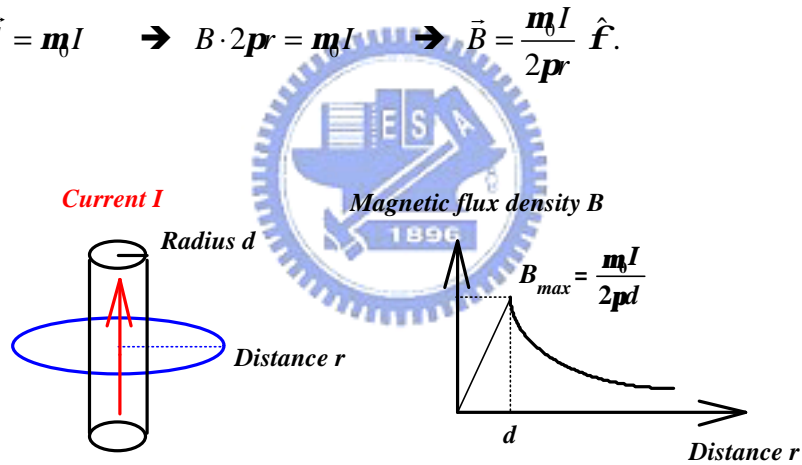


Fig. 2-1. Magnetic flux density distribution in a long and straight wire.

A linear wire circuit pattern with a periodic structure is designed as in Fig. 2-2 (a). This periodic structure provides a loop allowing the current to flow in the opposite directions for inducing different magnetic fields among the wire circuit. Correspondingly, an alternate and regular magnetic flux density distribution is generated when a steady current is applied to the wire circuit, as shown in Fig. 2-2 (b). Thus, a linear type of multi-pole magnetic component with a uniform pole profile is accomplished. Various plus and minus marks denote the induced magnetic field

along different z directions.

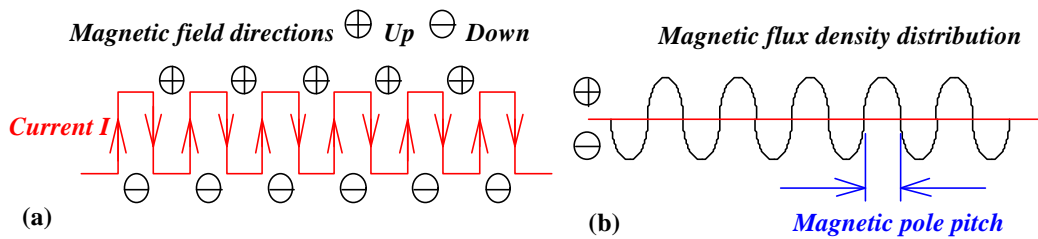


Fig. 2-2. (a) Linear wire circuit pattern with a periodic structure. (b) The magnetic flux density distribution induced from the linear wire circuit pattern.

Annular wire circuit pattern is proposed and illustrated in Fig. 2-3 (a) to produce different magnetic fields in the radial direction. An annular multi-pole magnetic field distribution is obtained after applying a steady current to the annular wire circuit, as shown in Fig. 2-3 (b). Consequently, a rotary type of multi-pole magnetic component with a uniform pole profile is achieved. It is seen that the different multi-pole magnetic components with a uniform field distribution can be acquired without magnetization. Both of linear and annular wire circuit patterns can be easily fabricated on the PCB for different applications.

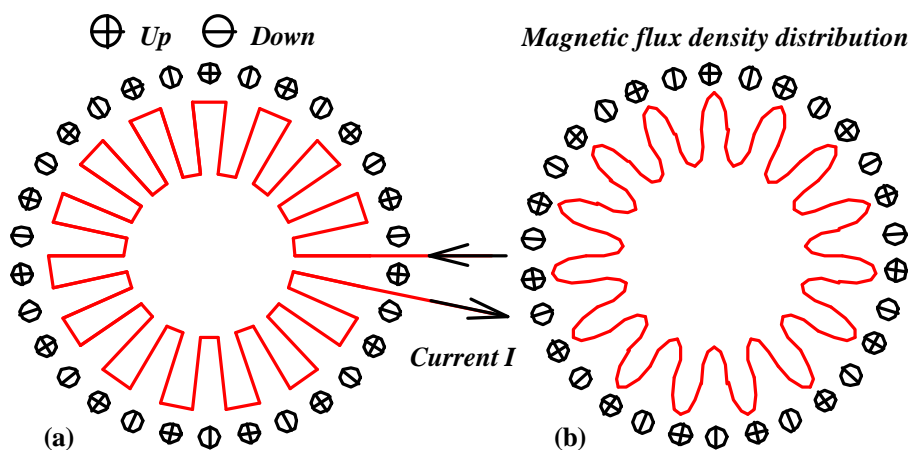


Fig. 2-3. (a) Annular wire circuit pattern with a multi-pole configuration in the radial direction. (b) The magnetic flux density distribution induced from the annular wire circuit pattern.

Currently, the minimum wire width and the gap between any two adjacent wires on the circuit can be achieved about 3mils ($\sim 75\mu\text{m}$, $1\text{mil} = 25.4\mu\text{m}$) through the PCB manufacturing technology. Accordingly, it is highly possible and feasible to fabricate a multi-pole magnetic component with a fine magnetic pole pitch of less than 1mm. A comparison among different methods in fabricating a multi-pole magnetic component with a fine magnetic pole pitch is summarized on Table 2-1.

Table 2-1 Comparison among different methods

Basic requirements Methods	Precise machining	Magnetizing head	Magnetization machine	Minimum pole pitch	Cost
Conventional magnetization	Yes	Yes	Yes	1mm	High
Single-pulse magnetization	Yes	Yes	Yes	$100\mu\text{m}$	Very high
PCB manufacturing technology	No	No	No	$\sim 150\mu\text{m}$	Low

Obviously, all precise machining technique, magnetizing head and magnetization machine are necessary in conventional and single-pulse magnetization methods. The manufacturing cost is thus very high and the minimum pitch sizes are around 1mm and $100\mu\text{m}$, respectively. However, the innovative method of PCB manufacturing technology provides a simple process to fabricate a multi-pole magnetic component with a fine magnetic pole pitch, neither the precise machining technique nor the magnetizing head and magnetization machine is required. The magnetic pole pitch can be minimized to around $150\mu\text{m}$. Although this pitch size is slightly larger than $100\mu\text{m}$ produced by using the single-pulse magnetization method, it has been significantly reduced to be smaller than 1mm.

From above discussions, PCB manufacturing technology is not only a simple but also a feasible and convenient method to fabricate a multi-pole magnetic component with a fine magnetic pole pitch. Consequently, PCB manufacturing technology is

hired to narrow the magnetic pole pitch to be less than 1mm for this dissertation work. The detailed design and fabrication process will be discussed in the following sections.

2.2 Design

A special wire circuit pattern was designed as in Fig. 2-4. All dimensions of wire segments on the circuit should be taken into account to obtain a desired pitch size. The spacing between any two adjacent wires is defined as the gap G . The sum of wire width $T1$ and gap G is defined as the magnetic pole pitch. A straight wire d on both sides is designed to connect to the current source. Various wire segments of a and b are related by $L=a+b$. The segment a is equal to b at the condition along the bisection line.

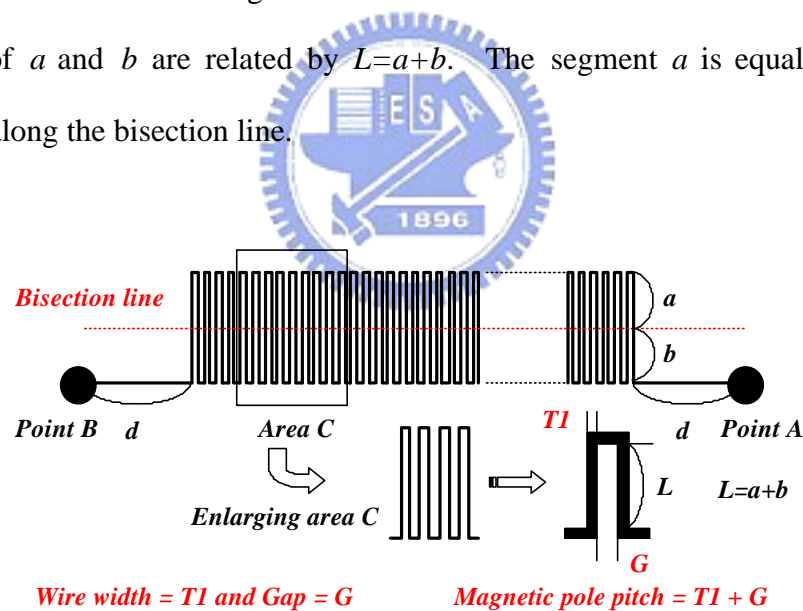


Fig. 2-4. Special wire circuit pattern designed for fabricating a multi-pole magnetic component with a fine magnetic pole pitch.

The schematic view of the cross section on the special wire circuit pattern along the bisection line is illustrated in Fig. 2-5 (a), indicating the wire thickness is $T2$. According to *Ampere's law*, an alternate and regular magnetic field distribution is induced after applying a steady current to the wire circuit, as shown in Fig. 2-3 (b).

Thus, a multi-pole magnetic component with a fine magnetic pole pitch is obtained. Additionally, different pole numbers and pitch sizes can be also easily achieved by designing an appropriate wire circuit pattern.

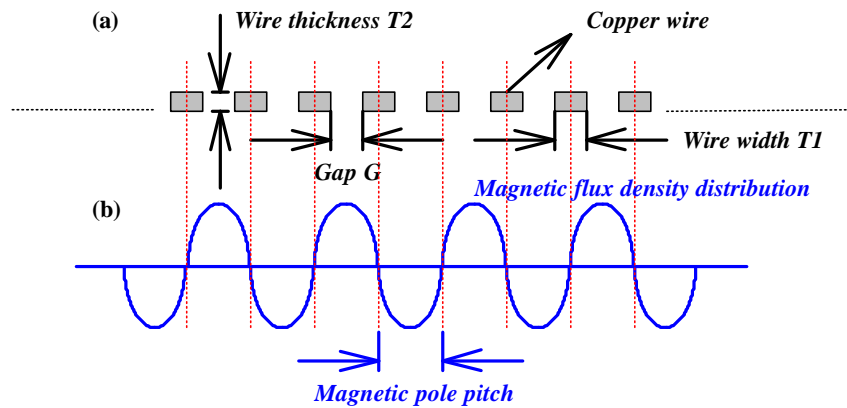


Fig. 2-5. (a) Schematic view of the cross section on the special wire circuit pattern along the bisection line. (b) The magnetic flux density distribution generated from the special wire circuit pattern.

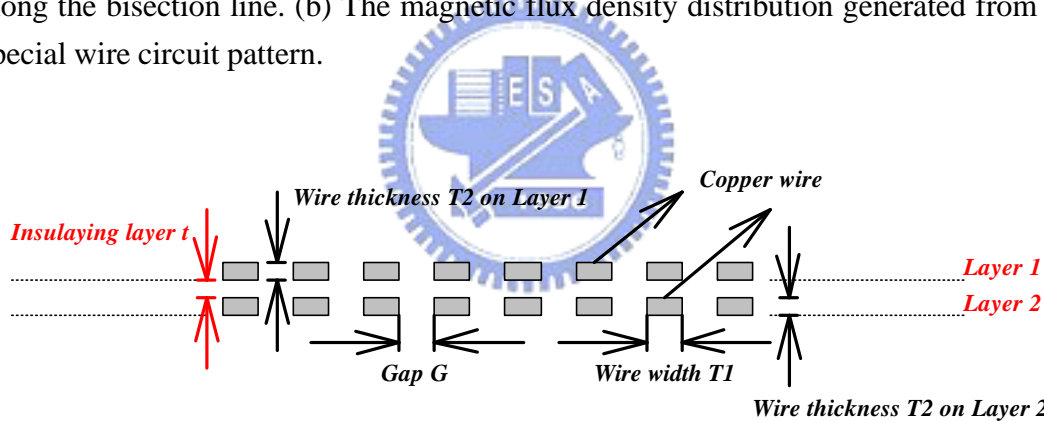


Fig. 2-6. Schematic view of the cross section on a dual-layered wire circuit structure along the bisection line.

A dual-layered wire circuit structure is considered to enhance the field strength in the fine magnetic pole pitch. Figure 2-6 shows the schematic view of the cross section on a dual-layered wire circuit structure along the bisection line. The geometrical structures of single-layered and dual-layered wire circuits are depicted in Fig. 2-7. An insulating layer t is inserted between two layers in the dual-layered wire circuit structure to prevent a short circuit. Both of *Layer 1* and *Layer 2* induce

the magnetic fields simultaneously after applying a steady current to the wire circuit. The total magnetic field is the sum of *Layer 1* and *Layer 2*. Consequently, the field strength can be effectively enhanced using the dual-layered wire circuit structure. The large field strength in the wire circuit is useful to the signal detection. The details can be found in Chapter 5. Both of single-layered and dual-layered wire circuit structures can be easily realized through the PCB manufacturing technology.

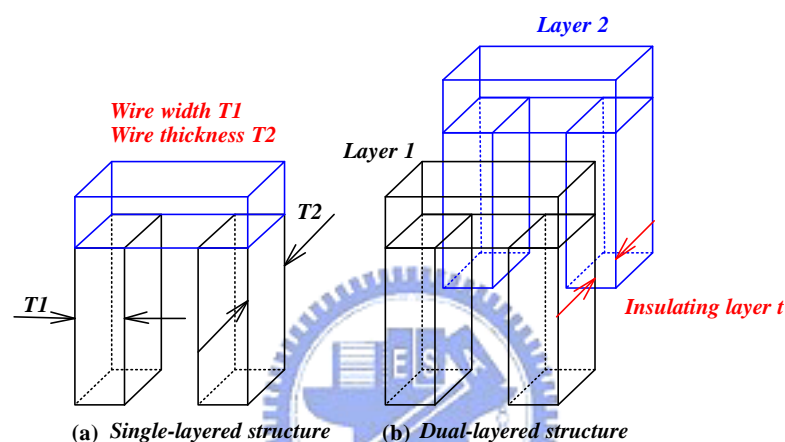


Fig. 2-7. Geometrical structures of (a) single-layered and (b) dual-layered wire circuits.

2.3 Fabrication

2.3.1 Drawing

First, the special wire circuit pattern with an appropriate layout must be designed and drawn by using drawing software such as AutoCAD, SolidWorks or Pro/E, etc. [28-30]. Here, AutoCAD is employed to do this job. In this step, the wire width, gap and corresponding position must be drawn and arranged accurately to acquire the desired pitch size and pole number.

Various gaps of $150\mu\text{m}$ and $200\mu\text{m}$ with a wire width of $100\mu\text{m}$ are used to design

different magnetic pole pitches of $250\mu\text{m}$ and $300\mu\text{m}$ on nine-pole magnetic components, as shown in Figs. 2-8 (a) and (b). The drawings of nine-pole magnetic components also have different fine magnetic pole pitches of $250\mu\text{m}$ and $300\mu\text{m}$ by using another wire width of $125\mu\text{m}$ with various gaps of $125\mu\text{m}$ and $175\mu\text{m}$, as illustrated in Figs. 2-8 (c) and (d). Four holes located at corners are designed to fix the sample in measurements. Both of *Point A* and *Point B* are drawn for connecting to the current source.

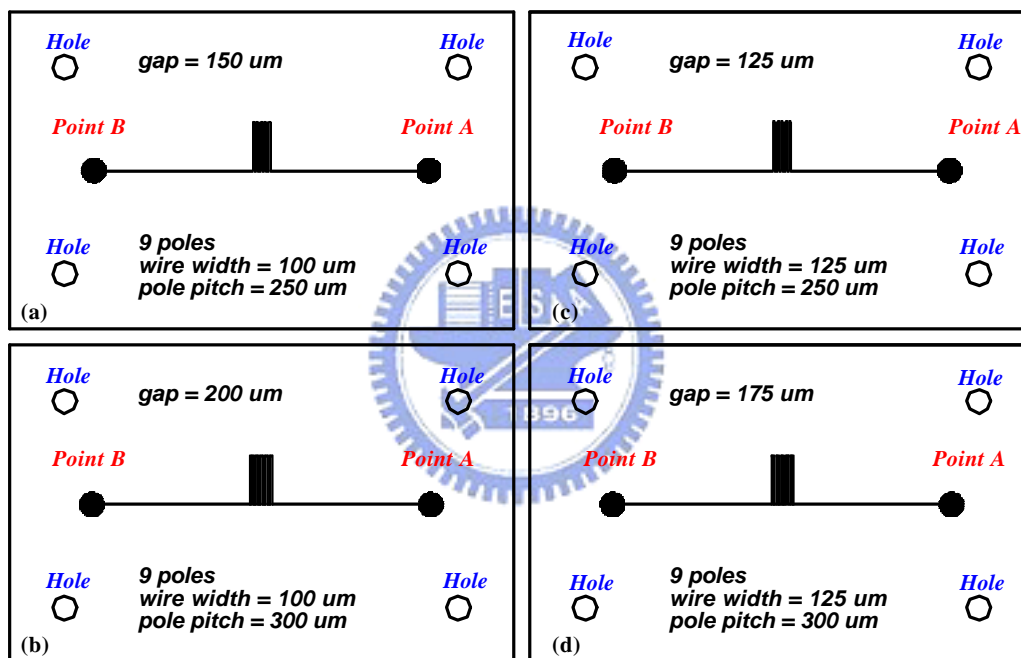


Fig. 2-8. Various drawings of nine-pole magnetic components with different fine magnetic pole pitches of (a) $250\mu\text{m}$ by using a wire width of $100\mu\text{m}$ and a gap of $150\mu\text{m}$, (b) $300\mu\text{m}$ by using a wire width of $100\mu\text{m}$ and a gap of $200\mu\text{m}$, (c) $250\mu\text{m}$ by using a wire width of $125\mu\text{m}$ and a gap of $125\mu\text{m}$, and (d) $300\mu\text{m}$ by using a wire width of $125\mu\text{m}$ and a gap of $175\mu\text{m}$.

The circuit layout software such as OrCAD, Protel or PowerPCB, etc. can be used for the unit transformation to meet the specific requirement of PCB manufacturing process [31-33]. Here, PowerPCB is selected to proceed the assigned task. Several standard file formats are acceptable for fabricating the wire circuit and the most

common is Gerber file format. The wire circuit patterns can be easily transferred to the substrate through using Gerber files.

2.3.2 Wire circuit manufacturing process

Before starting the process, a mask with the special wire circuit pattern must be prepared by using Gerber files. The mask is like a film used in conventional cameras. Nine-pole and nineteen-pole wire circuit masks are demonstrated in Figs. 2-9 (a) and (b), respectively.

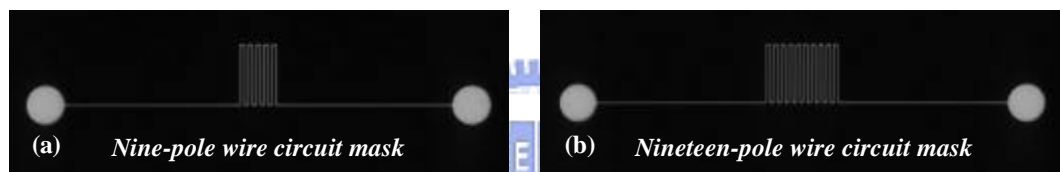


Fig. 2-9 (a) Nine-pole and (b) nineteen-pole wire circuit masks.

The flow charts of wire circuit manufacturing process in fabricating the multi-pole magnetic component with a fine magnetic pole pitch is illustrated in Fig. 2-10 [34]. In the step (a), a copper film with a standard thickness is adhered to the surface of the substrate. The surface of the copper film is very flat and its thickness can be increased through an electroplating process. Usually the substrate material is made of glass epoxy (FR4) which has good electric and heat insulation. The surface of the copper film should be cleaned up to be free from dusts. A photoresist layer is then applied to the surface of the copper film in the step (b).

The subsequent procedures are heating and curing the photoresist layer on the substrate. There are two kinds of photoresist, which are positive and negative. The positive photoresist will dissolve after light exposure and the negative photoresist will

not. Here, the positive photoresist is selected to transfer the wire circuit pattern. The most popular method of coating the photoresist used in the process is so-called “Dry Film”. Using a hot roll laminator, the Dry Film can be laminated on the substrate and easily automated. Moreover, the Dry Film lamination is not sensitive to the cleanness, so this process is now popular for the fine wire manufacturing.

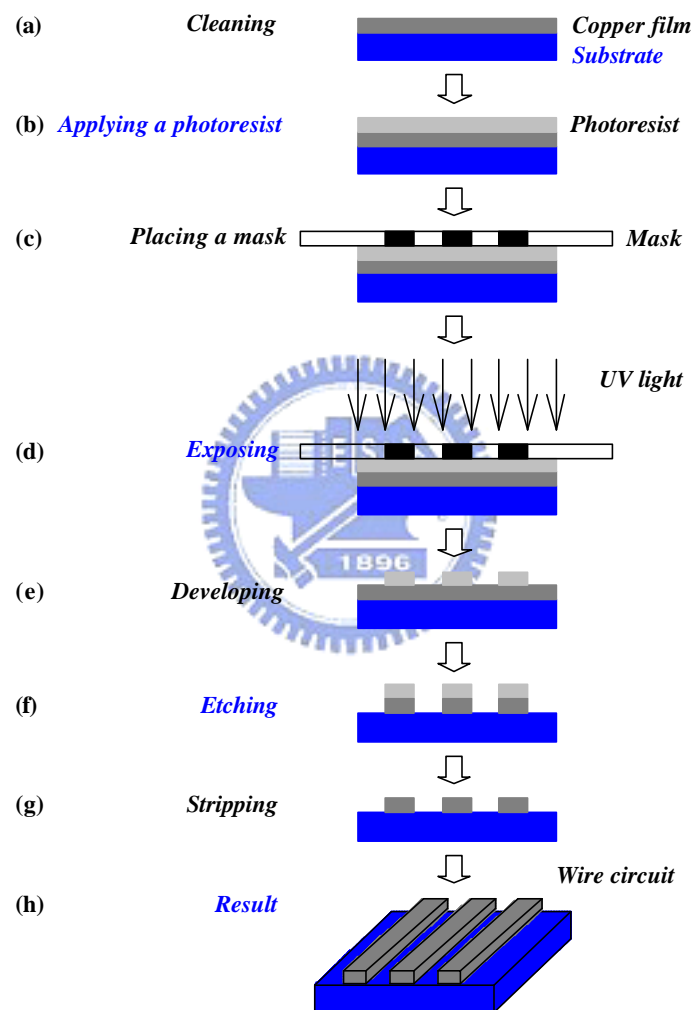


Fig. 2-10. Flow charts of wire circuit manufacturing process. (a) The surface of the copper film is cleaned up to be free from dusts. (b) A photoresist layer is applied to the surface of the copper film. (c) A pre-prepared mask is placed on the top of the photoresist layer. (d) The UV light is employed to proceed the light exposure process. (e) The non-exposed area is removed through a developing process. (f) The copper film at the exposed area is removed by chemical reaction using an etching solvent. (g) The residual photoresist on the surface of the wire circuit is stripped. (h) The wire circuit is accomplished on the substrate.

Subsequent steps of (c) and (d), a pre-prepared mask is placed on the top of the photoresist layer to proceed the light exposure process by using ultraviolet (UV) light. The special wire circuit pattern on the mask is transferred to the substrate after UV light exposure. The wire circuit pattern is then formed from removing the photoresist at the non-exposed area through the developing process (e). In the etching process (f), the copper film at the exposed area is removed by chemical reaction using an etching solvent such as ferric chloride, alkaline ammonia, cupric chloride, etc. The special wire circuit pattern is thus appeared on the substrate. Further steps of (g) and (h), the residual photoresist is stripped using a solvent so that a real wire circuit is accomplished on a substrate. A very thin thickness of gold (Au) is coated on the surface of copper wires to prevent oxidation.

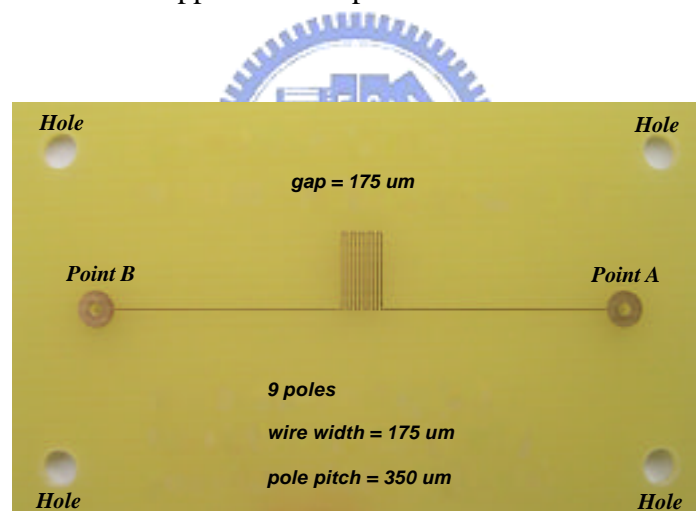


Fig. 2-11. A nine-pole magnetic component fabricated on the PCB with a fine magnetic pole pitch of $350\mu\text{m}$ by using a wire width of $175\mu\text{m}$ and a gap of $175\mu\text{m}$.

A nine-pole magnetic component with a fine magnetic pole pitch of $350\mu\text{m}$ fabricated on the PCB by using a wire width of $175\mu\text{m}$ and a gap of $175\mu\text{m}$ is demonstrated in Fig. 2-11. Four holes located at corners are drilled in order to fix the sample for measurements. Two small holes inside *Point A* and *Pont B* are drilled as well to connect to the current source. All holes and shapes of wire circuit samples

are made through using CNC (computer numerical control) machine. Figure 2-12 shows another example of 29-pole magnetic component with a fine magnetic pole pitch of $500\mu\text{m}$ by using a wire width of $225\mu\text{m}$ and a gap of $275\mu\text{m}$.

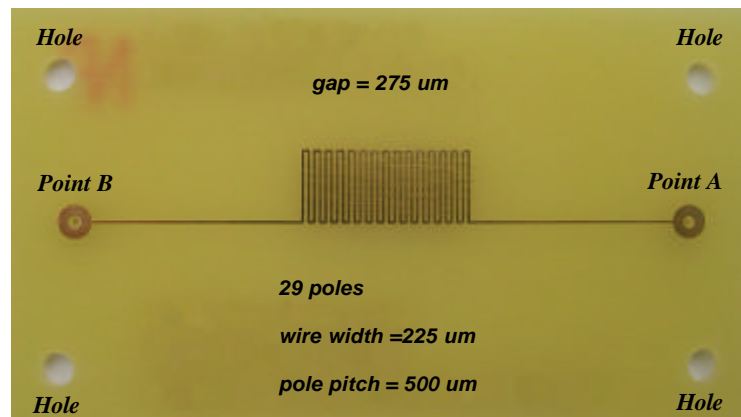


Fig. 2-12. A 29-pole magnetic component fabricated on the PCB with a fine magnetic pole pitch of $500\mu\text{m}$ by using a wire width of $225\mu\text{m}$ and a gap of $275\mu\text{m}$.

2.4 Summary



PCB manufacturing technology has been demonstrated to effectively narrow the magnetic pole pitch to be less than 1mm. This innovative method provides a simple process to fabricate the multi-pole magnetic component without using the complicated machining technique, magnetizing head and magnetization machine. It is also a cost-effective method to enable mass production easily. Additionally, different pole numbers and pitch sizes can be also easily fabricated on the PCB through this flexible approach.

Chapter 3

Theoretical analysis

Several methods are applicable to compute the induced magnetic field in the fine magnetic pole pitch fabricated on the PCB due to the current input. The field distribution of a straight wire with a finite length can be easily acquired by using *Biot-Savart law*. The integral of magnetic flux density is evaluated numerically by discretizing the volume into a mesh of elements. The wire circuit fabricated on the PCB can be treated as composed of many straight wires with a finite length that are located at different positions on the substrate. Consequently, the total magnetic flux density induced from the wire circuit can be obtained after accumulating the contribution of each straight wire. All obtained field formulae in this chapter are derived from a basic assumption of a uniform current density through the wire circuit.

3.1 Long and straight wire

An element dl in a long and straight wire carrying a steady current I is shown in Fig. 3-1. According to *Biot-Savart law*, the magnetic flux density at the point P is

$$d\vec{B} = \frac{\mu_0 I}{4\pi} \frac{dl \sin \alpha}{r^2} \hat{\mathbf{f}} = \frac{\mu_0 I}{4\pi} \frac{dl \cos \theta}{r^2} \hat{\mathbf{f}}, \quad (3-1)$$

where μ_0 is the permeability of free space and $\hat{\mathbf{f}}$ is the unit vector in cylindrical coordinates. The relative orientations of current I and magnetic flux density \vec{B}

satisfy the right-hand screw rule. Here

$$l = r \tan \mathbf{a}, \quad \tilde{n} = r \cos \mathbf{a}, \quad dl = \tilde{n} \frac{d\mathbf{a}}{\cos^2 \mathbf{a}} = \frac{r^2 d\mathbf{a}}{\tilde{n}}. \quad (3-2)$$

Thus, from Eq. (3-1)

$$\vec{B} = \frac{\mu_0 I}{4\pi r} \int_{-\pi/2}^{+\pi/2} \cos \mathbf{a} d\mathbf{a} \hat{\mathbf{f}} = \frac{\mu_0 I}{2\pi r} \hat{\mathbf{f}}. \quad (3-3)$$

Lines of the magnetic flux density \vec{B} are circles lying in a plane perpendicular to the straight wire and centered on it. The magnitude of magnetic flux density \vec{B} falls off as $1/r$ [36].

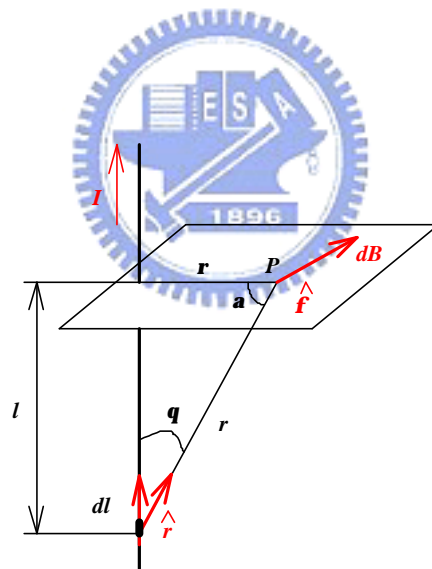


Fig. 3-1. Long and straight wire carrying a steady current I , the element dl contributes a $d\vec{B}$ at the point P .

3.2 Straight wire with a finite length L

3.2.1 Point P located outside the straight wire

An element dz' in a straight wire with a finite length L carrying a steady current I is

illustrated in Fig. 3-2. Wire segments of a and b are related by $L=a+b$, and the diameter of the straight wire is d .

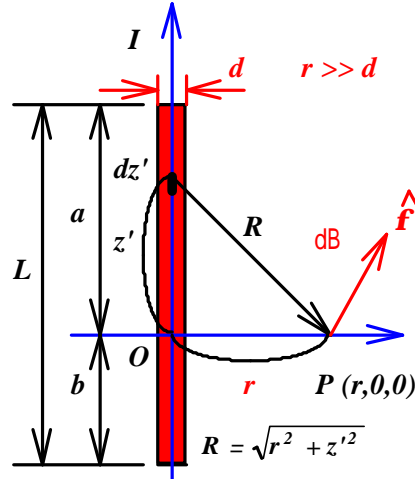


Fig. 3-2. A straight wire with a finite length L carrying a steady current I , the element dz' contributes a $d\vec{B}$ at the point P located outside the straight wire.

At the point P , the magnetic flux density $d\vec{B}$ is given by

$$d\vec{B} = \frac{\mu_0 I}{4\pi} \frac{d\vec{l} \times \hat{R}}{R^2} \hat{f} = \frac{\mu_0 I}{4\pi} \frac{d\vec{l} \times \vec{R}}{R^3} \hat{f}, \quad (3-4)$$

and here

$$R = \sqrt{r^2 + z'^2}, \quad d\vec{l} = dz' \hat{z}, \quad \vec{R} = r\hat{r} - z'\hat{z}, \quad d\vec{l} \times \vec{R} = rdz' \hat{f}. \quad (3-5)$$

The distance r is assumed $r \gg d$. A special integration formula [37] is used to calculate Eq. (3-4) and it is

$$\int \frac{dx}{\sqrt{(x^2 \pm a^2)^{3/2}}} = \frac{1}{a^2} \frac{\pm x}{\sqrt{x^2 \pm a^2}}. \quad (3-6)$$

Thus, from Eq. (3-4) to Eq. (3-6)

$$\begin{aligned}\vec{B} &= \frac{\mu_0 I}{4\pi} \int_{-b}^{+a} \frac{rdz'}{(r^2+z'^2)^{3/2}} \hat{f} = \frac{\mu_0 I}{4\pi} \frac{r}{r^2} \frac{z'}{\sqrt{z'^2+r^2}} \Big|_{-b}^a \hat{f} \\ &= \frac{\mu_0 I}{4\pi r} \left(\frac{a}{\sqrt{a^2+r^2}} + \frac{b}{\sqrt{b^2+r^2}} \right) \hat{f}.\end{aligned}\quad (3-7)$$

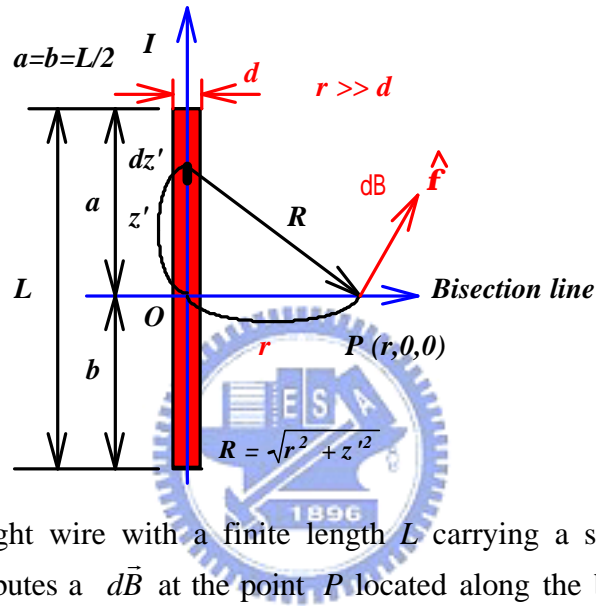


Fig. 3-3. A straight wire with a finite length L carrying a steady current I , the element dz' contributes a $d\vec{B}$ at the point P located along the bisection line of the straight wire.

3.2.2 Point P located along the bisection line of the straight wire

The magnetic flux density at the point P located along the bisection line ($a=b=L/2$) of the straight wire in Fig. 3-3 can be calculated by Eq. (3-7) and given by

$$\begin{aligned}\vec{B} &= \frac{\mu_0 I}{4\pi} \int_{-b}^{+a} \frac{rdz'}{(r^2+z'^2)^{3/2}} \hat{f} = \frac{\mu_0 I}{4\pi} \frac{r}{r^2} \frac{z'}{\sqrt{z'^2+r^2}} \Big|_{-b}^a \hat{f} \\ &= \frac{\mu_0 I}{4\pi r} \left(\frac{a}{\sqrt{a^2+r^2}} + \frac{b}{\sqrt{b^2+r^2}} \right) \hat{f} = \frac{\mu_0 I}{2\pi r} \left(\frac{L/2}{\sqrt{(L/2)^2+r^2}} \right) \hat{f}.\end{aligned}\quad (3-8)$$

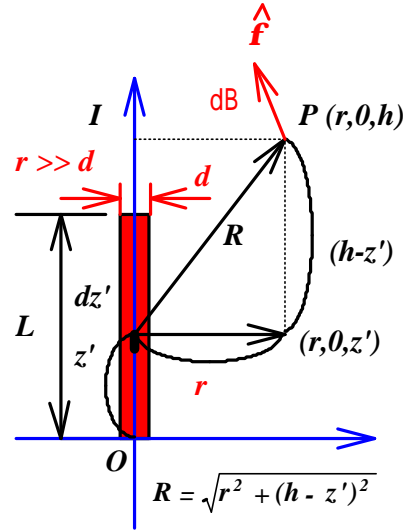


Fig. 3-4. A straight wire with a finite length L carrying a steady current I , the element dz' contributes a $d\vec{B}$ at the point P located at the upper position of the straight wire.

3.2.3 Point P located at the upper position of the straight wire

The magnetic flux density at the point P located at the upper position of the straight wire in Fig. 3-4 can be obtained and here

$$R = \sqrt{r^2 + (h - z')^2}, \quad d\vec{l} = dz' \hat{z}, \quad \vec{R} = r\hat{r} + (h - z')\hat{z}, \quad (3-9)$$

$$d\vec{l} \times \vec{R} = dz' \hat{z} \times [r\hat{r} + (h - z')\hat{z}] = rdz' \hat{f}. \quad (3-10)$$

Thus, from Eq. (3-4)

$$\begin{aligned} \vec{B} &= \frac{\mu_0 I}{4\pi} \int_0^L \frac{rdz'}{[r^2 + (h - z')^2]^{3/2}} \hat{f} = \frac{\mu_0 I}{4\pi} \int_0^L \frac{-rd(h - z')}{[r^2 + (h - z')^2]^{3/2}} \hat{f} \\ &= \frac{\mu_0 I}{4\pi} \frac{-r}{r^2} \left. \frac{h - z'}{\sqrt{(h - z')^2 + r^2}} \right|_0^L \hat{f} = \frac{\mu_0 I}{4\pi r} \left(\frac{h}{\sqrt{h^2 + r^2}} - \frac{h - L}{\sqrt{(h - L)^2 + r^2}} \right) \hat{f}. \end{aligned} \quad (3-11)$$

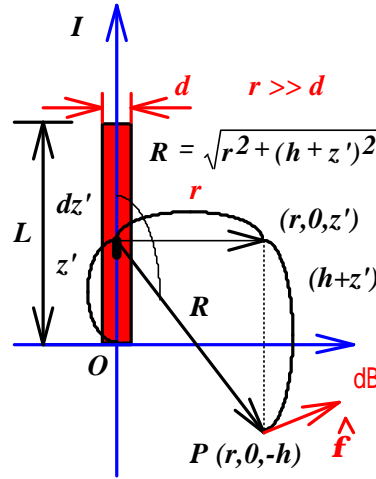


Fig. 3-5. A straight wire with a finite length L carrying a steady current I , the element dz' contributes a $d\vec{B}$ at the point P located at the lower position of the straight wire.

3.2.4 Point P located at the lower position of the straight wire

The magnetic flux density at the point P located at the lower position ($h=-h$) of the straight wire in Fig. 3-5 can be acquired by Eq. (3-11) and given by

$$\begin{aligned}\vec{B} &= \frac{\mu_0 I}{4\pi} \int_0^L \frac{rdz'}{[r^2 + (h+z')^2]^{3/2}} \hat{f} = \frac{\mu_0 I}{4\pi} \int_0^L \frac{rd(h+z')}{[r^2 + (h+z')^2]^{3/2}} \hat{f} \\ &= \frac{\mu_0 I}{4\pi} \frac{r}{r^2} \frac{h+z'}{\sqrt{(h+z')^2 + r^2}} \Big|_0^L \hat{f} = \frac{\mu_0 I}{4\pi} \left(\frac{h+L}{\sqrt{(h+L)^2 + r^2}} - \frac{h}{\sqrt{h^2 + r^2}} \right) \hat{f}. \quad (3-12)\end{aligned}$$

3.3 Two-dimensional analysis

Eq. (3-1) to Eq. (3-12) are derived from a hypothesis of the distance $r \gg d$, and therefore the diameter d of the straight wire can be neglected in calculation. However, the diameter d should be taken into account when $r \approx d$. The cross section of a straight wire fabricated on the PCB is not circular but rectangular, which

can be divided into a mesh of indexed elements, as shown in Fig. 3-6. These elements are equal in area containing the same amount of current density i .

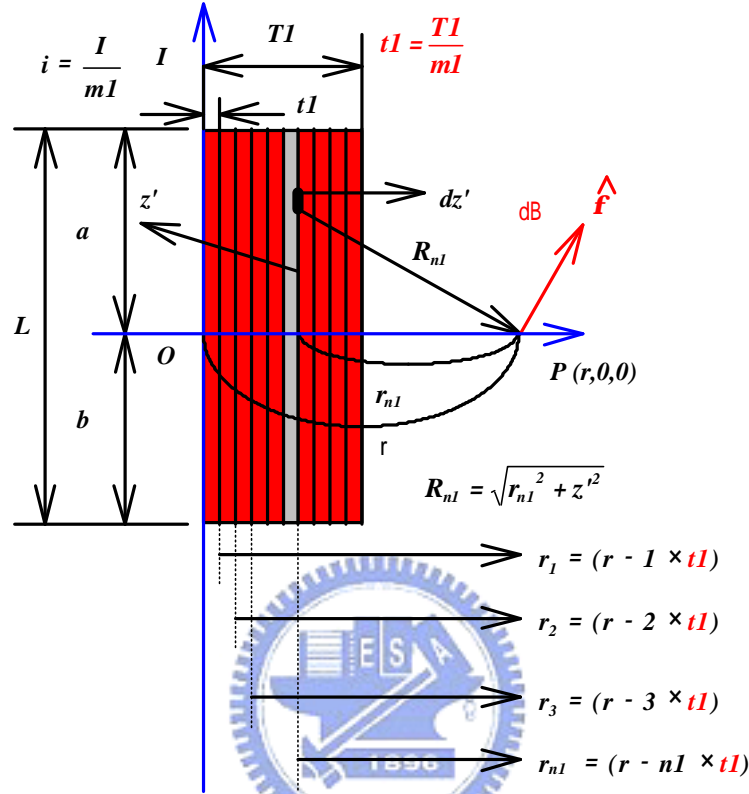


Fig. 3-6. Mesh of a straight wire with a finite length L carrying a steady current I and the wire width $Tl \approx r$. The distance r_{nl} decreases slightly with a small tl .

Here only the wire width Tl is taken into account and $Tl \approx r$. Each element is a straight wire with a finite length L . Consequently, the induced magnetic flux density can be calculated by Eq. (3-7). The integral of magnetic flux density is evaluated numerically by discretizing the surface into a mesh of indexed elements. After summing the contribution of each element, the total magnetic flux density \bar{B} produced by the straight wire at the point P is obtained and given by

$$\bar{B} = \sum_{n1=1}^{m1} \frac{m1i}{4\pi r_{n1}} \left(\frac{a}{\sqrt{a^2 + r_{n1}^2}} + \frac{b}{\sqrt{b^2 + r_{n1}^2}} \right) \hat{f} \quad (n1=1 \sim m1), \quad (3-13)$$

where $n1$ is an interger, $m1$ is the “mesh” parameter that characterizes the discretization of wire width $T1$. Wire segments of a and b are related by $L=a+b$.

Paramters of current density i and distance r_{n1} are given by

$$i = \frac{I}{m1}, \quad r_{n1} = (r - n1 \times t1), \quad t1 = \frac{T1}{m1}. \quad (3-14)$$

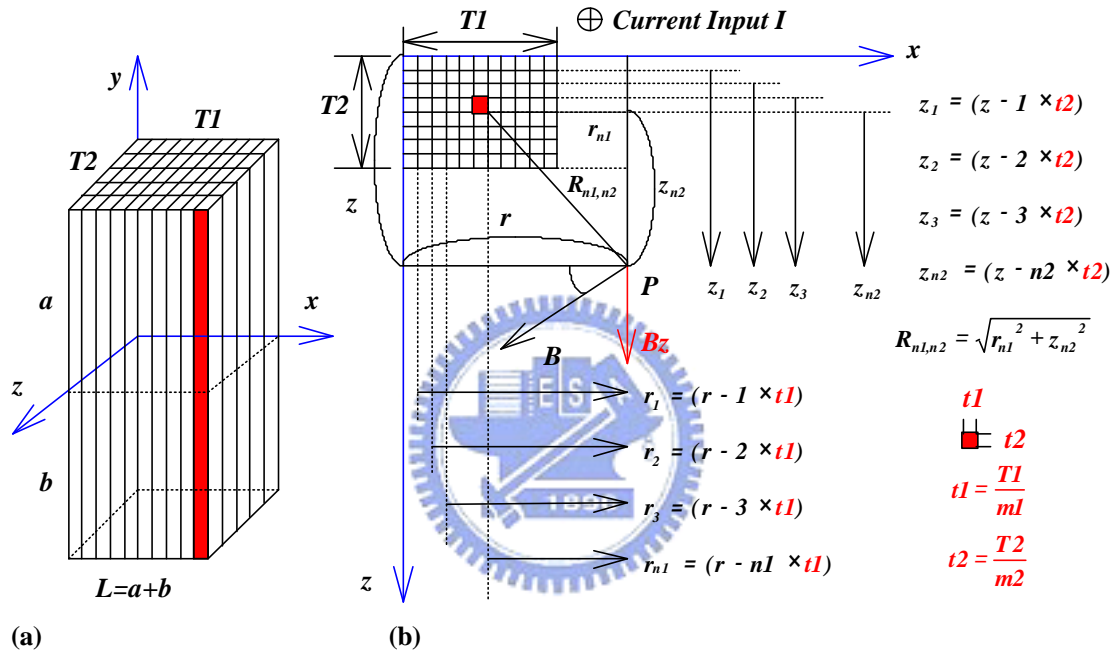


Fig. 3-7. (a) Mesh and (b) corresponding positions of all elements of a straight wire with a wire width $T1 \approx r$ and a wire thickness $T2 \approx r$ carrying a steady current I . The distances of r_{n1} and z_{n2} decrease slightly with a small $t1$ and $t2$, respectively.

3.4 Three-dimensional analysis

The wire thickness $T2$ also needs to be taken into account in calculation when $T2 \approx r$, as illustrated in Fig. 3-7 (a). The integral of magnetic flux density in Eq. (3-7) can be evaluated numerically by discretizing the volume into a mesh of indexed elements. The corresponding positions of all elements are indicated in Fig. 3-7 (b). After summing the contribution of each element, the total magnetic flux density \vec{B}

produced by the straight wire at the point P in the z direction is given by

$$B_z = \sum_{n1=1}^{m1} \sum_{n2=1}^{m2} \frac{m1 i}{4 \pi R_{n1,n2}} \times \left(\frac{a}{\sqrt{a^2 + R_{n1,n2}^2}} + \frac{b}{\sqrt{b^2 + R_{n1,n2}^2}} \right) \times \sin \mathbf{q}, \quad (3-15)$$

where $n1$ and $n2$ are intergers, $m1$ and $m2$ are “mesh” parameters that characterize the discretization of wire width $T1$ and wire thickness $T2$, and \mathbf{q} is the angular offset of the X-axis. Wire segments of a and b are also related by $L=a+b$. Paramters of current density i , distance $R_{n1,n2}$ and $\sin \mathbf{q}$ are

$$i = \frac{I}{m1 \cdot m2}, \quad R_{n1,n2} = \sqrt{r_{n1}^2 + z_{n2}^2}, \quad \sin \mathbf{q} = \frac{r_{n1}}{R_{n1,n2}}, \quad (3-16)$$

and here



$$r_{n1} = (r - n1 \times t1), \quad t1 = \frac{T1}{m1}, \quad (3-17)$$

$$z_{n2} = (z - n2 \times t2), \quad t2 = \frac{T2}{m2}, \quad (n1 = 1 \sim m1, n2 = 1 \sim m2). \quad (3-18)$$

3.5 Field analysis

The wire circuit designed in Fig. 2-4 was redrawn as in Fig. 3-8 (a) in order to analyze the field distribution in the fine magnetic pole pitch. The red arrows indicate the current flow in the wire circuit. Various plus and minus marks denote the induced magnetic field along different z directions. Both of wire width $T1$ and wire thickness $T2$ are taken into account simultaneously. The wire segment w is related

by $w=2 Tl+G$.

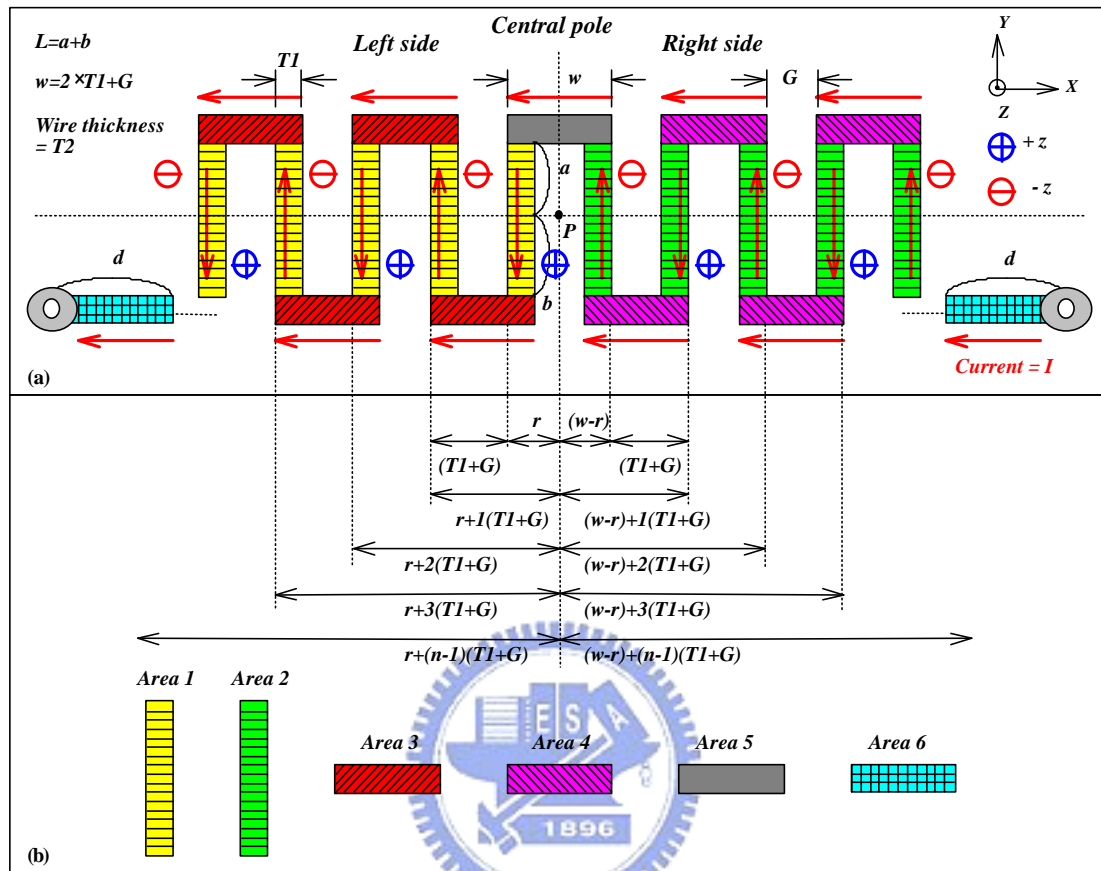


Fig. 3-8. (a) Geometrical structure, current loop and induced field direction of the wire circuit. (b) Corresponding positions of each segment and six areas indicated with different colors for study separately.

Each wire segment can be treated as a straight wire with a finite length carrying a steady current I . Consequently, the magnetic flux density can be calculated by Eq. (3-15). After accumulating the contribution of each wire segment, the total magnetic flux density at the point P in the wire circuit can be obtained. All corresponding positions of wire segments and six areas with different colors illustrated in Fig. 3-8 (b) are used to derive the formulae for calculating the field distribution. Details of deriving process for each area are discussed in the following sections.

3.5.1 At Area 1

According to Eq. (3-4) and Eq. (3-15), the induced magnetic flux density in the z direction of B_{zA1} at Area 1 is given by

$$B_{zA1} = \sum_{n=1}^m \sum_{n2=1}^{m2} \sum_{n1=1}^{m1} \frac{\mathbf{m}_0 i}{4\pi R_{A1}} \times \left(\frac{a}{\sqrt{a^2 + R_{A1}^2}} + \frac{b}{\sqrt{b^2 + R_{A1}^2}} \right) \times \sin \mathbf{q}_{A1} \times (-1)^{n-1} \quad (n = 1 \sim m), \quad (3-19)$$

where n , $n1$ and $n2$ are intergers, $m1$ and $m2$ are “mesh” parameters that characterize the discretization of wire width $T1$ and wire thickness $T2$, m is the number of wire segments at Area 1, and \mathbf{q}_{A1} is the angular offset. Paramters of current density i , distance R_{A1} and $\sin \mathbf{q}_{A1}$ are

$$i = \frac{I}{m1 \cdot m2}, \quad R_{A1} = \sqrt{r_{A1}^2 + z_{A1}^2}, \quad \sin \mathbf{q}_{A1} = \frac{r_{A1}}{R_{A1}}, \quad (3-20)$$

and here

$$r_{A1} = (r - n1 \times t1) + (n - 1)(T1 + G), \quad t1 = \frac{T1}{m1}, \quad z_{A1} = z - n2 \times t2, \quad t2 = \frac{T2}{m2}. \quad (3-21)$$

3.5.2 At Area 2

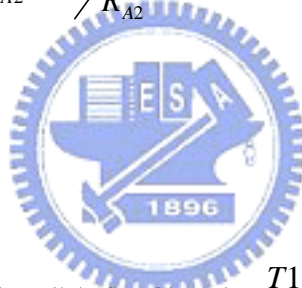
According to Eq. (3-4) and Eq. (3-15), the induced magnetic flux density in the z direction of B_{zA2} at Area 2 is given by

$$B_{zA2} = \sum_{n=1}^m \sum_{n2=1}^{m2} \sum_{n1=1}^{m1} \frac{m_i}{4pR_{A2}} \times \left(\frac{a}{\sqrt{a^2 + R_{A2}^2}} + \frac{b}{\sqrt{b^2 + R_{A2}^2}} \right) \times \sin \mathbf{q}_{A2} \times (-1)^{n-1} \quad (n=1 \sim m), \quad (3-22)$$

where n , $n1$ and $n2$ are intergers, $m1$ and $m2$ are “mesh” parameters that characterize the discretization of wire width $T1$ and wire thickness $T2$, m is the number of wire segments at *Area 2*, and \mathbf{q}_{A2} is the angular offset. Paramters of distance R_{A2} and $\sin \mathbf{q}_{A2}$ are

$$R_{A2} = \sqrt{r_{A2}^2 + z_{A2}^2}, \quad \sin \mathbf{q}_{A2} = \frac{r_{A2}}{R_{A2}}, \quad (3-23)$$

and here



$$r_{A2} = [(w-r) - n1 \times t1] + (n-1)(T1+G), \quad t1 = \frac{T1}{m1}, \quad (3-24)$$

$$z_{A2} = z - n2 \times t2, \quad t2 = \frac{T2}{m2}, \quad w = (2 \times T1 + G). \quad (3-25)$$

3.5.3 At the top side of Area 3

According to Eq. (3-11) and Eq. (3-15), the induced magnetic flux density in the z direction of B_{zA3t} at the top side of *Area 3* is given by

$$B_{zA3t} = \sum_{n=3}^m \sum_{n2=1}^{m2} \sum_{n1=1}^{m1} \frac{m_i}{4pR_{A3t}} \times \left(\frac{h_{A3t}}{\sqrt{h_{A3t}^2 + R_{A3t}^2}} \right)$$

$$-\frac{h_{A3t} - w}{\sqrt{(h_{A3t} - w)^2 + R_{A3t}^2}} \times \sin \mathbf{q}_{A3t} \times (+1) \quad (n = 3, 5, 7 \dots m), \quad (3-26)$$

where n , $n1$ and $n2$ are intergers, $m1$ and $m2$ are “mesh” parameters that characterize the discretization of wire width $T1$ and wire thickness $T2$, m is the number of wire segments at *Area 3* on the top side, and \mathbf{q}_{A3t} is the angular offset. Paramters of distance R_{A3t} and $\sin \mathbf{q}_{A3t}$ are

$$R_{A3t} = \sqrt{r_{A3t}^2 + z_{A3t}^2}, \quad \sin \mathbf{q}_{A3t} = \frac{r_{A3t}}{R_{A3t}}, \quad (3-27)$$

and here

$$r_{A3t} = (T1 + a) - n1 \times t1, \quad t1 = \frac{T1}{m1}, \quad z_{A3t} = z - n2 \times t2, \quad t2 = \frac{T2}{m2}, \quad (3-28)$$

$$h_{A3t} = r + (n-1)(T1 + G) \quad (n = 3, 5, 7 \dots m). \quad (3-29)$$

3.5.4 At the bottom side of *Area 3*

According to Eq. (3-12) and Eq. (3-15), the induced magnetic flux density in the z direction of B_{zA3b} at the bottom side of *Area 3* is given by

$$B_{zA3b} = \sum_{n=2}^m \sum_{n2=1}^{m2} \sum_{n1=1}^{m1} \frac{\mathbf{m}i}{4\mathbf{p}R_{A3b}} \times \left(\frac{h_{A3b}}{\sqrt{h_{A3b}^2 + R_{A3b}^2}} - \frac{h_{A3b} - w}{\sqrt{(h_{A3b} - w)^2 + R_{A3b}^2}} \right) \times \sin \mathbf{q}_{A3b} \times (-1) \quad (n = 2, 4, 6 \dots m), \quad (3-30)$$

where n , $n1$ and $n2$ are intergers, $m1$ and $m2$ are “mesh” parameters that characterize the discretization of wire width $T1$ and wire thickness $T2$, m is the number of wire segments at *Area 3* on the bottom side, and \mathbf{q}_{A3b} is the angular offset. Paramters distance R_{A3b} and $\sin\mathbf{q}_{A3b}$ are

$$R_{A3b} = \sqrt{r_{A3b}^2 + z_{A3b}^2}, \quad \sin\mathbf{q}_{A3b} = \frac{r_{A3b}}{R_{A3b}}, \quad (3-31)$$

and here

$$r_{A3b} = (T1+b) - n1 \times t1, \quad t1 = \frac{T1}{m1}, \quad z_{A3b} = z - n2 \times t2, \quad t2 = \frac{T2}{m2}, \quad (3-32)$$

$$h_{A3b} = r + (n-1)(T1+G) \quad (n = 2,4,6\dots m). \quad (3-33)$$

3.5.5 At the top side of Area 4

According to Eq. (3-12) and Eq. (3-15), the induced magnetic flux density in the z direction of B_{zA4t} at the top side of *Area 4* is given by

$$B_{zA4t} = \sum_{n=3}^m \sum_{n2=1}^{m2} \sum_{n1=1}^{m1} \frac{\mathbf{m}_i}{4\mathbf{p}R_{A4t}} \times \left(\frac{h_{A4t}}{\sqrt{h_{A4t}^2 + R_{A4t}^2}} - \frac{h_{A4t} - w}{\sqrt{(h_{A4t} - w)^2 + R_{A4t}^2}} \right) \times \sin\mathbf{q}_{A4t} \times (+1) \quad (n = 3,5,7\dots m), \quad (3-34)$$

where n , $n1$ and $n2$ are intergers, $m1$ and $m2$ are “mesh” parameters that characterize the discretization of wire width $T1$ and wire thickness $T2$, m is the number of wire

segments at *Area 4* on the top side, and \mathbf{q}_{A4t} is the angular offset. Parameters of distance R_{A4t} and $\sin \mathbf{q}_{A4t}$ are

$$R_{A4t} = \sqrt{r_{A4t}^2 + z_{A4t}^2}, \quad \sin \mathbf{q}_{A4t} = \frac{r_{A4t}}{R_{A4t}}, \quad (3-35)$$

and here

$$r_{A4t} = (T1 + a) - n1 \times t1, \quad t1 = \frac{T1}{m1}, \quad z_{A4t} = z - n2 \times t2, \quad t2 = \frac{T2}{m2}, \quad (3-36)$$

$$h_{A4t} = (w - r) + (n - 1)(T1 + G), \quad w = 2T1 + G, \quad (n = 3, 5, 7 \dots m). \quad (3-37)$$

3.5.6 At the bottom side of *Area 4*

According to Eq. (3-11) and Eq. (3-15), the induced magnetic flux density in the z direction of B_{zA4b} at the bottom side of *Area 4* is given by

$$B_{zA4b} = \sum_{n=2}^m \sum_{n2=1}^{m2} \sum_{n1=1}^{m1} \frac{\mathbf{m}_i}{4\pi R_{A4b}} \times \left(\frac{h_{A4b}}{\sqrt{h_{A4b}^2 + R_{A4b}^2}} - \frac{h_{A4b} - w}{\sqrt{(h_{A4b} - w)^2 + R_{A4b}^2}} \right) \times \sin \mathbf{q}_{A4b} \times (-1) \quad (n = 2, 4, 6 \dots m), \quad (3-38)$$

where n , $n1$ and $n2$ are integers, $m1$ and $m2$ are “mesh” parameters that characterize the discretization of wire width $T1$ and wire thickness $T2$, m is the number of wire segments at *Area 4* on the bottom side, and \mathbf{q}_{A4b} is the angular offset. Parameters distance R_{A4b} and $\sin \mathbf{q}_{A4b}$ are

$$R_{A4b} = \sqrt{r_{A4b}^2 + z_{A4b}^2}, \quad \sin \mathbf{q}_{A4b} = r_{A4b} / R_{A4b}, \quad (3-39)$$

and here

$$r_{A4b} = (T1 + b) - n1 \times t1, \quad t1 = \frac{T1}{m1}, \quad z_{A4b} = z - n2 \times t2, \quad t2 = \frac{T2}{m2}, \quad (3-40)$$

$$h_{A4b} = (w - r) + (n - 1)(T1 + G), \quad w = 2 \times T1 + G, \quad (n = 2, 4, 6 \dots m). \quad (3-41)$$

3.5.7 At Area 5

According to Eq. (3-8) and Eq. (3-15), the induced magnetic flux density in the z direction of B_{zA5} at Area 5 is given by

$$B_{zA5} = \sum_{n2=1}^{m2} \sum_{n1=1}^{m1} \frac{\mathbf{m}i}{4\mathbf{p}R_{A5}} \left(\frac{w-r}{\sqrt{(w-r)^2 + R_{A5}^2}} + \frac{r}{\sqrt{r^2 + R_{A5}^2}} \right) \times \sin \mathbf{q}_{A5}, \quad (3-42)$$

where $n1$ and $n2$ are intergers, $m1$ and $m2$ are “mesh” parameters that characterize the discretization of wire width $T1$ and wire thickness $T2$, and \mathbf{q}_{A5} is the angular offset.

Paramters of distance R_{A5} and $\sin \mathbf{q}_{A5}$ are

$$R_{A5} = \sqrt{r_{A5}^2 + z_{A5}^2}, \quad \sin \mathbf{q}_{A5} = r_{A5} / R_{A5}, \quad (3-43)$$

and here

$$r_{A5} = (T1 + a) - n1 \times t1, \quad t1 = \frac{T1}{m1}, \quad z_{A5} = z - n2 \times t2, \quad t2 = \frac{T2}{m2}. \quad (3-44)$$

3.5.8 At the left side of Area 6

According to Eq. (3-12) and Eq. (3-15), the induced magnetic flux density in the z direction of B_{zA6l} at the left side of Area 6 is given by

$$B_{zA6l} = \sum_{n2=1}^{m2} \sum_{n1=1}^{m1} \frac{m_i}{4\pi R_{A6l}} \left(\frac{h_{A6l}}{\sqrt{h_{A6l}^2 + R_{A6l}^2}} - \frac{h_{A6l} - d}{\sqrt{(h_{A6l} - d)^2 + R_{A6l}^2}} \right) \times \sin \mathbf{q}_{A6l} \times (-1), \quad (3-45)$$

where $n1$ and $n2$ are intergers, $m1$ and $m2$ are “mesh” parameters that characterize the discretization of wire width $T1$ and wire thickness $T2$, and \mathbf{q}_{A6l} is the angular offset.

Paramters of distance R_{A6l} and $\sin \mathbf{q}_{A6l}$ are

$$R_{A6l} = \sqrt{r_{A6l}^2 + z_{A6l}^2}, \quad \sin \mathbf{q}_{A6l} = \frac{r_{A6l}}{R_{A6l}}, \quad (3-46)$$

and here

$$r_{A6l} = (T1 + b) - n1 \times t1, \quad t1 = \frac{T1}{m1}, \quad z_{A6l} = z - n2 \times t2, \quad t2 = \frac{T2}{m2}, \quad (3-47)$$

$$h_{A6l} = r + (m - 1)(T1 + G) + d. \quad (3-48)$$

3.5.9 At the right side of Area 6

According to Eq. (3-11) and Eq. (3-15), the induced magnetic flux density in the z direction of B_{zA6r} at the right side of Area 6 is given by

$$B_{zA6r} = \sum_{n2=1}^{m2} \sum_{n1=1}^{m1} \frac{m_i}{4pR_{A6r}} \left(\frac{h_{A6r}}{\sqrt{h_{A6r}^2 + R_{A6r}^2}} - \frac{h_{A6r} - d}{\sqrt{(h_{A6r} - d)^2 + R_{A6r}^2}} \right) \times \sin \mathbf{q}_{A6r} \times (-1), \quad (3-49)$$

where $n1$ and $n2$ are intergers, $m1$ and $m2$ are “mesh” parameters that characterize the discretization of wire width $T1$ and wire thickness $T2$, and \mathbf{q}_{A6r} is the angular offset.

Paramters of distance R_{A6r} and $\sin \mathbf{q}_{A6r}$ are

$$R_{A6r} = \sqrt{r_{A6r}^2 + z_{A6r}^2}, \quad \sin \mathbf{q}_{A6r} = \frac{r_{A6r}}{R_{A6r}}, \quad (3-50)$$

and here

$$r_{A6r} = (T1 + b) - n1 \times t1, \quad t1 = \frac{T1}{m1}, \quad z_{A6r} = z - n2 \times t2, \quad t2 = \frac{T2}{m2}, \quad (3-51)$$

$$h_{A6r} = (w - r) + (m - 1)(T1 + G) + d. \quad (3-52)$$

Field formulae for computing the magnetic flux density induced from each area in the wire circuit have been derived separately. Consequently, the total magnetic flux density at the point P in the z direction can be easily obtained from summing the contribution of each area and given by

$$B_{ztotal} = B_{zA1} + B_{zA2} + B_{zA3t} + B_{zA3b} + B_{zA4t} + B_{zA4b} + B_{zA5} + B_{zA6l} + B_{zA6r}. \quad (3-53)$$

A fine magnetic pole pitch of $300\mu\text{m}$ was designed by using a wire width $T1$ of $125\mu\text{m}$ and a gap G of $175\mu\text{m}$. The straight wires of L and d are designed with the

values of 6mm and 19.4mm, respectively. The wire thickness T_2 is $40\mu\text{m}$ and 1-A current is applied to the nine-pole magnetic component to induce the magnetic field. The top view of central pole and corresponding cross section of the wire circuit is illustrated in Fig. 3-9.

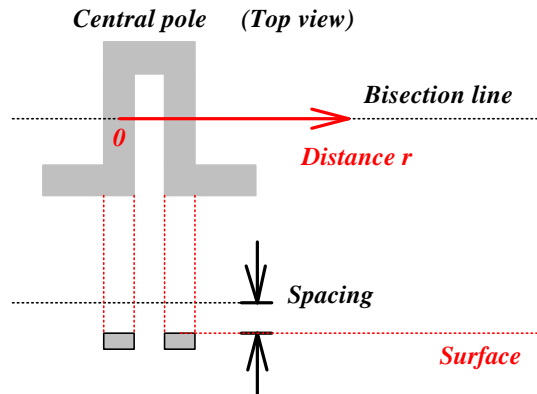


Fig. 3-9. Top view of the central pole on the PCB sample and the corresponding cross section of the wire circuit.

The calculated field distributions of the central pole along the bisection line ($a=b=L/2$) in the z direction are plotted in Fig. 3-10. Various red and blue lines represent the calculated values at the detection spacing of $200\mu\text{m}$ and $300\mu\text{m}$ above the surface of the wire circuit, respectively. The magnetic flux density in the z direction decreases significantly with an increase of the detection spacing. Additionally, these field distributions also indicate that the dimension of magnetic pole pitch is $300\mu\text{m}$.

Another fine magnetic pole pitch of $400\mu\text{m}$ was designed by using a wire width T_1 of $175\mu\text{m}$ and a gap G of $225\mu\text{m}$. The calculated field distributions of the central pole along the bisection line in the z direction are plotted in Fig. 3-11. The similar results are found, as discussed in Fig. 3-10, indicating the fine magnetic pole pitch is $400\mu\text{m}$. As for the measurement data, various experiments will be performed in the next chapter.

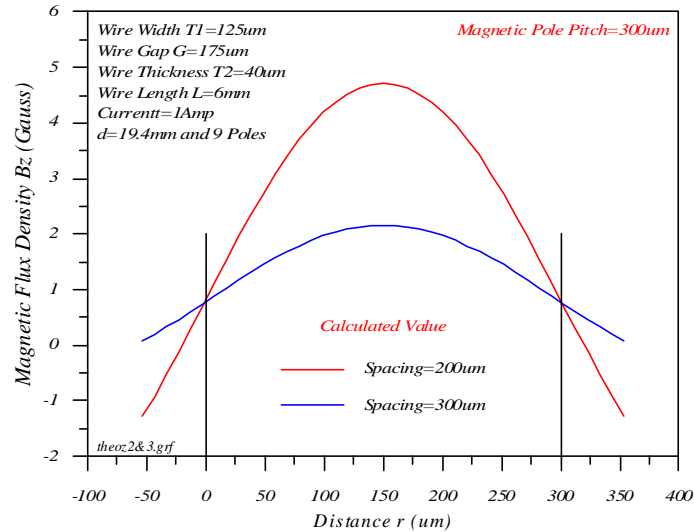


Fig. 3-10. Calculated field distributions of the central pole along the bisection line for the magnetic pole pitch of $300\mu\text{m}$ at the detection spacing of $200\mu\text{m}$ and $300\mu\text{m}$.

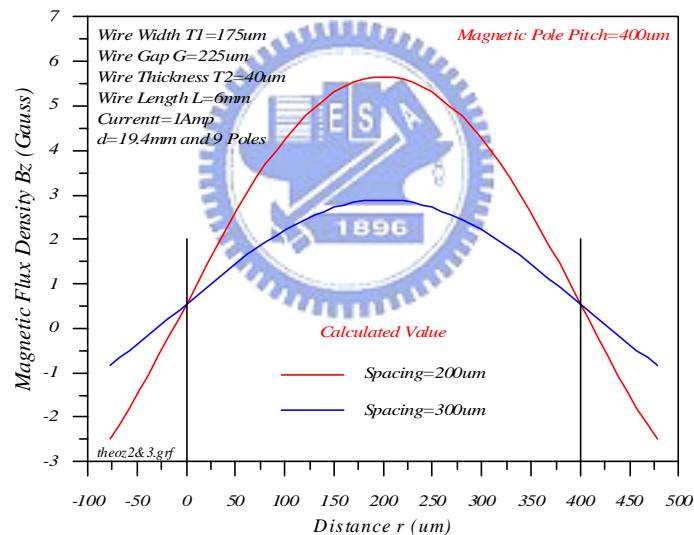


Fig. 3-11. Calculated field distributions of the central pole along the bisection line for the magnetic pole pitch of $400\mu\text{m}$ at the detection spacing of $200\mu\text{m}$ and $300\mu\text{m}$.

3.6 Summary

Field formulae have been derived for computing the magnetic flux density in the fine magnetic pole pitch fabricated on the PCB. These field solutions are expressed in terms of finite sums of elementary functions to enable a parametric study of the

field distribution relative to the wire width T_1 , wire thickness T_2 , gap G , etc. Moreover, these derived field formulae are easily implemented in any programming environment to require only a few minutes of running time on a personal computer.



Chapter 4

Field measurements

A precise magnetic field measuring system was designed and set up to determine the field distribution in the fine magnetic pole pitch fabricated on the PCB. Various wire widths $T1$ and gaps G were used to fabricate different magnetic pole pitches of $300\mu\text{m}$, $350\mu\text{m}$ and $400\mu\text{m}$ on nine-pole magnetic components. The field formulae derived in Chapter 3 were also employed to calculate the field distribution in the fine magnetic pole pitch. As a comparison, the calculated values of magnetic flux density agree with the measurement data. The magnetic flux density in the z direction decreases significantly with an increase of the detection spacing. Additionally, the explicit boundaries between magnetic poles are found, indicating the fine magnetic pole pitches are $300\mu\text{m}$, $350\mu\text{m}$ and $400\mu\text{m}$. Consequently, the resolution of magnetic encoders can be markedly improved by a factor of 3.33 ($1\text{mm}/300\mu\text{m}$) if the fine magnetic pole pitch of $300\mu\text{m}$ is applied.

4.1 Dimensional measurements

Before the field measurements, the dimension of wire circuit fabricated on the PCB should be checked carefully. Since the etching rate is not easy to handle in the etching process as in Fig. 2-10 (f), the dimension of wire width $T1$ and gap G are difficult to control as well. The wire width $T1$ is decreased as the gap G is increased. Conversely, the wire width $T1$ is increased as the gap G is decreased. Correspondingly, the sum of wire width $T1$ and gap G will keep at the same value of

$T1+G$. Although the slight change in the dimension of wire circuit will not affect the field measurements extremely, the checking process is also required to improve the accuracy of measurement data to conform to the calculated values in the field distribution.

A precise dimension measuring system including an X-Y table, a monitor, a CCD (charge-coupled device) module, a screen, and a computer was used to check the dimension of wire circuit, as shown in Fig. 4-1 [38]. A PCB sample is put on the top of X-Y table and the image can be captured through CCD module. The clear image of wire circuit is displayed on the monitor after focusing on the PCB sample by turning Z-knob. After magnifying the image, each copper wire on the PCB sample can be distinguished and measured easily. A relative original point should be designated for calculating the dimension of copper wires.

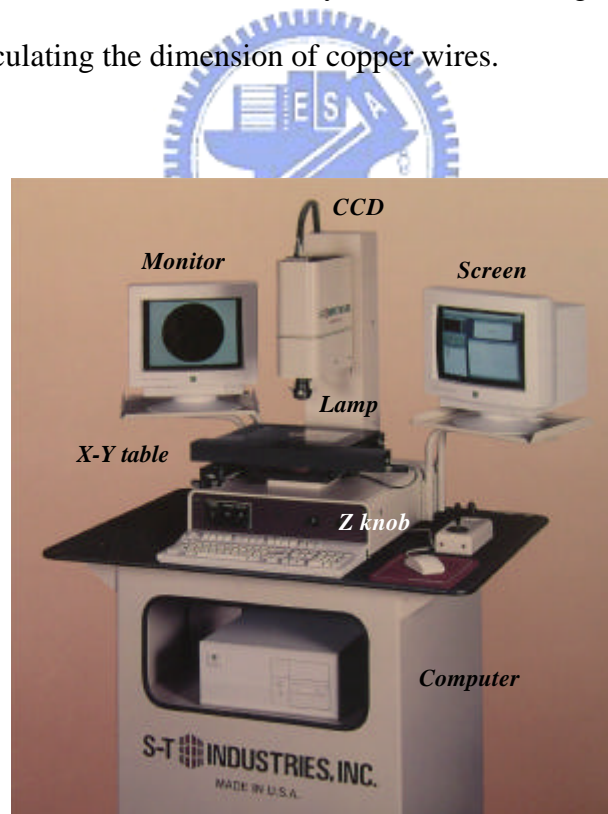


Fig. 4-1. Precise dimension measuring system.

Cursors of *Line V* and *Line H* on the monitor will flash once the cross point *P* meets the edges of copper wires, as shown in Fig. 4-2. The flash point is then

selected and therefore all edges of copper wires on the PCB sample can be obtained by moving cursors. All movements are finely controlled through X-Y table. At the same time, different position coordinates of selected flash points are displayed on the screen. All relative distances between different selected flash points can be easily figured out using corresponding position coordinates. Consequently, all dimensions of each wire segment on the PCB sample can be obtained by using this precise dimension measuring system.

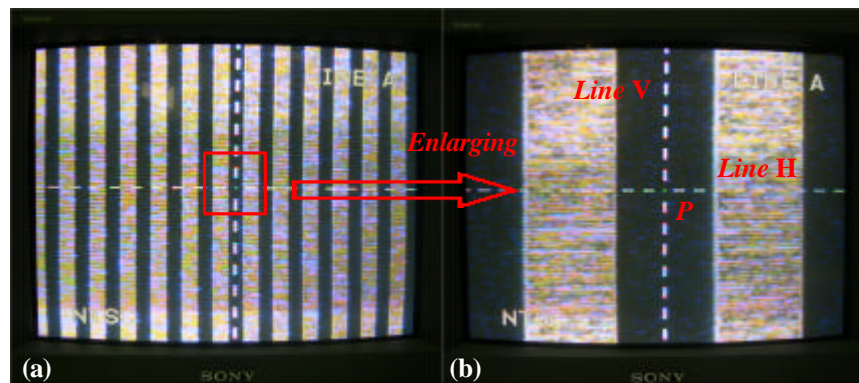


Fig. 4-2. (a) Image of wire circuit captured and displayed on the monitor through CCD module. (b) Enlarged image of copper wires on the PCB sample.

Except checking the dimension of wire segment, the thickness of copper wires also needs to be determined for the field calculation. A part of copper wires including the substrate is cut in order to measure the thickness of copper wires. Then, the part is fixed by using the acrylic resin and its cross section is polished. Both of *Side A* and *Side B* are polished again carefully to be flat, as shown in Fig. 4-3. Planes on both sides should be controlled in parallel as possible for reducing measurement errors. Finally, the thickness of copper wires is obtained through a microscope. After having all dimensions of the wire circuit, the field distribution in the fine magnetic pole pitch on the PCB sample can be easily calculated by using the field formulae derived in Chapter 3.

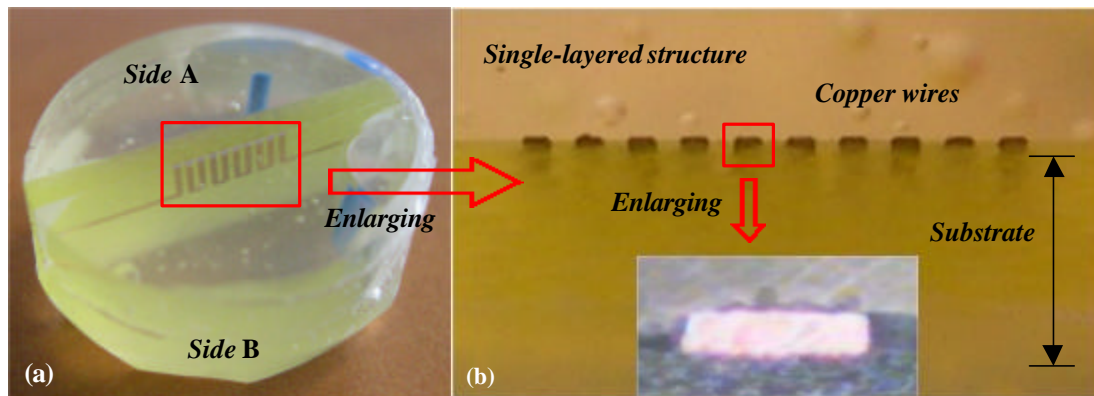


Fig. 4-3. (a) Sample of part copper wires fixed by using the acrylic resin. (b) Enlarged images of the thickness of part copper wires fabricated on the PCB sample.

4.2 Magnetic field measuring system

In order to determine the field distribution in the fine magnetic pole pitch fabricated on the PCB, a precise magnetic field measuring system was designed and set up. This measuring system mainly composes of a precise Hall-effect probe, a probe holder, a PCB sample holder, an X-Y micro-stage and an X-Y-Z micro-stage, as shown in Fig. 4-4. All components are mounted on an optical table to prevent vibrations. The current input and output are connected to a power supply, which can provide a current to induce the magnetic field among the wire circuit on the PCB sample. The precise Hall-effect probe is linked with a high-resolution Gauss meter (ADS HGM 8200) for measuring the small magnetic flux density in the fine magnetic pole pitch [39]. The voltage outputs on the Gauss meter are connected to a precise digital multimeter (GW GDM-391) for detecting the induced voltage [40].

Consequently, the magnitude of magnetic flux density in the fine magnetic pole pitch can be read out easily. The sensing area of Hall element inside the precise Hall-effect probe is only $165 \times 165 \mu\text{m}^2$. Correspondingly, it is capable of measuring the field distribution in the fine magnetic pole pitch of less than 1mm. The

measurement data at any point is the average value over the sensing area of Hall element while in measurements. Before measurements, the relative positions among the PCB sample, micro-stages and Hall-effect probe should be carefully adjusted and aligned to reduce measurement errors.

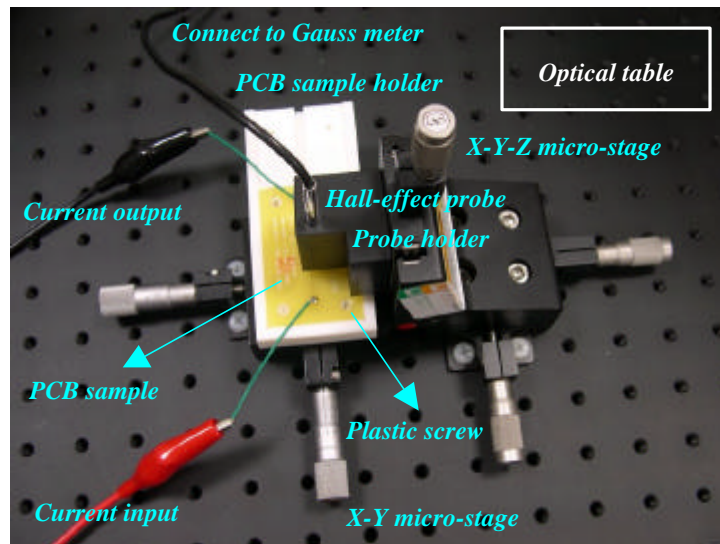


Fig. 4-4. Precise magnetic field measuring system.

The probe and PCB sample holders are made of plastic materials to prevent from affecting the field measurements. Both of them are fixed by using plastic screws and the PCB sample is mounted on the sample holder through the same way. The detection spacing between the surface of PCB sample and Hall-effect probe is finely adjusted using X-Y-Z micro-stage. The corresponding positions of each copper wire on the PCB sample are controlled carefully by means of X-Y and X-Y-Z micro-stages. Consequently, the magnetic flux density at any point above the PCB sample can be obtained through controlling X-Y and X-Y-Z micro-stages. Different positions will induce various output voltages that are detected from the precise digital multimeter. Accordingly, the field distribution in the fine magnetic pole pitch fabricated on the PCB sample can be determined after linking these various output voltages.

4.3 Measurement results

Various wire widths $T1$ and gaps G were used to fabricate different magnetic pole pitch of $300\mu\text{m}$, $350\mu\text{m}$ and $400\mu\text{m}$ on nine-pole magnetic components. All parameters in this study are listed on Table 4-1. The straight wires of L and d are designed with the values of 6mm and 19.4mm , respectively. The wire thickness $T2$ is $40\mu\text{m}$ and 1-A current is applied to the wire circuit to induce the magnetic field. The top view and corresponding cross section of the three central poles on nine-pole magnetic components are illustrated in Fig. 4-5.

Table 4-1 Various wire widths $T1$, gaps G , pitch sizes, and ratios of $T1/G$

Wire width $T1$ (μm)	Gap G (μm)	Pitch size $T1 + G$ (μm)	Ratio of $T1/G$
125	175	300	$5/7=0.714$
150	200	350	$6/8=0.750$
175	225	400	$7/9=0.778$

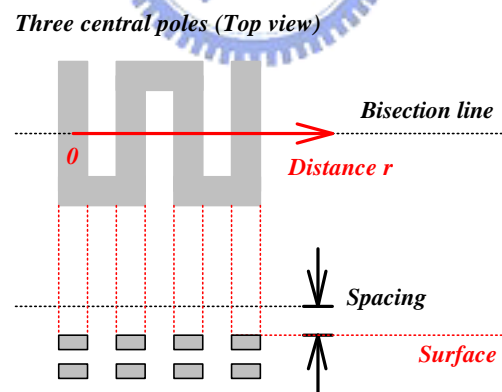


Fig. 4-5. Top view of the three central poles on nine-pole magnetic components and the corresponding cross section.

The field distributions of the three central poles along the bisection line in the z direction are plotted in Fig. 4-6. Various circle and square marks denote the measurement data at the detection spacing of $200\mu\text{m}$ and $300\mu\text{m}$ above the surface of

the wire circuit. The magnetic flux density in the z direction decreases significantly with an increase of the detection spacing. Additionally, the explicit boundaries between magnetic poles are found, indicating the fine magnetic pole pitch is $300\mu\text{m}$. Consequently, the resolution of magnetic encoders can be markedly improved by a factor of 3.33 ($1\text{mm}/300\mu\text{m}$) if the fine magnetic pole pitch of $300\mu\text{m}$ is applied.

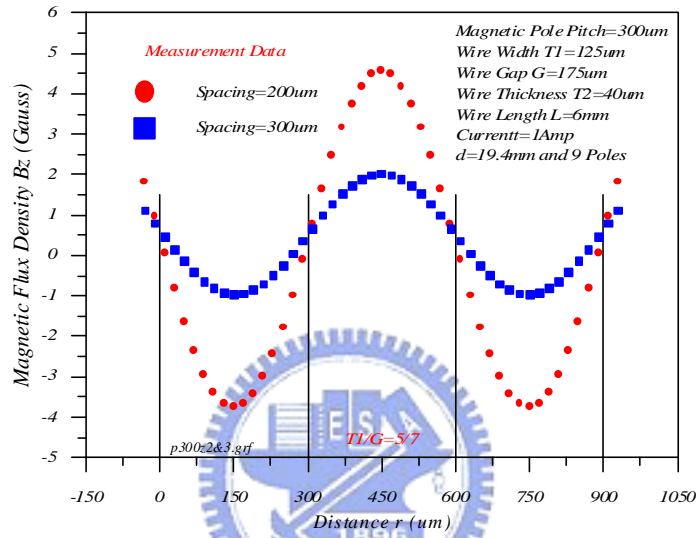


Fig. 4-6. Field distributions at the detection spacing of $200\mu\text{m}$ and $300\mu\text{m}$ for the magnetic pole pitch of $300\mu\text{m}$ ($T1/G=5/7$).

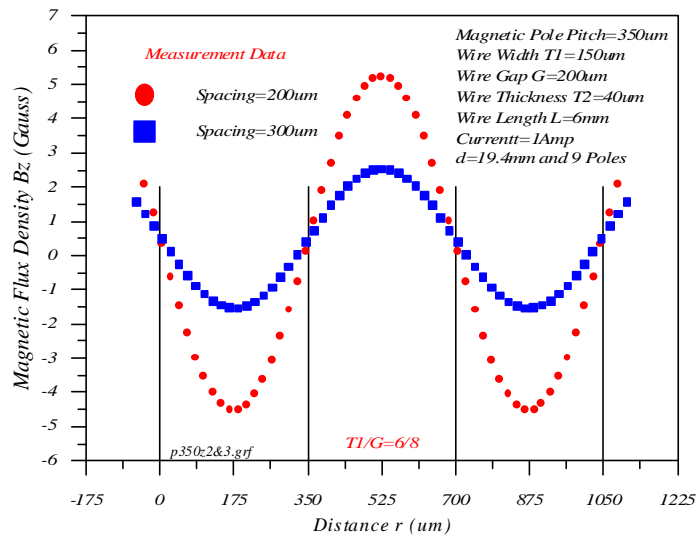


Fig. 4-7. Field distributions at the detection spacing of $200\mu\text{m}$ and $300\mu\text{m}$ for the magnetic pole pitch of $350\mu\text{m}$ ($T1/G=6/8$).

Regarding the pitch sizes of $350\mu\text{m}$ and $400\mu\text{m}$, the similar results are obtained as in Fig. 4-6, and their field distributions are plotted in Figs. 4-7 and 4-8, respectively. From observing the measurement data, the results demonstrate that the designed precise magnetic field measuring system is capable of measuring the field distribution in the fine magnetic pole pitch fabricated on the PCB.

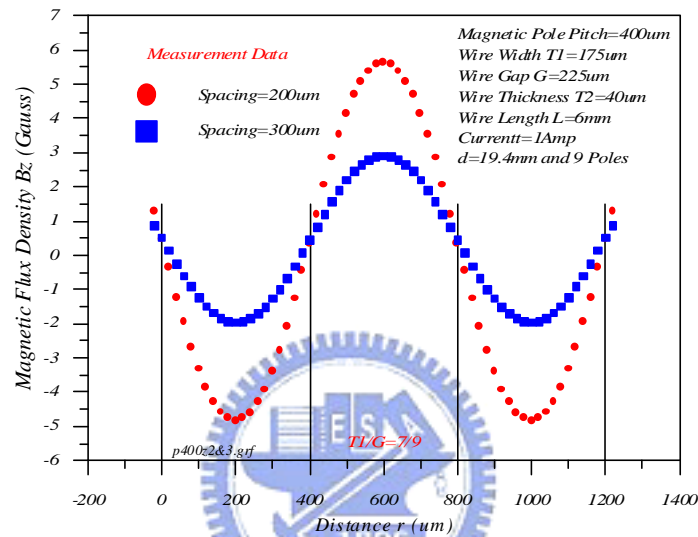


Fig. 4-8. Field distributions at the detection spacing of $200\mu\text{m}$ and $300\mu\text{m}$ for the magnetic pole pitch of $400\mu\text{m}$ ($T1/G=7/9$).

The field distributions of the two central poles along the bisection line with various ratios of $T1/G$ at the detection spacing of $200\mu\text{m}$ are combined and plotted in Fig. 4-9. Various circle, square and cross marks denote the measurement data at different magnetic pole pitches of $300\mu\text{m}$, $350\mu\text{m}$ and $400\mu\text{m}$, respectively. The field distributions are asymmetric to the zero-level in the z direction and the accompanied fine offset is caused by the wire circuit loop design in Fig. 2-4, which has an asymmetric structure for each pole. The similar results are found at the detection spacing of $300\mu\text{m}$, as shown in Fig. 4-10.

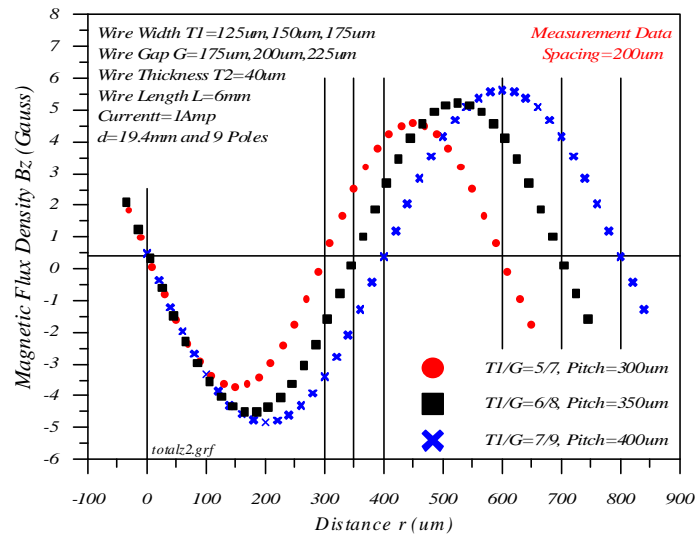


Fig. 4-9. Field distributions with various ratios of $T1/G$ at the detection spacing of $200\mu\text{m}$.

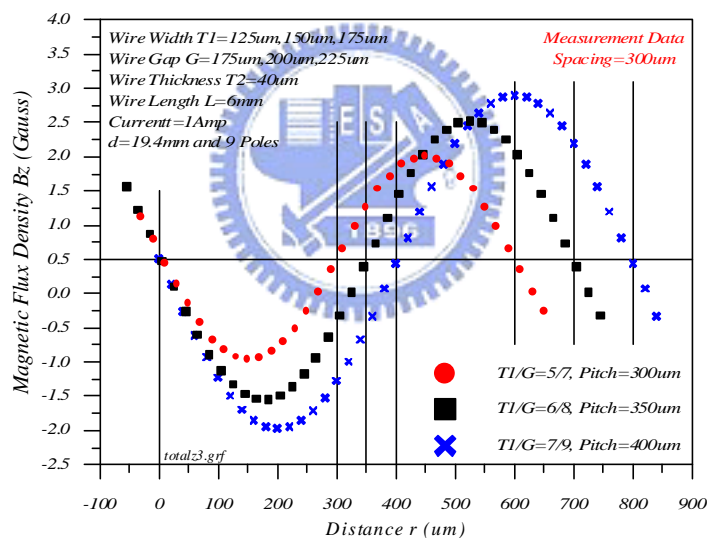


Fig. 4-10. Field distributions with various ratios of $T1/G$ at the detection spacing of $300\mu\text{m}$.

The field distributions of the central pole along the bisection line with various ratios of $T1/G$ at the detection spacing of $200\mu\text{m}$ are combined and plotted in Fig. 4-11. The solid lines represent the calculated values obtained from using the derived field formulae. Various circle, square and cross marks denote the measurement data at different magnetic pole pitches of $300\mu\text{m}$, $350\mu\text{m}$ and $400\mu\text{m}$, respectively. The

magnetic flux density in the z direction increases with an increasing ratio of $T1/G$. That means the magnetic pole pitch of $400\mu\text{m}$ has larger field strength than others. The larger strength in the field distribution is useful to the signal detection. As a comparison, the calculated values of magnetic flux density agree with the measurement data. Consequently, the derived field formulae for computing the field distribution in the fine magnetic pole pitch are confirmed through these various measurements.

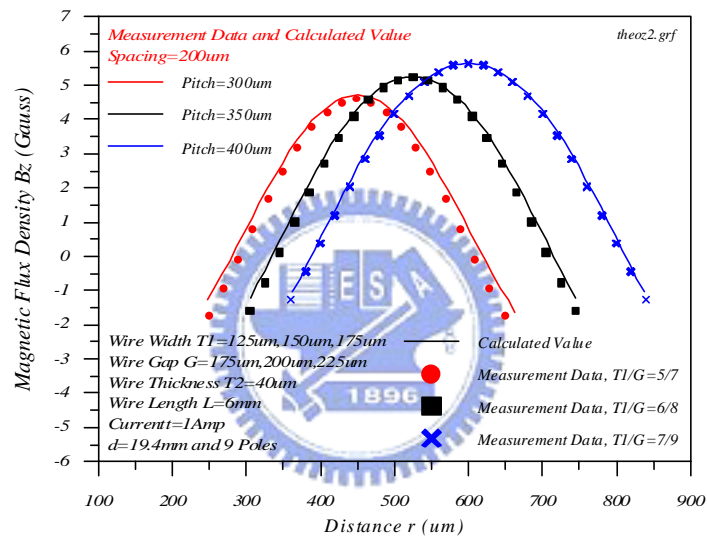


Fig. 4-11. Field distributions of the central pole along the bisection line with various ratios of $T1/G$ at the detection spacing of $200\mu\text{m}$.

Additionally, these measurement results also demonstrate that the designed precise magnetic field measuring system is capable of determining the field distribution induced from the wire circuit fabricated on the PCB. Another field distributions of the central pole along the bisection line with various ratios of $T1/G$ at the detection spacing of $300\mu\text{m}$ are combined and plotted in Fig. 4-12. The similar results are found as in Fig. 4-11.

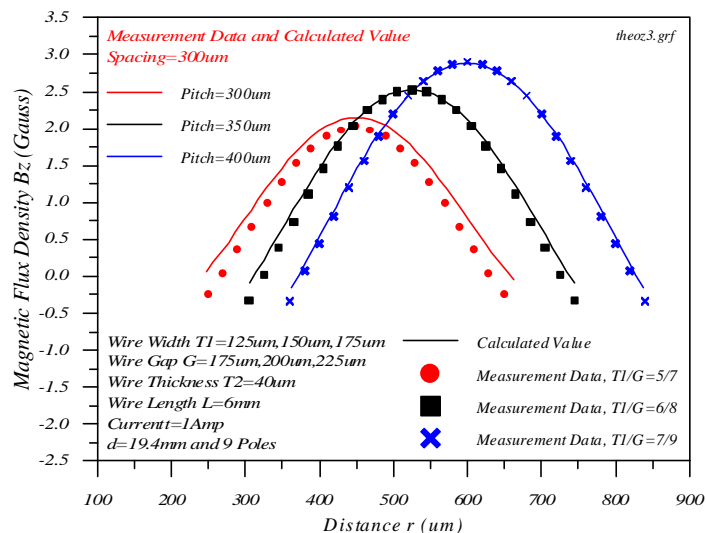


Fig. 4-12. Field distributions of the central pole along the bisection line with various ratios of $T1/G$ at the detection spacing of $300\mu\text{m}$.

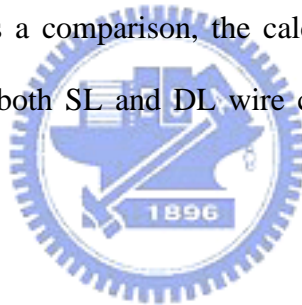
4.4 Summary

Different magnetic pole pitches of $300\mu\text{m}$, $350\mu\text{m}$ and $400\mu\text{m}$ were designed and fabricated on nine-pole magnetic components by using various wire widths $T1$ and gaps G . The field distributions in the z direction have been measured and calculated by the designed magnetic field measuring system and field formulae derived in Chapter 3. As a comparison, the calculated values of magnetic flux density agree with the measurement data. That means both of them are capable of determining the field distribution induced from the wire circuit fabricated on the PCB. The field distributions are asymmetric to the zero-level and the accompanied fine offset is caused by the wire circuit loop design, which has an asymmetric structure for each pole. The magnetic flux density in the z direction increases with an increasing ratio of $T1/G$. Additionally, the explicit boundaries between magnetic poles are found, indicating the fine magnetic pole pitches are $300\mu\text{m}$, $350\mu\text{m}$ and $400\mu\text{m}$. Consequently, the resolution of magnetic encoders can be markedly improved by a factor of 3.3 ($1\text{mm}/300\mu\text{m}$) if the fine magnetic pole pitch of $300\mu\text{m}$ is applied.

Chapter 5

Field enhancement and optimization

Both of single-layered (SL) and dual layered (DL) wire circuit structures were used to investigate the field enhancement in the fine magnetic pole pitch. After measurements, a gain factor of 1.37 was obtained through using DL wire circuit structure. Additionally, the field optimization was also studied to find the optimal magnetic pole pitch, which has larger strength and steeper variation in the field distribution. The larger strength and steeper variation are useful to the signal detection and processing. As a comparison, the calculated values of magnetic flux density in the z direction on both SL and DL wire circuit structures agree with the measurement data.



5.1 Field enhancement

5.1.1 Design and experiments

Various experimental measurements with SL wire circuit structure on the PCB samples have been discussed in Chapter 4. However, the field strength induced from the wire circuit is too small to be useful to the signal detection. In this study, the same wire circuit pattern designed in Fig. 2-4 was fabricated with DL wire circuit structure to improve the field strength for measurements. Figure 5-1 illustrates the cross section, induced magnetic field and equivalent circuit of DL wire circuit structure. An insulating layer t is inserted between two layers to prevent a short

circuit. Two layers are connected in parallel at the terminals of *Point A* and *Point B*. After applying a current to DL wire circuit, both of *Layer 1* and *Layer 2* will induce the magnetic field simultaneously. The total magnetic field is the sum of *Layer 1* and *Layer 2*. Consequently, the field strength can be effectively improved by using DL wire circuit structure.

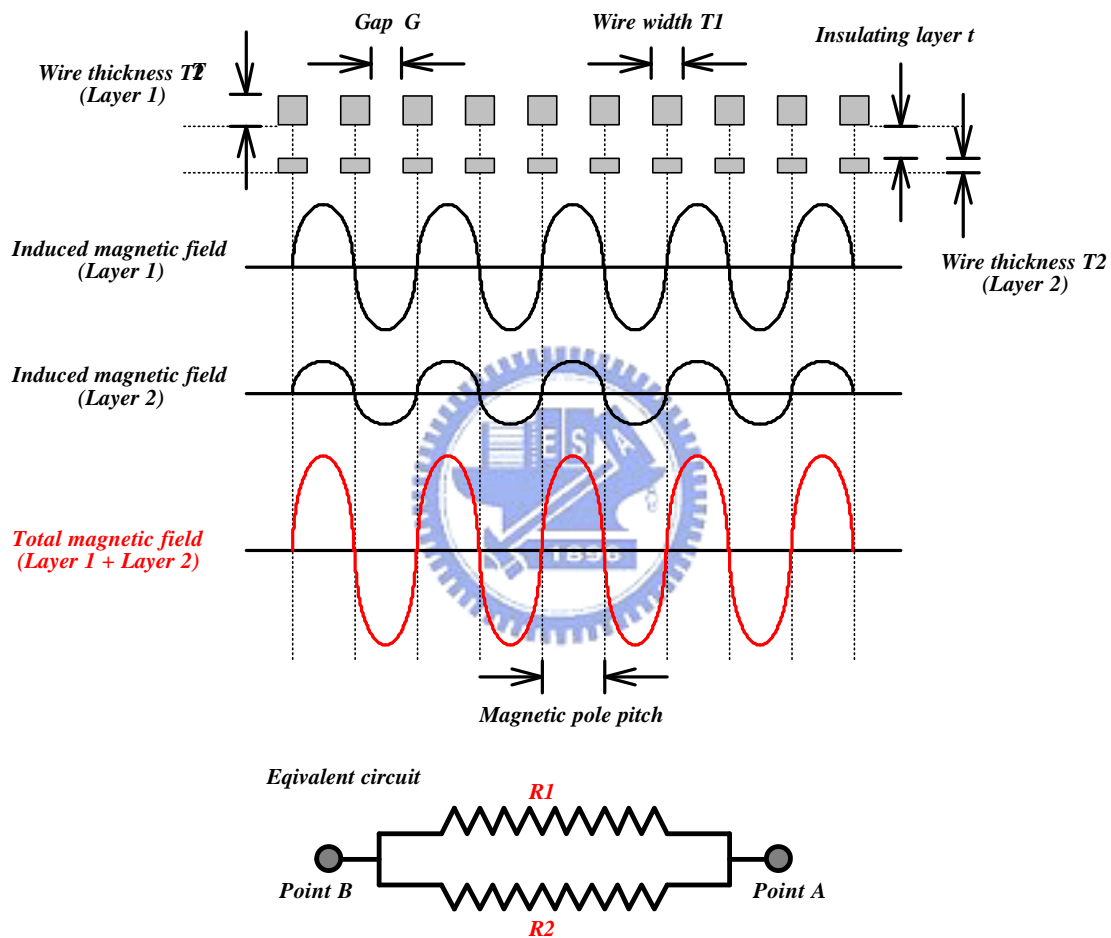


Fig. 5-1. Cross section, induced magnetic field and equivalent circuit of DL wire circuit structure.

A fine magnetic pole pitch of $500\mu\text{m}$ was designed and fabricated with DL wire circuit structure by using a wire width $T1$ of $215\mu\text{m}$ and a gap G of $285\mu\text{m}$. The straight wires of L and d are designed with the values of 6mm and 19.5mm ,

respectively. The wire thickness $T2$ on *Layer 1* is $41\mu\text{m}$ and $33\mu\text{m}$ on *Layer 2*. The insulating layer t is $70\mu\text{m}$ between two layers. The corresponding resistance $R1$ is $173\text{m}\Omega$ and $R2$ is $254\text{ m}\Omega$, which were measured through a precise digital multimeter (Advantest R6450) [41]. According to *Kirchhoff's* and *Ohm's laws*, 1.68-A current should be applied to DL wire circuit to keep 1-A current flowing through *Layer 1* and only 0.68-A current flowing through *Layer 2*. Additionally, the same conditions only on *Layer 1* was also used to fabricate with SL wire circuit structure to compare how it differs from DL wire circuit structure in the field distribution. All parameters on DL wire circuit structure are listed on Table 5-1.

Table 5-1 Parameters on DL wire circuit structure

DL wire circuit structure Parameters	on <i>Layer 1</i>	on <i>Layer 2</i>
Wire width $T1$ (μm)	215	215
Gap G (μm)	285	285
Magnetic pole pitch = $G + T1$ (μm)	500	500
Wire thickness $T2$ (μm)	41	33
Corresponding resistance ($\text{m}\Omega$)	173	254
Pole number	9	9
Insulating layer t (μm)	70	

5.1.2 Results and discussions

The top view and corresponding cross section of the three central poles on nine-pole magnetic components are illustrated as in Fig. 4-5. The field distributions of the three central poles along the bisection line in the z direction on both SL and DL wire circuit structures are plotted in Figs. 5-2 and 5-3. Various circle and square marks denote the measurement data at the detection spacing of $200\mu\text{m}$ and $300\mu\text{m}$ above the surface of the wire circuit. The similar results are found, as discussed in Figs. 4-6, 4-7 and 4-8.

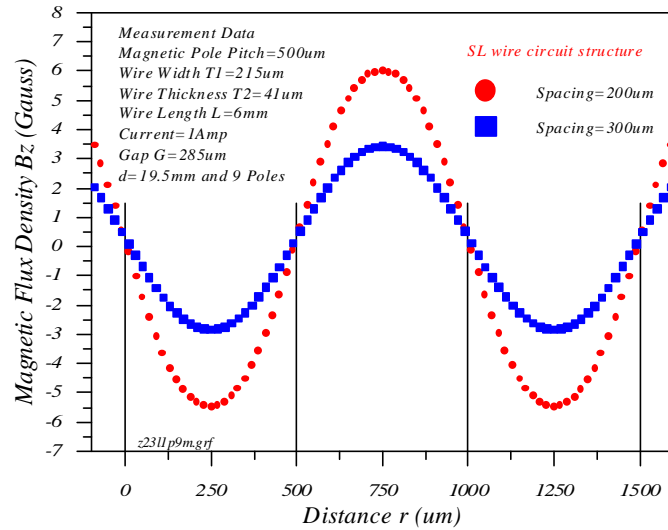


Fig. 5-2. Field distributions for the magnetic pole pitch of 500µm at the detection spacing of 200µm and 300µm with SL wire circuit structure.

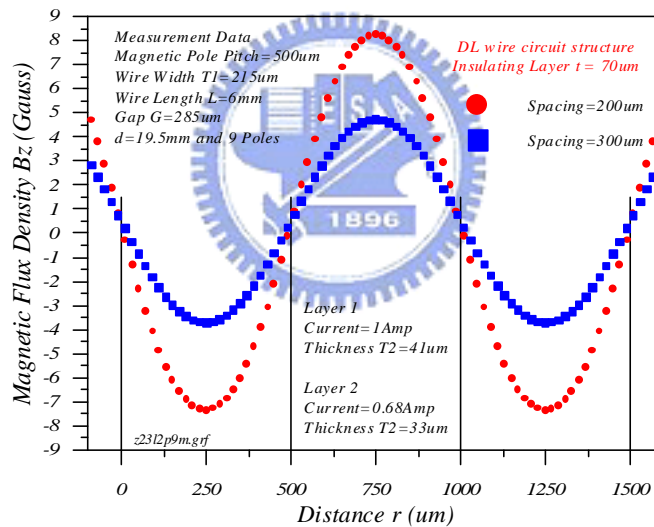


Fig. 5-3. Field distributions for the magnetic pole pitch of 500µm at the detection spacing of 200µm and 300µm with DL wire circuit structure.

Both field distributions in Figs. 5-2 and 5-3 are combined and re-plotted in Fig. 5-4 to compare the difference between SL and DL wire circuit structures. The plus and triangular marks denote the measurement data for SL wire circuit structure. As for the circle and square marks, they represent the measurement results at DL wire circuit structure. The maximum magnetic flux density in the z direction for SL wire

circuit structure at the detection spacing of $200\mu\text{m}$ and $300\mu\text{m}$ are 6.02 Gauss and 3.44 Gauss , respectively. Those for DL wire circuit structure are 8.24 Gauss and 4.72 Gauss , respectively. As a comparison, the maximum magnetic flux density in the z direction can be effectively enhanced by a factor of 1.37 through using DL wire circuit structure. The larger field strength in the field distribution is useful to the signal detection.

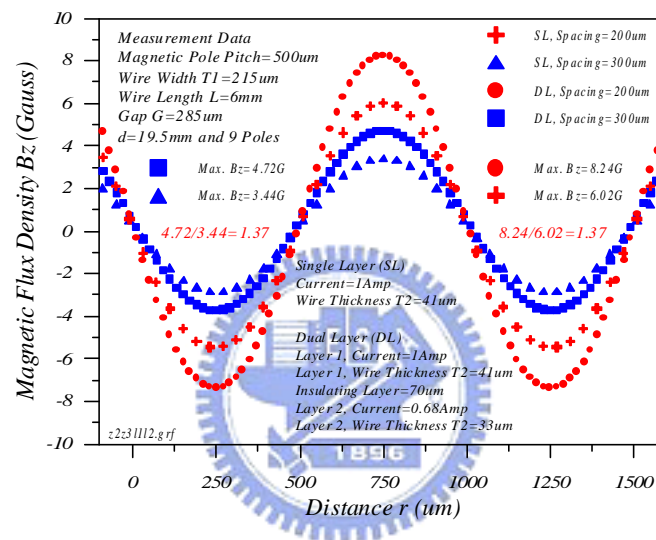


Fig. 5-4. Field distributions for the magnetic pole pitch of $500\mu\text{m}$ at SL and DL wire circuit structures.

Regarding the calculated field distributions of the central pole along the bisection line for SL and DL wire circuit structures, they are plotted in Figs. 5-5 and 5-6, respectively. The solid lines represent the calculated values obtained from using the field formulae derived in Chapter 3. Various circle and square marks denote the measurement data at the detection spacing of $200\mu\text{m}$ and $300\mu\text{m}$. As a comparison, the calculated values of magnetic flux density in the z direction agree with the measurement data. Consequently, the derived field formulae for calculating the field distribution are confirmed again through these various measurements.

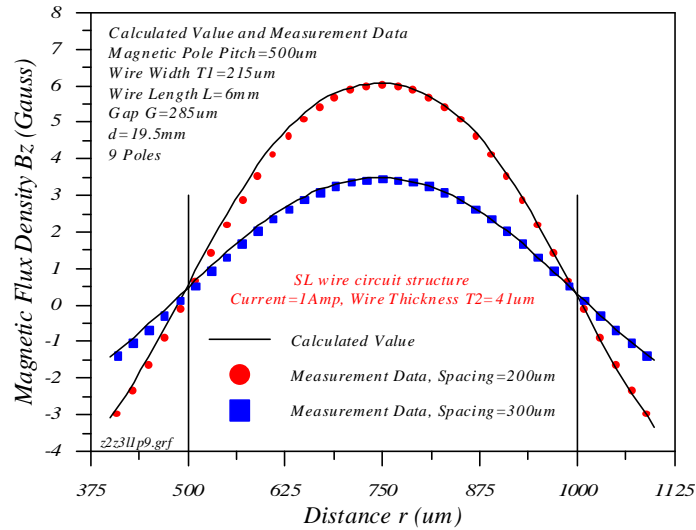


Fig. 5-5. Calculated values and measurement data of the central pole for the magnetic pole pitch of $500\mu\text{m}$ on SL wire circuit structure.

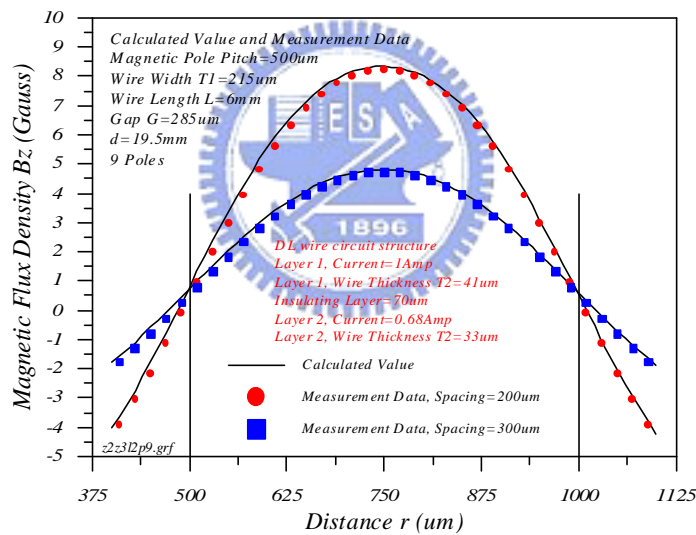


Fig. 5-6. Calculated values and measurement data of the central pole for the magnetic pole pitch of $500\mu\text{m}$ on DL wire circuit structure.

5.1.3 Summary

A fine magnetic pole pitch of $500\mu\text{m}$ was accomplished on both SL and DL wire circuit structures. The field strength can be enhanced by a factor of 1.37 through using DL wire circuit structure. The larger field strength in the field distribution is

useful to the signal detection. Additionally, the calculated values of magnetic flux density in the z direction on both SL and DL wire circuit structures agree with the measurement data. Consequently, the derived field formulae are confirmed again through various measurements.

5.2 Field optimization

5.2.1 Design and experiments

Field formulae for computing the field distribution in the fine magnetic pole pitch have been derived in Chapter 3. These field solutions enable a parametric study of the field distribution relative to the wire width $T1$, gap G , etc. Consequently, these field formulae can be used to investigate the field optimization in the fine magnetic pole pitch. Figure 5-7 demonstrates the field distribution of a straight wire with a finite length, which was calculated along the bisection line at the detection spacing of $200\mu\text{m}$ by Eq. (3-15). The magnetic flux density in the z direction varies with the distance r significantly. The maximum magnetic flux density is found at the distance of r_{max} . Since the straight wires on both left and right sides in the pole structure are symmetric, the field distributions can be calculated and plotted as in Figs. 5-8 (a) and (b). The optimal condition in the field distribution is obtained after these two field distributions are combined at the distance of r_{max} as in Fig. 5-8 (d).

Consequently, the gap G between these two straight wires should be designed with the value of $2 \times (r_{max} - T1)$. Accordingly, the corresponding optimal magnetic pole pitch is $T1 + G = 2r_{max} - T1$. The optimal magnetic pole pitch in the field distribution has larger strength than in Fig. 5-8 (c) and steeper variation than in Fig. 5-

8 (e) when the gap G is not equal to the value of $2 \times (r_{max} - T1)$.

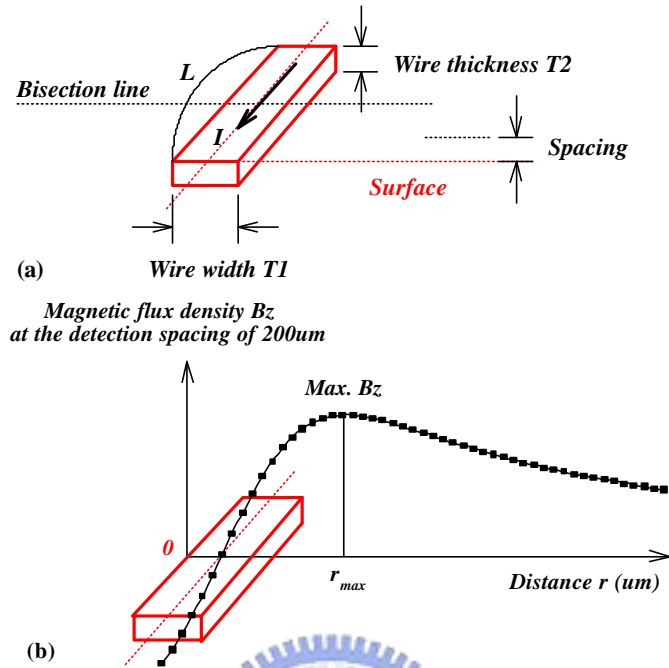


Fig. 5-7. (a) Geometrical structure of a straight wire with a finite length. (b) The field distribution calculated along the bisection line at the detection spacing of $200\mu\text{m}$.

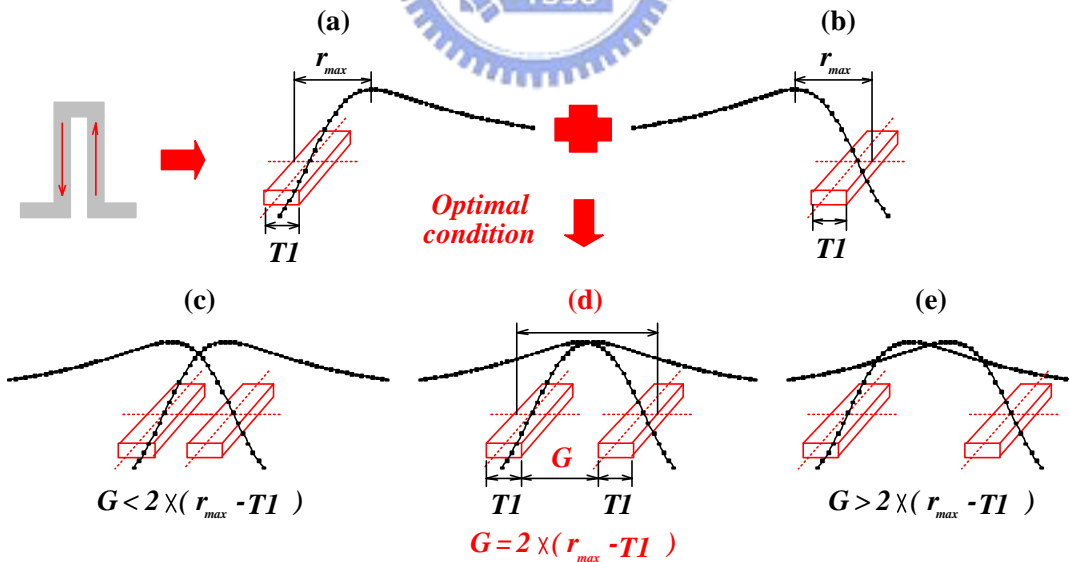


Fig. 5-8. Pole structure and optimal condition in the field distribution.

In this study, the wire thickness $T2$ is $41\mu\text{m}$, wire length L is 6mm , and 1-A current is applied to the straight wire to induce the magnetic field. Various wire widths $T1$ of $190\mu\text{m}$ and $235\mu\text{m}$ were used to investigate the field optimization.

After calculation, the optimal magnetic pole pitches are $465\mu\text{m}$ and $495\mu\text{m}$, respectively. All parameters of wire width $T1$, distance r_{max} , gap G and optimal magnetic pole pitch $T1+G$ are listed on Table 5-2.

Table 5-2 Parameters of wire width $T1$, distance r_{max} , gap G and optimal magnetic pole pitch $T1+G$

Wire width (μm) $T1$	Distance (μm) r_{max}	Gap G (μm) $2 \times (r_{max} - T1)$	Optimal magnetic pole pitch (μm) $T1+G=2r_{max}-T1$
190.0	327.5	275	465.0
235.0	365.0	260	495.0

5.2.2 Results and discussions

Various gaps G of $175\mu\text{m}$, $275\mu\text{m}$ and $375\mu\text{m}$ with the same wire width $T1$ of $190\mu\text{m}$ were used to fabricate different magnetic pole pitches of $365\mu\text{m}$, $465\mu\text{m}$ and $565\mu\text{m}$ on nine-pole magnetic components. The top view of central pole and corresponding cross section of the wire circuit is illustrated as in Fig. 3-9. After measurements, the field distributions of the central pole along the bisection line at the detection spacing of $200\mu\text{m}$ above the surface of the wire circuit are plotted in Fig. 5-9. The circle, square and cross marks denote the measurement data at the magnetic pole pitch of $365\mu\text{m}$, $465\mu\text{m}$ and $565\mu\text{m}$, respectively.

As a comparison, the optimal magnetic pole pitch of $465\mu\text{m}$ has larger strength than the pitch size of $365\mu\text{m}$ and steeper variation than that of $565\mu\text{m}$ between *Line A* and *Line B*. Both of larger strength and steeper variation in the field distribution are useful to the signal detection and processing. The solid lines represent the calculated values of magnetic flux density in the z direction obtained from using the field formulae derived in Chapter 3. The results agree with the measurement data.

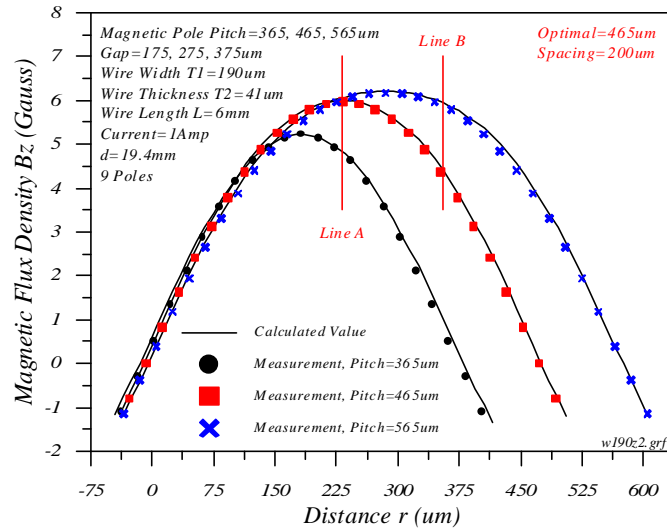


Fig. 5-9. Field distributions of the central pole at different magnetic pole pitches of $365\mu\text{m}$, $465\mu\text{m}$ and $565\mu\text{m}$ by using the wire width $T1$ of $190\mu\text{m}$.

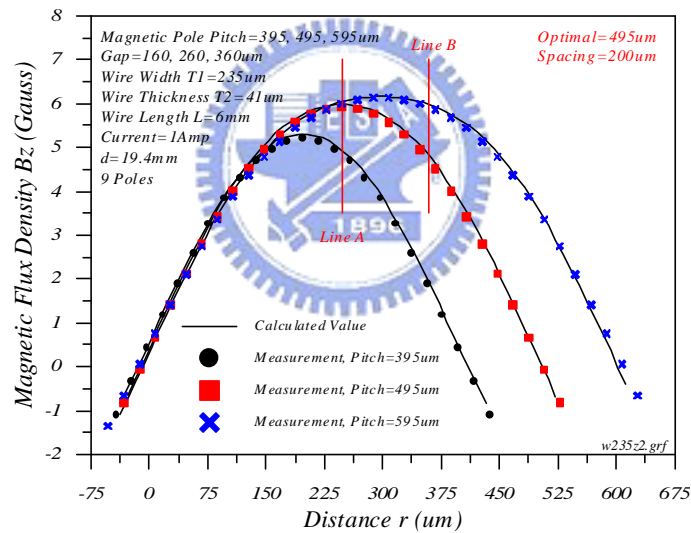


Fig. 5-10. Field distributions of the central pole at different magnetic pole pitches of $395\mu\text{m}$, $495\mu\text{m}$ and $595\mu\text{m}$ by using the wire width $T1$ of $235\mu\text{m}$.

Another wire width $T1$ of $235\mu\text{m}$ with various gaps G of $160\mu\text{m}$, $260\mu\text{m}$ and $360\mu\text{m}$ was also used to fabricate different magnetic pole pitches of $395\mu\text{m}$, $495\mu\text{m}$ and $595\mu\text{m}$ to investigate the field optimization again. The field distributions of the central pole along the bisection line in the z direction at the detection spacing of $200\mu\text{m}$ are plotted in Fig. 5-10. The solid lines represent the calculated values.

Various circle, square and cross marks denote the measurement data at the magnetic pole pitch of $395\mu\text{m}$, $495\mu\text{m}$ and $595\mu\text{m}$, respectively. The smooth field variation is also found at the magnetic pole pitch of $595\mu\text{m}$ between *Line A* and *Line B*, as the pitch size of $565\mu\text{m}$ discussed in Fig. 5-9. Consequently, the optimal magnetic pole pitch of $495\mu\text{m}$ has larger strength and steeper variation in the field distribution than others.

5.2.3 Summary

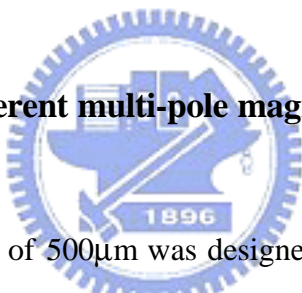
The field optimization in the fine magnetic pole pitch of less than 1mm fabricated on the PCB has been investigated and demonstrated. Different optimal magnetic pole pitches of $465\mu\text{m}$ and $495\mu\text{m}$ were obtained by using wire widths $T1$ of $190\mu\text{m}$ and $235\mu\text{m}$, respectively. Such an optimal design has larger strength and steeper variation in the field distribution, which are useful to the signal detection and processing. Additionally, the calculated values of magnetic flux density in the z direction agree with the measurement data. Consequently, the field formulae derived in Chapter 3 can be used to investigate the field optimization in the fine magnetic pole pitch fabricated on the PCB.

Chapter 6

Field variation analysis

Field measurements, enhancement and optimization in the fine magnetic pole pitch fabricated on the PCB have been discussed in Chapters 4 and 5. However, the field distributions in the z direction were only determined along the bisection line on a nine-pole magnetic component. Consequently, different multi-pole magnetic components were designed to analyze the field variation. Additionally, the field distributions along different measuring routes were also investigated in this chapter.

6.1 Variation among different multi-pole magnetic components



A fine magnetic pole pitch of $500\mu\text{m}$ was designed and fabricated on different 9-pole, 19-pole and 29-pole magnetic components by using a wire width $T1$ of $240\mu\text{m}$ and a gap G of $260\mu\text{m}$. The straight wires of L and d are designed with the values of 6mm and 19.5mm, respectively. The wire thickness $T2$ is $41\mu\text{m}$ and 1-A current is applied to the multi-pole magnetic components to induce the magnetic field. The top view and corresponding cross section of the three central poles on nine-pole magnetic components are illustrated as in Fig. 4-5. After measurements, the field distributions of the three central poles along the bisection line at the detection spacing of $200\mu\text{m}$ and $300\mu\text{m}$ are plotted in Fig. 6-1. Various plus, square, and circle marks denote the measurement data at the 9-pole, 19-pole and 29-pole magnetic component, respectively. The magnetic flux density in the z direction decreases significantly with an increase of the detection spacing. The explicit boundaries between magnetic

poles are found, indicating the fine magnetic pole pitch is $500\mu\text{m}$. The field strength and variation among different multi-pole magnetic components are very close and tend towards a value when the pole number is increased.

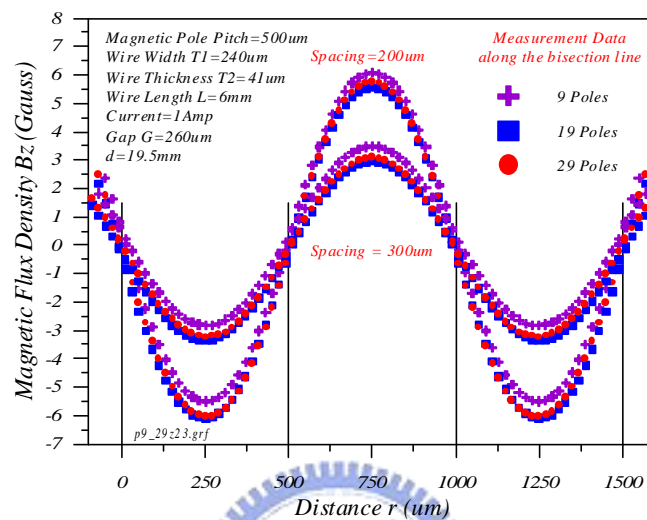


Fig. 6-1. Field distributions along the bisection line among different 9-pole, 19-pole, and 29-pole magnetic components with a fine magnetic pole pitch of $500\mu\text{m}$.

6.2 Variation along different measuring routes

Another fine magnetic pole pitch of $400\mu\text{m}$ was designed and fabricated on 9-pole and 19-pole magnetic components by using a wire width T_1 of $180\mu\text{m}$ and a gap G of $220\mu\text{m}$. As mentioned in Fig. 2-4, various wire segments of a and b are related by $L=a+b$. In this study, the field measurements are along not only the bisection line but also different measuring routes, as illustrated in Fig. 6-2.

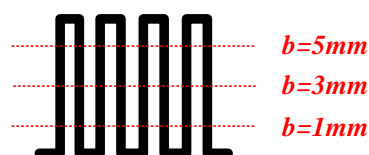


Fig. 6-2. Different measuring routes with various wire segments b .

Additionally, a small current of 0.5-A is applied to 9-pole and 19-pole magnetic components to induce the magnetic field. The field distributions of the three central poles in the 9-pole magnetic component along different measuring routes at the detection spacing of $200\mu\text{m}$ are plotted in Fig. 6-3. The similar results are found, as discussed in Fig. 6-1.

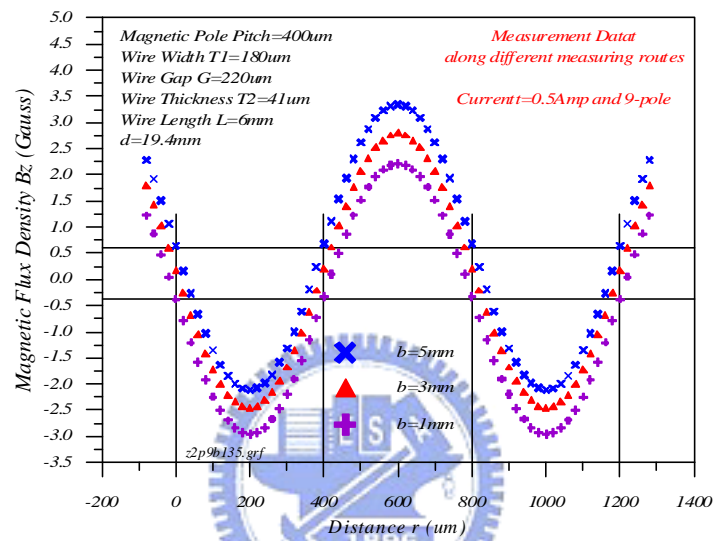


Fig. 6-3. Field distributions along different measuring routes in the 9-pole magnetic component with a fine magnetic pole pitch of $400\mu\text{m}$.

The maximum and minimum magnetic flux density in the z direction increase significantly with an increase of the wire segment b . This increase is caused by the contributions of *Area 3*, *Area 4* and *Area 5*, as described in the section 3.6. Both of positive and negative field strength are enhanced when the measuring route is close to *Area 3*, *Area 4* and *Area 5*. The peak-to-peak values of magnetic flux density only vary slightly along different measuring routes. The explicit boundaries between magnetic poles are also found, indicating the fine magnetic pole pitch is $400\mu\text{m}$ even the measuring route is far from the bisection line. These characteristics are useful to the subsequent signal detection and processing.

The similar results in the 19-pole magnetic component are observed in Fig. 6-4. The maximum, minimum and peak-to-peak values of magnetic flux density at various wire segments b for 9-pole and 19-pole magnetic components are listed on Table 6-1.

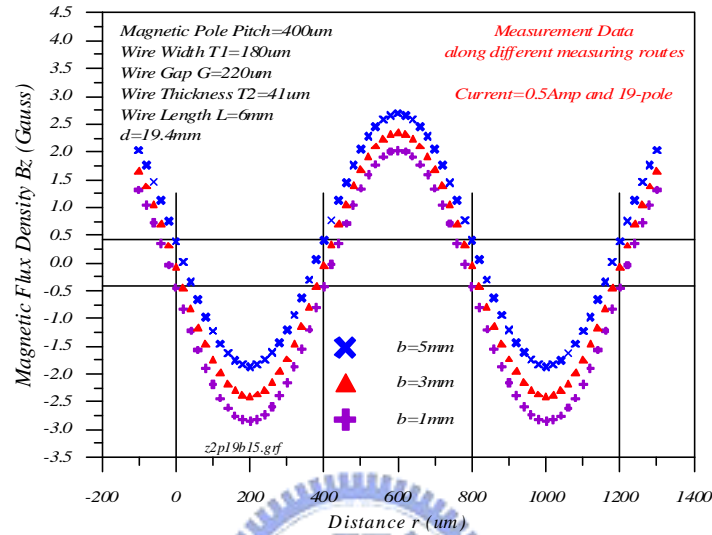


Fig. 6-4. Field distributions along different measuring routes in the 19-pole magnetic component with a fine magnetic pole pitch of $400\mu\text{m}$.

Table 6-1 Various values of magnetic flux density at various wire segments b for 9-pole and 19-pole magnetic components

For 9-pole magnetic component			
Wire segment b (mm)	Maximum value (G)	Minimum value (G)	P-P value (G)
1	2.22	-2.96	5.18
3	2.80	-2.45	5.25
5	3.35	-2.12	5.47
For 19-pole magnetic component			
Wire segment b (mm)	Maximum value (G)	Minimum value (G)	P-P value (G)
1	2.03	-2.84	4.87
3	2.35	-2.39	4.74
5	2.69	-1.87	4.56

As for the field calculations of the central pole, they are plotted in Figs. 6-5 and 6-6. The solid lines represent the calculated values obtained from using the derived field formulae. Various plus, triangle and cross marks denote the measurement data

along different measuring routes with the wire segment b of 1mm, 3mm and 5mm. As a comparison, the calculated values of magnetic flux density in the z direction agree with the measurement data on both 9-pole and 19-pole magnetic components.

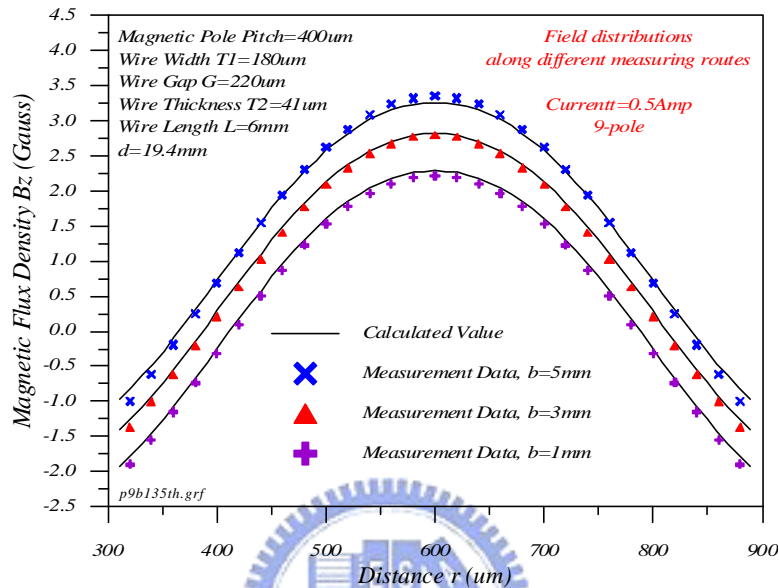


Fig. 6-5. Field distributions of the central pole along different measuring routes in the z direction for the 9-pole magnetic component.

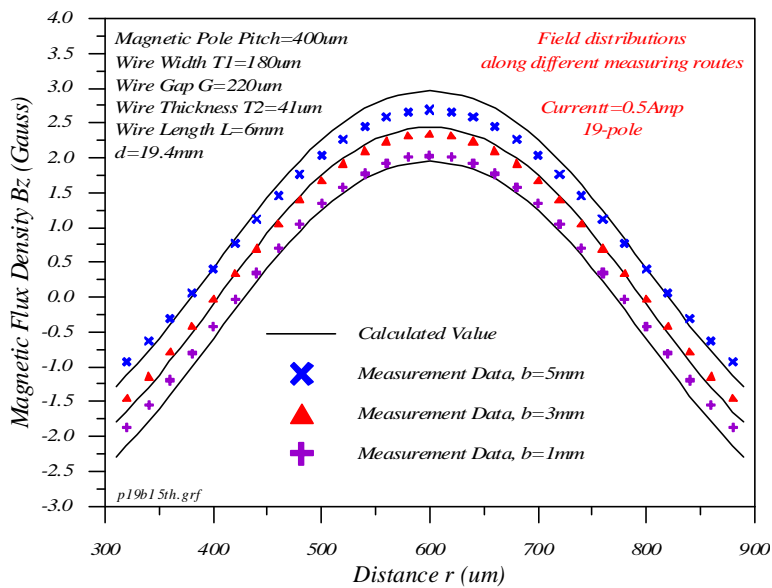


Fig. 6-6. Field distributions of the central pole along different measuring routes in the z direction for the 19-pole magnetic component.

6.3 Summary

A fine magnetic pole pitch of $500\mu\text{m}$ was designed and fabricated on different 9-pole, 19-pole, and 29-pole magnetic components by using a wire width $T1$ of $240\mu\text{m}$ and a gap G of $260\mu\text{m}$. The field strength and variation along the bisection line among different multi-pole magnetic components are very close and tend towards a value when the pole number is increased.

Another fine magnetic pole pitch of $400\mu\text{m}$ was designed and fabricated on 9-pole and 19-pole magnetic components by using a wire width $T1$ of $180\mu\text{m}$ and a gap G of $220\mu\text{m}$. The field distributions were determined along not only the bisection line but also different measuring routes. Additionally, a small current of 0.5-A is applied to the multi-pole magnetic components to induce the magnetic field. The maximum and minimum magnetic flux density in the z direction increases with an increase of the wire segment b . The peak-to-peak values of magnetic flux density only vary slightly along different measuring routes. These characteristics are useful to the subsequent signal detection and processing. As for the field calculations, the magnetic flux density in the z direction agree with the measurement data on both 9-pole and 19-pole magnetic components.

Chapter 7

Conclusions

In this dissertation, the innovative method by using the printed circuit board (PCB) manufacturing technology has been demonstrated to effectively fabricate a multi-pole magnetic component with a fine magnetic pole pitch of less than 1mm. This innovative method provides a simple process without using the complicated technologies such as machining technique, magnetizing head and magnetization machine. Additionally, it is also a cost-effective method to enable mass production easily. Different pole numbers and pitch sizes can be also easily fabricated on the PCB through this flexible approach.

The field formulae have been also derived to compute the field distribution in the multi-pole magnetic component. These field solutions are expressed in terms of finite sums of elementary functions to enable a parametric study of the field distribution relative to the wire width $T1$, gap G , etc. Moreover, these field formulae are also easily implemented in any programming environment to require only a few minutes of running time on a personal computer.

As for the field measurements, a precise magnetic field measuring system was designed and set up to determine the field distribution in the multi-pole magnetic component. It comprises a precise Hall-effect probe, a probe holder, a PCB sample holder, an X-Y micro-stage and an X-Y-Z micro-stage. All components are mounted on an optical table to prevent vibrations. The sensing area of Hall element inside the precise Hall-effect probe is only $165 \times 165 \mu\text{m}^2$. Correspondingly, it is capable of measuring the field distribution in the fine magnetic pole pitch of less than 1mm.

Different magnetic pole pitches of $300\mu\text{m}$, $350\mu\text{m}$ and $400\mu\text{m}$ were accomplished on various 9-pole magnetic components. The magnetic flux density in the z direction along the bisection line decreases significantly with an increase of the detection spacing. The field distributions are asymmetric to the zero-level and the explicit boundaries between magnetic poles are found, indicating the magnetic pole pitch is $300\mu\text{m}$, $350\mu\text{m}$ and $400\mu\text{m}$, respectively. Correspondingly, the resolution of magnetic encoders can be markedly improved by a factor of 3.33 ($1\text{mm}/300\mu\text{m}$).

Additionally, a dual-layered wire circuit structure was used to improve the field strength in the fine magnetic pole pitch and a gain factor of 1.37 was obtained in the field enhancement. Furthermore, the field optimization was also investigated to find the optimal magnetic pole pitch. Such an optimal design has larger strength and steeper variation in the field distribution. Both of them are useful to the subsequent signal detection and processing.

Except the field enhancement and optimization, the field variation was also studied in this dissertation. Different 9-pole, 19-pole, and 29-pole magnetic components were fabricated with the same magnetic pole pitch. The field strength and variation among different multi-pole magnetic components are very close and tend towards a value when the pole number is increased. Additionally, the field distribution in the fine magnetic pole pitch was determined along not only the bisection line but also different measuring routes with various wire segments b . The maximum and minimum magnetic flux density in the z direction increase with an increasing wire segment b . The peak-to-peak values of magnetic flux density only vary slightly along different measuring routes. These characteristics are also useful to the subsequent signal detection and processing.

All experimental measurements were performed by the designed magnetic field measuring system. Regarding the field calculations, they were computed through

using the field formulae derived in Chapter 3. As a comparison, the calculated values of magnetic flux density in the z direction agree with the measurement data. Consequently, the derived field formulae for computing the field distribution in the fine magnetic pole pitch are confirmed.

A summary of main results has been presented in the above-mentioned conclusions. Some areas for future works are described as the following:

A. Thermal issue

The primary concern in this dissertation is the thermal issue. A large current of 1-A is applied to the wire circuit in order to induce a large magnetic field for measurements. The power consumption is thus very serious and needs to be reduced as possible. The most effective means of decreasing the power consumption is to reduce the applied current. However, the magnetic field induced from the wire circuit will be also markedly decreased. The small magnetic field can be easily detected through using MR sensors. Consequently, MR sensors will be used instead of Hall-effect probe to determine the field distribution in the multi-pole magnetic component fabricated on the PCB.

B. Annular multi-pole magnetic component

The rotary magnetic encoders are also widely used to detect the position, angle or speed in precise control systems. However, an annular multi-pole magnetic field distribution is required, as discussed in Fig. 2-3. The possible wire circuit pattern is also proposed in this figure. After applying a current to the wire circuit, an annular multi-pole magnetic field distribution is obtained. Consequently, the related

research about the annular multi-pole magnetic component will be studied in the future.

C. Field enhancement

A dual-layered wire circuit structure has been used to improve the field strength in the fine magnetic pole pitch. After measurements, a gain factor of 1.37 was obtained in the field enhancement. Unfortunately, the fabrication of dual-layered wire circuit structure is not easy to handle to make two layers in positions precisely. Another solution by coating a magnetic film on the substrate is considered. This film is with very high permeability that can concentrate the magnetic flux to enhance the magnetic field. Correspondingly, the field enhancement through coating a magnetic film on the substrate will be investigated in the future as well.



D. Resolution improvement

The wire circuit fabricated on the silicon substrate with a nano scale has been realized in the semiconductor industry. Consequently, the wire width and gap on the wire circuit can be easily reduced to obtain a tiny magnetic pole pitch by using the semiconductor manufacturing technology. Accordingly, the resolution of magnetic encoders can be further improved in applications through this method. However, the magnetic field induced from the wire circuit will be very small and difficult to detect. Correspondingly, a high sensitive GMR sensor should be used to determine the field distribution in the tiny magnetic pole pitch. The related research in fabricating the tiny magnetic pole pitch by using the semiconductor manufacturing technology will be also studied in the future.

References

- [1] K. Mohri, K. Yoshino, H. Okuda, R. Malmhall, “Highly accurate rotation-angle sensors using amorphous star-shaped cores”, IEEE Trans. Magn. Vol. 22, (1986) 409-411.
- [2] K. Miyashita, T. Takahashi, M. Yamanaka, “Features of a magnetic rotary encoder”, IEEE Trans. Magn., Vol. 23, (1987) 2182-2184.
- [3] H. Okuno, M. Ishikawa, Y. Sakaki, “Properties of SmCo film for magnetic rotary encoder”, IEEE Trans. Magn., Vol. 23, (1987) 2425-2427.
- [4] P. Campbell, “Magnetic rotary position encoders with magneto-resistive sensors”, Proceedings of Fourth International Conference on Electrical Machines and Drives, Sep. 13-15, (1989) 359-363.
- [5] T. Mikoshiba, K. Yamasawa, “A new non-repeated code type magnetic scale using a simple absolute head”, IEEE Trans. Magn. Vol. 32, (1996) 4938-4940.
- [6] Y. Kikuchi, F. Nakamura, H. Wakiwaka, H. Yamada, Y. Yamamoto, “Consideration for a high resolution of magnetic rotary encoder”, IEEE Trans. Magn. Vol. 32, (1996) 4959-4961.
- [7] Y. Kikuchi, F. Nakamura, H. Wakiwaka, H. Yamada, J. Yamamoto, “Consideration of magnetization and detection on magnetic rotary encoder using finite element method”, IEEE Trans. Magn. Vol. 33, (1997) 2159-2162.
- [8] Y. Kikuchi, F. Nakamura, H. Wakiwaka, H. Yamada, H. Yamamoto, “Index phase output characteristics of magnetic rotary encoder using a magneto-resistive element”, IEEE Trans. Magn. Vol. 32, (1997) 3370-3372.
- [9] 游志榮, “磁性編碼器磁環充磁機原型設計、製作及測試”, 國立中央大學/機械工程研究所, (84級) 碩士論文.

- [10] 莊俊良, “磁性編碼器之磁環分析與模擬”, 國立中央大學/機械工程研究所, (85級) 碩士論文.
- [11] 賴坤奇, “磁性編碼器原型製作、測試”, 國立中央大學/機械工程研究所, (86級) 碩士論文.
- [12] 林江清等, “磁性編碼器研製技術報告(一)”, 工業技術研究院/工業材料研究所, (1996) 技術報告.
- [13] 林江清等, “磁性編碼器研製技術報告(二)”, 工業技術研究院/工業材料研究所, (1997) 技術報告.
- [14] 羅應照等, “磁氣式回轉速度檢出磁石充磁設計規畫書”, 工業技術研究院/機械工業研究所, (1995) 技術報告.
- [15] 黃世民等, “磁氣式回轉速度檢出磁石充磁驗證規畫書”, 工業技術研究院/機械工業研究所, (1995) 技術報告.
- [16] 羅應照等, “磁氣式回轉速度檢出磁石充磁應用維護說明”, 工業技術研究院/機械工業研究所, (1995) 技術報告.
- [17] 翁明輝, “線性尺千倍頻電路設計”, 國立中央大學/機械工程研究所, (87級) 碩士論文.
- [18] 翁明輝等, “線性磁性定位伺服系統電路設計”, 工業技術研究院/光電工業研究所, (1998) 技術報告.
- [19] 陳建祥等, “直線型分解式位置控制系統電路設計”, 工業技術研究院/光電工業研究所, (1999) 技術報告.
- [20] <http://www.magnix.com/product/magne-sheet.html>, the website of Toyo Jiki Industry Co., LTD.
- [21] <http://www.magnetizer.com.tw/p9.htm>, the website of Ney Hwu Electrical Co., LTD.
- [22] Y. Kikuchi, T. Yoneda, Y. Kataoka, K. Shiotani, H. Wakiwaka, H. Yamada, “Considerations of output voltage waveform on magnetic linear encoder for

- artificial heart using linear pulse motor”, *Sens. Actuator A-Phys.* 81, (2000) 309-312.
- [23] Ashok K. Agarwala, “Method of magnetizing high energy rare earth alloy magnets”, USA Patent Number 4,920,326 (1990).
- [24] Svetlana Reznik, Edward P. Furlani, William E. Schmidtman, “Apparatus for polarizing rare-earth permanent magnets”, USA Patent Number 5,852,393 (1998).
- [25] Y. J. Luo, E. T. Hwang, S. M. Huang, “Multi-pole magnetization of high resolution magnetic encoder”, *Proceedings, EEIC/ICWA Exposition, Chicago, USA, Oct. 4-7, (1993) 237 242.*
- [26] P. Lorrain et al., *Electromagnetic Fields And Waves*, W. H. Freeman Company, New York, 3rd Ed., 1988, p. 330.
- [27] P. Lorrain et al., *Electromagnetic Fields And Waves*, W. H. Freeman Company, New York, 3rd Ed., 1988, p. 353-354.
- [28] <http://www.autodesk.com.tw/adsk/servlet/home?siteID=1170616&id=2501735>, the website of Autodesk Company in Taipei branch.
- [29] <http://www.solidworks.com/>, the website of SolidWorks Corporation.
- [30] <http://www.ptc.com/products/proe/wildfire/>, the website of Parametric Technology Corporation.
- [31] <http://www.orcad.com/>, the website of Cadence Design Systems Company.
- [32] <http://www.altium.com/protel/>, the website of Altium Limited.
- [33] <http://www.mentor.com/pcb/>, the website of Mentor Graphics Corporation.
- [34] <http://www.big5.tomshardware.com/howto/01q3/010814/index.html>, the website of tom’s hardware guide.
- [35] P. Lorrain et al., *Electromagnetic Fields And Waves*, W. H. Freeman Company, New York, 3rd Ed., 1988, pp. 327-328.

- [36] P. Lorrain et al., *Electromagnetic Fields And Waves*, W. H. Freeman Company, New York, 3rd Ed., 1988, p. 330.
- [37] Hsi-Huan Chen, *Electromagnetism—Principles and Examples--*, Central Book Company, Taiwan, 4th Ed., 1987, p. 868. (Publishing in Chinese)
- [38] <http://www.stindustries.com/index.html>, the website of S-T Industries, Inc.
- [39] http://www.magnix.com/product/gauss_ads.htm, the website of Toyojiki Industry Co., LTD.
- [40] http://www.goodwill.com.tw/Products/GDM-391A_T.htm, the website of GOOD WILL INSTRUMENT CO., LTD.
- [41] http://webbuilder.asiannet.com/325/style/content/CN-01a/product.asp?lang=1&customer_id=325&name_id=3454&rid=13885, the website of BURGEON INSTRUMENT CO., LTD.



Appendix

The following programs of *Loop.m*, *Encoder.m* and *Loadfile.m* were designed to calculate the field distribution induced from the wire circuit according to the field formulae derived in Chapter 3. A fine magnetic pole pitch of $300\mu\text{m}$ was used to demonstrate the calculating process. This pitch size is fabricated on a nine-pole magnetic component by using a wire with $T1$ of $150\mu\text{m}$ and a gap G of $150\mu\text{m}$. The straight wires of L and d are designed with the values of 6mm and 19.4mm , respectively. The wire thickness $T2$ is $40\mu\text{m}$ and 1-A current is applied to the nine-pole magnetic component to induce the magnetic field. The field distribution of the central pole along the bisection line in the z direction is calculated at the detection spacing of $200\mu\text{m}$ above the surface of the wire circuit.

It starts from *Loop.m* with various distances r and *Encoder.m* is then called to compute the magnetic flux density. All calculated values are collected to plot the figure by using *Loadfile.m*. Consequently, the field distribution in the fine magnetic pole pitch can be obtained.

Please note that these programs are required to run in *MATLAB* environment.

Loop.m

```
% Please note the "x" is equal to the "r" in the file of Encoder.m %
clear
x=0/10^6
encoder
save c:\temp\a1.dat Bz_total -ascii
clear
x=25/10^6
```

```
encoder
save c:\temp\a2.dat Bz_total -ascii
clear
x=50/10^6
encoder
save c:\temp\a3.dat Bz_total -ascii
clear
x=75/10^6
encoder
save c:\temp\a4.dat Bz_total -ascii
clear
x=100/10^6
encoder
save c:\temp\a5.dat Bz_total -ascii
clear
x=125/10^6
encoder
save c:\temp\a6.dat Bz_total -ascii
clear
x=150/10^6
encoder
save c:\temp\a7.dat Bz_total -ascii
clear
x=175/10^6
encoder
save c:\temp\a8.dat Bz_total -ascii
clear
x=200/10^6
encoder
save c:\temp\a9.dat Bz_total -ascii
clear
x=225/10^6
encoder
save c:\temp\a10.dat Bz_total -ascii
clear
x=250/10^6
encoder
save c:\temp\a11.dat Bz_total -ascii
```




```
clear
x=275/10^6
encoder
save c:\temp\a12.dat Bz_total -ascii
clear
x=300/10^6
encoder
save c:\temp\a13.dat Bz_total -ascii
clear
x=325/10^6
encoder
save c:\temp\a14.dat Bz_total -ascii
clear
x=350/10^6
encoder
save c:\temp\a15.dat Bz_total -ascii
clear
x=375/10^6
encoder
save c:\temp\a16.dat Bz_total -ascii
clear
x=400/10^6
encoder
save c:\temp\a17.dat Bz_total -ascii
clear
x=425/10^6
encoder
save c:\temp\a18.dat Bz_total -ascii
x=450/10^6
encoder
save c:\temp\a19.dat Bz_total -ascii
Loadfile
```



Encoder.m

```

% Total magnetic flux density on the left side %
m1=301;           % m1 divisions in the wire width T1
m2=81;           % m2 divisions in the wire thickness T2
m=5;             % m wire segments on the left side of the middle line
T1=150/10^6;     % the wire width
T2=40/10^6;     % the wire thickness
G=150/10^6;     % the gap
r=x;            % the distance from the left edge of the central pole
d=19.4/10^3;    % the straight wire for connecting to the current source
I=1;            % the applied current
z1=200/10^6;    % the spacing above the surface of the wire circuit
z=z1+T2;        % the spacing including the wire thickness T2
L=6000/10^6;    % the straight wire related by L=a+b
a=L/2;          % the wire segment along the bisection line
b=a;            % the wire segment along the bisection line
w=2*T1+G;       % the wire segments on the top or bottom sides
u0=4*pi/10^7;   % the permeability in free space
Bz_left=0;      % the initial value of magnetic flux density

for n1=1:m1;
for n2=1:m2;
for n=1:m;

r_left=(r-n1/m1*T1)+(n-1)*(T1+G);
z_left=z-n2/m2*T2;
R_left=sqrt(r_left^2+z_left^2);

B1=u0*(I/m1/m2)/(4*pi*R_left);
B2=a/sqrt(a^2+R_left^2);
B3=b/sqrt(b^2+R_left^2);
B4=r_left/R_left*(-1)^(n-1);
B=B1*(B2+B3)*B4*10^4;
Bz_left=Bz_left+B;

end;

```

```
end;
```

```
end;
```

```
fprintf(' Total magnetic flux density on the left side
= %e (Gauss)\n',Bz_left);
```

Bz_left

```
% Total magnetic flux density on the right side %
```

```
Bz_right=0;
```

```
for n1=1:m1;
```

```
for n2=1:m2;
```

```
for n=1:m;
```

```
r_right=[(w-r)-(n1/m1*T1)]+(n-1)*(T1+G);
```

```
z_right=z-n2/m2*T2;
```

```
R_right=sqrt(r_right^2+z_right^2);
```

```
B1=u0*(I/m1/m2)/(4*pi*R_right);
```

```
B2=a/sqrt(a^2+R_right^2);
```

```
B3=b/sqrt(b^2+R_right^2);
```

```
B4=r_right/R_right*(-1)^(n-1);
```

```
B=B1*(B2+B3)*B4*10^4;
```

```
Bz_right=Bz_right+B;
```

```
end;
```

```
end;
```

```
end;
```

```
fprintf(' Total magnetic flux density on the right side
= %e (Gauss)\n',Bz_right);
```

Bz_right

```
% Total magnetic flux density on the top side Bz_top (only n=1) %
```

```
Bz_top=0;
```

```
for n1=1:m1;
```

```
for n2=1:m2;
```

```

r_top=(T1+a)-n1/m1*T1;
z_top=z-n2/m2*T2;
R_top=sqrt(r_top^2+z_top^2);
B1=u0*(I/m1/m2)/(4*pi*R_top);
B2=(w-r)/sqrt((w-r)^2+R_top^2);
B3=r/sqrt(r^2+R_top^2);
B4=r_top/R_top;
B=B1*(B2+B3)*B4*10^4;
Bz_top=Bz_top+B;

end;
end;

fprintf(' Total magnetic flux density on the top side (only n=1)      Bz_top
= %e (Gauss)\n\n',Bz_top);

% Total magnetic flux density on the left top side Bz_tleft (except n=1) %

Bz_tleft=0;
for n1=1:m1;
for n2=1:m2;
for n=3:2:m;

r_tleft=(T1+a)-n1/m1*T1;
z_tleft=z-n2/m2*T2;
R_tleft=sqrt(r_tleft^2+z_tleft^2);
h_tleft=r+(n-1)*(T1+G);
% the point (r,0,h) and h can be h_tleft, h_bleft, h_tright and h_bright

B1=u0*(I/m1/m2)/(4*pi*R_tleft);
B2=h_tleft/sqrt(h_tleft^2+R_tleft^2);
B3=(h_tleft-w)/sqrt((h_tleft-w)^2+R_tleft^2);
B4=r_tleft/R_tleft;
B=B1*(B2-B3)*B4*10^4;
Bz_tleft=Bz_tleft+B;

```



```

end;
end;
end;

fprintf(' Total magnetic flux density on the left top side          Bz_tleft   =
%e   (Gauss)\n',Bz_tleft);

% Total magnetic flux density on the left bottom side Bz_bleft (except n=1) %

Bz_bleft=0;
for n1=1:m1;
for n2=1:m2;
for n=2:2:m;

r_bleft=(T1+b)-n1/m1*T1;
z_bleft=z-n2/m2*T2;
R_bleft=sqrt(r_bleft^2+z_bleft^2);
h_bleft=r+(n-1)*(T1+G);
% the distance from bottom or bottom side to the main pole

B1=u0*(I/m1/m2)/(4*pi*R_bleft);
B2=h_bleft/sqrt(h_bleft^2+R_bleft^2);
B3=(h_bleft-w)/sqrt((h_bleft-w)^2+R_bleft^2);
B4=r_bleft/R_bleft*(-1);
B=B1*(B2-B3)*B4*10^4;
Bz_bleft=Bz_bleft+B;

end;
end;
end;

fprintf(' Total magnetic flux density on the left bottom side          Bz_bleft   =
%e   (Gauss)\n',Bz_bleft);

Bz_tbleft=Bz_tleft+Bz_bleft;
fprintf(' Total magnetic flux density on the left top and bottom sides  Bz_tbleft   =
%e   (Gauss)\n\n',Bz_tbleft);

```

```

% Total magnetic flux density on the right top side Bz_tright (except n=1) %

Bz_tright=0;
for n1=1:m1;
for n2=1:m2;
for n=3:2:m;

r_tright=(T1+a)-n1/m1*T1;
z_tright=z-n2/m2*T2;
R_tright=sqrt(r_tright^2+z_tright^2);
h_tright=(w-r)+(n-1)*(T1+G);

B1=u0*(I/m1/m2)/(4*pi*R_tright);
B2=h_tright/sqrt(h_tright^2+R_tright^2);
B3=(h_tright-w)/sqrt((h_tright-w)^2+R_tright^2);
B4=r_tright/R_tright;
B=B1*(B2-B3)*B4*10^4;
Bz_tright=Bz_tright+B;

end;
end;
end;

fprintf(' Total magnetic flux density on the right top side      Bz_tright  =
%e    (Gauss)\n',Bz_tright);

```



```

% Total magnetic flux density on the right bottom side Bz_bright (except n=1) %

```

```

Bz_bright=0;
for n1=1:m1;
for n2=1:m2;
for n=2:2:m;

r_bright=(T1+b)-n1/m1*T1;
z_bright=z-n2/m2*T2;
R_bright=sqrt(r_bright^2+z_bright^2);
h_bright=(w-r)+(n-1)*(T1+G);

```

```

B1=u0*(I/m1/m2)/(4*pi*R_bright);
B2=h_bright/sqrt(h_bright^2+R_bright^2);
B3=(h_bright-w)/sqrt((h_bright-w)^2+R_bright^2);
B4=r_bright/R_bright*(-1);
B=B1*(B2-B3)*B4*10^4;
Bz_bright=Bz_bright+B;

end;
end;
end;

fprintf(' Total magnetic flux density on the right bottom side      Bz_bright
= %e (Gauss)\n',Bz_bright);

Bz_tbright=Bz_tright+Bz_bright;
fprintf(' Total magnetic flux density on the right top and bottom sides Bz_tbright =
%e (Gauss)\n',Bz_tbright);

% Total magnetic flux density on the left side for connection Bz_lcon %

Bz_lcon=0;
for n1=1:m1;
for n2=1:m2;

r_lcon=(T1+b)-n1/m1*T1;
z_lcon=z-n2/m2*T2;
R_lcon=sqrt(r_lcon^2+z_lcon^2);
h_lcon=r+(m-1)*(T1+G)+d;

B1=u0*(I/m1/m2)/(4*pi*R_lcon);
B2=h_lcon/sqrt(h_lcon^2+R_lcon^2);
B3=(h_lcon-d)/sqrt((h_lcon-d)^2+R_lcon^2);
B4=r_lcon/R_lcon*(-1);
B=B1*(B2-B3)*B4*10^4;
Bz_lcon=Bz_lcon+B;

```

```

end;
end;

fprintf(' Total magnetic flux density on the left side for connection Bz_lcon =
%e (Gauss)\n',Bz_lcon);

% Total magnetic flux density on the right side for connection Bz_rcon %

Bz_rcon=0;
for n1=1:m1;
for n2=1:m2;

r_rcon=(T1+b)-n1/m1*T1;
z_rcon=z-n2/m2*T2;
R_rcon=sqrt(r_rcon^2+z_rcon^2);
h_rcon=(w-r)+(m-1)*(T1+G)+d;

B1=u0*(I/m1/m2)/(4*pi*R_rcon);
B2=h_rcon/sqrt(h_rcon^2+R_rcon^2);
B3=(h_rcon-d)/sqrt((h_rcon-d)^2+R_rcon^2);
B4=r_rcon/R_rcon*(-1);
B=B1*(B2-B3)*B4*10^4;
Bz_rcon=Bz_rcon+B;

end;
end;

fprintf(' Total magnetic flux density on the right side for connection Bz_rcon =
%e (Gauss)\n\n',Bz_rcon);

Bz_total=Bz_left+Bz_right+Bz_top+Bz_tleft+Bz_bleft+Bz_tright+Bz_bright+Bz_lco
n+Bz_rcon;
fprintf(' Total magnetic flux density of all wire segments Bz_total
= %e (Gauss)\n\n\n',Bz_total);

```


Loadfile.m

```

clear
load c:\temp\a1.dat
load c:\temp\a2.dat
load c:\temp\a3.dat
load c:\temp\a4.dat
load c:\temp\a5.dat
load c:\temp\a6.dat
load c:\temp\a7.dat
load c:\temp\a8.dat
load c:\temp\a9.dat
load c:\temp\a10.dat
load c:\temp\a11.dat
load c:\temp\a12.dat
load c:\temp\a13.dat
load c:\temp\a14.dat
load c:\temp\a15.dat
load c:\temp\a16.dat
load c:\temp\a17.dat
load c:\temp\a18.dat
load c:\temp\a19.dat

a=[a1 a2 a3 a4 a5 a6 a7 a8 a9 a10 a11 a12 a13 a14 a15 a16 a17 a18 a19]
x=0:25:450
r=[x' a']
save c:\temp\a.dat r -ascii

plot(x,a)
grid on
title('The field distribution of the central pole calculated at the detection spacing of
200um')
xlabel('Distance r (um)')
ylabel('Total magnetic flux density in z direction Bz (Gauss)')

```

